LEVEL

IMPROVEMENT OF SPECTER II CODE: INJECTION AND EVOLUTION OF AN ARTIFICIAL RADIATION BELT

J. B. Cladis, et al.

Lockheed Palo Alto Research Laboratory
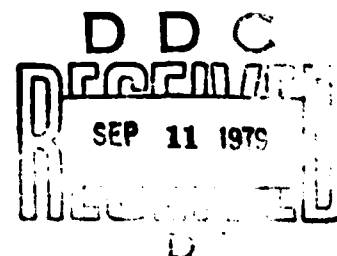Palo Alto, CA 94304

August 1979

Final Report

Prepared for
Director
DEFENSE NUCLEAR AGENCY
Washington, DC 20305

DDC

SEP 11 1979

AIR FORCE WEAPONS LABORATORY
Air Force Systems Command
Kirtland Air Force Base, NM 87117

79 09 4 069

This final report was prepared by Lockheed Palo Alto Research Laboratory, Palo Alto, California, under Contract F29601-76-C-0095, Job Order WDNB4307 with the Air Force Weapons Laboratory, Kirtland Air Force Base, New Mexico. Capt Robert C. Backstrom (DYC) was the Laboratory Project Officer-in-Charge.

When US Government drawings, specifications, or other data are used for any purpose other than a definitely related Government procurement operation, the Government thereby incurs no responsibility nor any obligation whatsoever, and the fact that the Government may have formulated, furnished, or in any way supplied the said drawings, specifications, or other data, is not to be regarded by implication or otherwise, as in any manner licensing the holder or any other person or corporation, or conveying any rights or permission to manufacture, use, or sell any patented invention that may in any way be related thereto.

This report has been authored by a contractor of the United States Government. Accordingly, the United States Government retains a nonexclusive, royalty-free license to publish or reproduce the material contained herein, or allow others to do so, for the United States Government purposes.

This report has been reviewed by the Information Office (OI) and is releasable to the National Technical Information Service (NTIS). At NTIS, it will be available to the general public, including foreign nations.

This technical report has been reviewed and is approved for publication.

ROBERT C. BACKSTROM
Captain, USAF
Project Officer

FOR THE COMMANDER

JOHN D. HAWKINS   THOMAS W. CIAMBRONE
Major, USAF   Colonel, USAF
Chief, Satellite and C³ Branch   Chief, Applied Physics Division

REPORT DOCUMENTATION PAGE		READ INSTRUCTIONS BEFORE COMPLETING FORM
1. REPORT NUMBER AFWL-TR-78-236	2. GOVT ACCESSION NO.	3. RECIPIENT'S CATALOG NUMBER
4. TITLE (and Subtitle) IMPROVEMENT OF SPECTER II CODE: INJECTION AND EVOLUTION OF AN ARTIFICIAL RADIATION BELT.		5. TYPE OF REPORT & PERIOD COVERED Final Report
		6. PERFORMING ORG. REPORT NUMBER LMSC/D634017
7. AUTHOR(s) J. B. Cladis, G. T. Davidson, W. E. Francis, L. L. Newkirk, and M. Walt		8. CONTRACT OR GRANT NUMBER(s) F29601-76-C-0095
9. PERFORMING ORGANIZATION NAME AND ADDRESS Lockheed Palo Alto Rsch Laboratory Space Science Laboratory 3251 Hanover St., Palo Alto, CA 94304		10. PROGRAM ELEMENT, PROJECT, TASK AREA & WORK UNIT NUMBERS 62704 WDNB4307
11. CONTROLLING OFFICE NAME AND ADDRESS Defense Nuclear Agency Washington, DC 20305		12. REPORT DATE August 1979
		13. NUMBER OF PAGES 192
14. MONITORING AGENCY NAME & ADDRESS(if different from Controlling Office) Air Force Weapons Laboratory (DYC) Kirtland Air Force Base, NM 87117		15. SECURITY CLASS. (of this report) Unclassified
		15a. DECLASSIFICATION/DOWNGRADING SCHEDULE

16. DISTRIBUTION STATEMENT (of this Report)

Approved for public release; distribution unlimited.

17. DISTRIBUTION STATEMENT (of the abstract entered in Block 20, if different from Report)

18. SUPPLEMENTARY NOTES

This research was sponsored by the Defense Nuclear Agency under Subtask S99QAXHC049, Work Unit 12, Trapped Radiation Assessment.

19. KEY WORDS (Continue on reverse side if necessary and identify by block number)

Nuclear Radiation, Space Radiation, Satellite Environments, Trapped Electron Injection, Argus Effect, Artificial Electron Belts, SPECTER Computer Code, Fission Debris Motion, Artificial Radiation Belt, Electron Radial Diffusion, Electron Belt Decay, and Radiation Belt Saturation.

20. ABSTRACT (Continue on reverse side if necessary and identify by block number)

Further improvements have been made in the SPECTER codes which compute the nuclear environment resulting from a high-altitude nuclear explosion and irradiation of satellites in that environment. A realistic model has been developed for the computation of fission-debris distribution in the magnetosphere. The model uses as input the distribution of debris and hot ionized air in the vicinity of the magnetic bubble. It computes the subsequent evolution of the distribution as the plasma expands along and across the

(over)

ABSTRACT (cont'd)

magnetic field. The motion across the magnetic field is determined by using an equivalent LCR circuit to find the ionospheric currents, which neutralize the transverse polarization fields. For a yield larger than 1 Megaton it was found that the tube containing the debris was convected outward from an initial L of 1.16 to beyond the maximum L value for trapping.

New coding has been incorporated to compute the redistribution of fission-decay electrons resulting from transport toward higher L values. The redistribution is computed by assuming conservation of the first and second adiabatic invariants. Low energy electrons are transported most efficiently to higher L-values. The consequent softening of the spectrum, as well as the spatial distributions, are in agreement with data for the Argus and Starfish tests.

The electron decay rates have been adjusted to take account of the flux limiting at high flux levels. The new decay model is based on a scheme proposed by Schulz, in which the diffusion rates near saturation revert to the strong diffusion limit.

The spatial and temporal regions have been identified wherein two or more separate nuclear explosions i) interact so that their trapping efficiencies are impaired, ii) are so close together that they can be regarded as a single burst, with summing of yields, or iii) can be regarded as independent.

The effects of radial diffusion on an artificial radiation belt were computed. Pitch-angle diffusion was simultaneously treated to account for the highly nonequilibrium early time distribution. Radial diffusion was found to be generally insignificant compared with pitch-angle diffusion and atmospheric loss below $L = 4$.

Recent contributions to the electron loss data base were surveyed. None of the recent data were found to be in a sufficiently advanced state of analysis to warrant incorporation in SPECTER at this time.

PREFACE

The SPECTER program has benefitted from the contributions of a large
number of persons in many institutions and locations. Foremost among
these is Dr. Charles A. Blank of Defense Nuclear Agency who guided the
program and provided support from its inception to the present. Since
Dr. Blank's retirement, his functions and responsibilities at DNA have
been assumed by Dr. Patrick Crowley. Direct responsibility for manage-
ment of the program at Air Force Weapons Laboratory rests with Mr. Joseph
F. Janni and project officer, Capt. Robert C. Backstrom; both of whom
have taken a strong personal interest in the program. Special commen-
dations are due Dr. Gary Cable, former project officer, now with Computer
Services Corporation, who has done much of the work of testing the com-
puter codes, and adapting them to new operational demands. Dr. Micheal
Schulz of Aerospace Corporation has diligently followed the progress of
the code development and provided many helpful suggestions and stimulating
ideas. The cooperation of Dr. R. Clark, Dr. K. Papadopoulos, Dr. J. D.
Huba, and others at Naval Research Laboratory has been vital to the under-
standing and treatment of early-time phenomena. Valuable contributions
were made at one time or another by others, not listed on the title page,
of the staff of the Space Sciences Laboratory of Lockheed Palo Alto Research
Laboratories; their assistance is deeply appreciated.

1/2

CONTENTS

CONTENTS (Continued)

ILLUSTRATIONS

5

ILLUSTRATIONS (Continued)

6

ILLUSTRATIONS (Continued)

TABLES

SECTION I

INTRODUCTION

The Specter computer codes, as described in references 1-3, determine the radiation environment resulting from a high-altitude nuclear explosion and the irradiation of satellites in that environment. This report describes recent improvements that have been made in the computation of the distributions of the nuclear debris and trapped fission-decay electrons in the magnetosphere, in the evolution of these distributions with time, and in the ultimate trapped-electron environment that may ensue in the event of a nuclear exchange.

A new electron injection model is described in Section II. It incorporates a model for the fission-debris distribution that is physically more realistic than the "confined" and "jetting" debris models that were used in the previous versions of the Specter codes. The magnetic tube containing the debris now convects outward, toward higher L values, owing to the enhanced plasma pressure in the tube. The trapped electrons, injected by the decay of the debris, drift outward as well as eastward while they reside in the debris tube. The redistribution of the electrons associated with their displacement in L is computed assuming conservation of the first two adiabatic invariants of the electron motion. Since the lower-energy electrons have lower eastward-drift velocities, they spend more time in the debris tube, and are therefore transported to higher L values. Accordingly, the energy spectra of the trapped electrons rapidly become softer toward higher L values. This result of the new injection model is in agreement with the nuclear-tests data; it constitutes a significant improvement in the computation of the trapped-electron distribution. A comparison of the computed fluxes with the nuclear-tests data is described in Section III.

As the population of trapped electrons increases due to injections by multiple nuclear explosions, the decay rate is expected to increase due to enhanced pitch-angle diffusion. This effect is taken into account by incorporating into

9

Specter an empirical model for the time-dependent loss rates based on the work of M. Schulz (Ref. 4). A discussion of this model together with the self-consistent flux levels for the saturation environment is given in Section IV. Section V treats the conditions under which two or more bursts interact such as to alter the injection efficiency of the individual bursts.

The trapped electron loss model in Specter is highly empirical, and makes no distinction between the various processes that remove electrons, such as pitch-angle diffusion at high altitudes and scattering in the atmosphere. There has been no attempt made until recently to include processes that redistribute electrons between adjoining L-shells. The new injection model, however, gives much improved radial distributions; accurate enough to warrant an investigation of subsequent processes that alter the distribution. Effects similar to those that lift the debris and electrons to high L-shells can also result in radial diffusion of trapped electrons. Radial diffusion is very important for energetic particles in the outer radiation belts. Section VI addresses the effects of radial diffusion on artificially injected electrons, and the corrections to the distribution that may be necessary.

The electron loss model is always subject to improvement as new data become available. The model is weak in some regions where adequate data have never been taken. This is especially true at low altitudes, particularly in the altitude region between the local and global cutoffs. New data are gradually appearing, however, and may soon warrant substantial revisions to the loss model. Section VII is an examination of the implications of new electron loss data to the Specter loss model. We review (in VII) the recent data bodies and describe (in VII.2) the comparison of the new injection model with both old and new data. A concluding subsection (VII.3) addresses the anticipated improvements and alterations that are needed to bring the model into agreement with the data. Recommendations for further improvements of the Specter codes are made in Section VIII.

SECTION II

NEW ELECTRON INJECTION MODEL

1. INTRODUCTION

In order to compute the initial distribution of the fission beta-decay
electrons which are injected into the radiation belt due to a high-altitude
nuclear detonation, it is necessary to know the spatial and temporal distri-
bution of the fission fragments. A new model has been developed for the
computation of the fission-debris distribution. This model is physically
more realistic than the "confined" and "jetting" debris models that were
previously used in the Specter Codes.

Briefly, the phenomenology of the ionized debris issuing from a nuclear
explosion above the sensible atmosphere of the earth is as follows. Initially,
the ionized debris expands radially against the geomagnetic field, forming a
magnetic bubble by excluding the field from the highly conductive plasma and
compressing it into a spherical shell. During the expansion and subsequent
collapse of the bubble, the ionized debris and energetic air ions escape from
the local entrapment and move toward higher and lower altitudes along the
earth's magnetic field. The bundle of field lines which contain the debris
and hot ionized air are referred to as the debris tube. Through the beta-
decay process, which is very rapid at early times, high fluxes of relativistic
electrons are emitted by the fission fragments. A large fraction of the
electrons become trapped in the debris tube. Owing to the configuration of
the geomagnetic field, the trapped electrons drift toward the east and the
ionized debris and air drift toward the west. The oppositely-drifitng
particles produce a charge separation across the tube. As depicted in Figure
1, a net positive charge forms at the western surface of the tube and a net
negative charge forms at the eastern surface. These charges produce an
electric field, E, in the debris tube directed toward the east, which causes
the debris to drift outward toward higher L values with the $\bar{E} \times \bar{B}$ drift velocity.
Hence, as the debris drifts outward, the emitted electrons drift eastward
forming the radiation belt. The process continues until the debris either enters
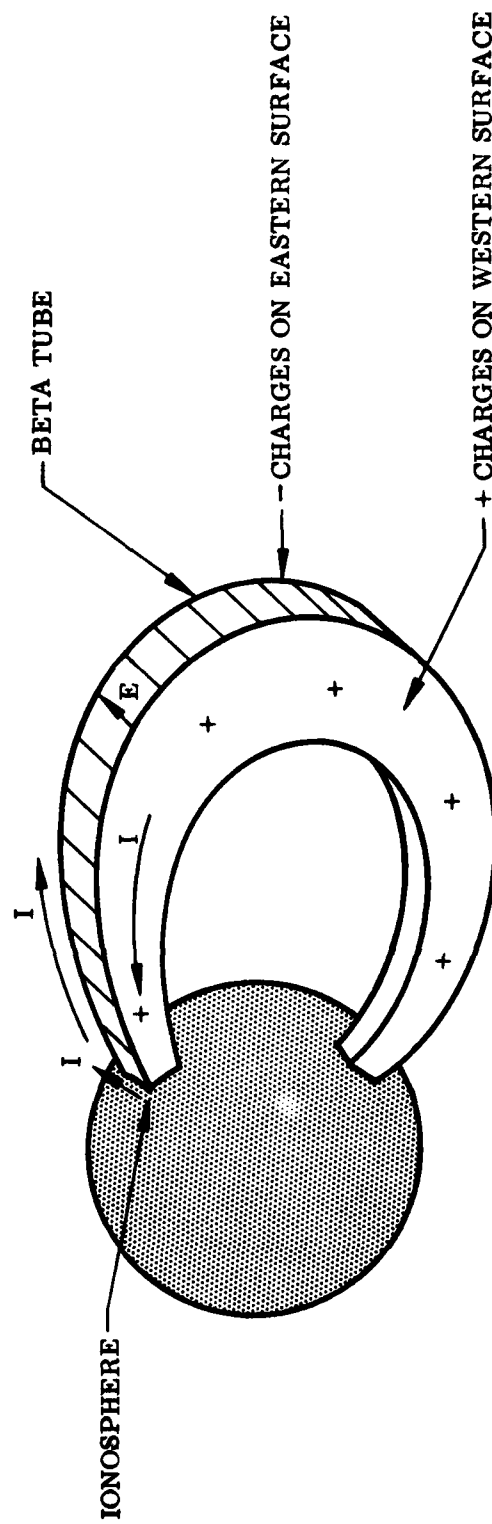
Figure 1. Illustration of electric field across debris tube and current tending to neutralize the excess charges.

12

the atmosphere because of its motion along the magnetic field or drifts outward beyond the boundary of the trapping region. The energy spectra of the trapped electrons become softer at the higher L values principally because the electrons become displaced upward in L before they drift out of the convecting debris tube, and the lower energy electrons reach higher L values because their eastward drift velocities are smaller.

The outward motion ($\bar{E}$ X $\bar{B}$ drift) of the debris depends sensitively on the coupling of the magnetosphere to the ionosphere. The charge separation across the tube tends to be neutralized by currents in the thermal plasma which, as shown in Figure 1, flow along magnetic field lines at high altitudes and across magnetic field lines in the ionosphere where the collision frequency is sufficiently high. The ionizing radiations from the nuclear device greatly increase the conductivity of the local ionosphere. This effect tends to dis- charge the tube, hence to retard the outward motion of the debris. On the other hand the neutralization current along the magnetic field may become so high that "anomalous resistivity" may develop along the field lines in the upper ionosphere. Such a resistivity, which is due to a plasma instability (Refs. 5-9) tends to decouple the tube from the ionosphere, hence to attenuate the neutralization process.

In the new injection model, the computation of the outward motion of the debris is based on the assumption that magnetic field lines are equipotentials. This assumption greatly simplifies the problem because the debris remains in a magnetic flux tube. The neutralizing effect of the ionospheric current is determined by using an equivalent electrical circuit to computer the net charge across the tube. This circuit consists of the effective capacitance and inductance of the magnetic tube and the variable resistance of the current path through the ionosphere. It is driven by the azimuthal drift current due to the trapped electrons and the ionized debris and hot air.

The injection model takes as input the velocity and spatial distribution of the debris and hot ionized air escaping from the magnetic bubble. These data were supplied by the Naval Research Laboratory. The model then computes the distribution of the debris in the magnetosphere by combining the motion of the debris along the magnetic tube with the cross L motion of the tube. Finally,

13

the debris distribution — specifically, the number density of the fission fragments as a function of B, L, and time — are used to compute the trapped electron distribution, including the redistribution of the electrons resulting from the motion of the debris tube.

2. MODEL OF CROSS-L MOTION OF DEBRIS

a. Equipotential Field Lines

Owing to the highly complex behavior of a dense, high-energy plasma injected into the magnetosphere, some simplifying assumptions must be made to estimate the motion of the nuclear debris. One approximation that is made is that the magnetic field lines containing the debris are equipotentials. This approximation is commonly made in magnetospheric physics because mobilities of the thermal charged particles are usually very high along magnetic field lines above the "sensible" atmosphere. Accordingly, the thermal-plasma constituents become redistributed rapidly along the field lines and tend to maintain the potential the same all along the field line. This approximation, as discussed in Section III, is good for low and intermediate-yield bursts. For high-yield bursts, however, this assumption may overstate the debris at low altitudes that drifts to higher L values.

The equipotential field-line approximation, however, greatly simplifies the computation of the debris motion. If the field lines are equipotentials, the debris drifts outward to higher L values as though the magnetic tube on which the debris is injected convects upward preserving its magnetic flux and dipole-like configuration. This behavior of the plasma can be shown as follows. Consider the debris to be located initially in a magnetic tube which has a center line that crosses the equator at the geocentric distance r_0 (see Figure 2). The argument above requires that if the field lines are equipotentials and the electric field in the tube is directed toward the east, every element of the plasma along the tube will drift in the local $\bar{E} \times \bar{B}$ direction at the speed E/B such that it will reach a magnetic tube which has a center line that crosses the equator at $r_0 + \Delta r_0$ in the time Δt. It is therefore necessary to show that,

14
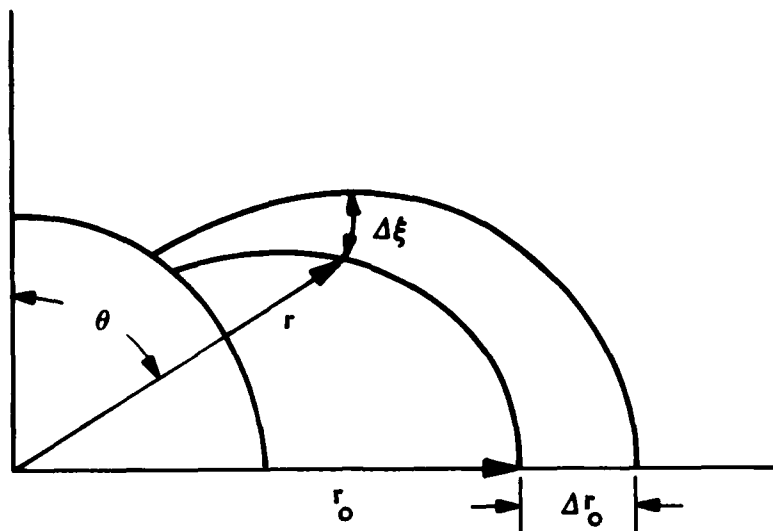
Figure 2. Illustration of motion of magnetic tube.

$$\Delta t = \frac{\Delta \xi}{E/B} = \frac{\Delta r_o}{E_o/B_o} \tag{1}$$

where   is the displacement of the plasma element that was located along the initial tube at the coordinates 4, . The subscript o refers to quantities at the equator ($\theta = 90^o$). Conservation of magnetic flux in a dipole field requires that,

$$B \ \Delta \xi \ r \ \sin \theta \ \Delta \phi = B_o \Delta r_o r_o \Delta \phi \tag{2}$$

or
$$\Delta \xi = \frac{B_o r_o}{B \ r \ \sin \theta} \ \Delta r_o \tag{3}$$

In Eq. (2) $\Delta \phi$ is the azimuthal width of the tube. Since the field lines are equipotentials,

$$V = e \ r \ \sin \theta \ \Delta \phi = E_o r_o \Delta \phi \tag{4}$$

or
$$E = \frac{E_o r_o}{r \ \sin \theta} \ . \tag{5}$$

Hence, by substituting (3) and (5) in (1), Eq. (1) is verified. Note that the above equations hold for any axisymmetric magnetic field.

15

b. Equivalent Electrical Circuit

The model of the debris motion is further simplified by using an equivalent
electrical circuit to compute the excess charge, hence the electric field
across the tube. The circuit is used principally to account for the ionospheric
current which tends to neutralize the charge across the tube. It also accounts
for the polarization of the thermal plasma at high altitudes that also reduces
the excess charge. The circuit is shown in Figure 3.
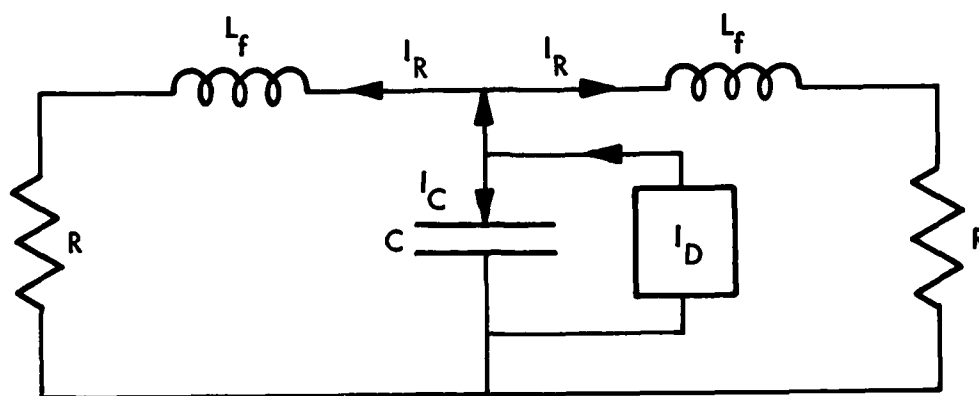
Figure 3. Equivalent electrical circuit.

Here, C is the capacitance of the tube (the excess charge on the tube
boundaries shown in Figure 1 divided by the voltage across the tube); L_f is
the inductance of the current-flow path shown in Figure 1, from the equator
to the ionosphere; and R is the effective resistance of the current path.
The current I_D is the azimuthal drift current due to the injected electrons
and energetic ions; I_C is the current which establishes the excess charge
across the tube (the current through the capacitor); and I_R is the field-
aligned current which tends to neutralize the excess charge. The effect of
the polarization current is taken into account as discussed below by using
an appropriate dielectric constant.

16

(1)   Capacitance

The capacitance of a small section of the tube of length ΔS along the
magnetic field, "height" $\Delta \xi$ normal to $\bar{B}$ in the magnetic meridian, and "width"
$r \sin \theta \, \Delta \varphi$, is given by the equation,

$$\Delta C = k k_o \frac{\Delta \xi \, \Delta S}{r \sin \theta \, \Delta \varphi} \tag{6}$$

where k is the dielectric constant of the plasma and k_o is the permittivity of
free space (8.85×10^{-12} farads/m). For the time scale of the tube motion, the
effective dielectric constant of the plasma is,

$$k = 1 + \rho/k_o B^2 \tag{7}$$

where ρ is the density of the plasma in kg/m^3 and B is the magnetic field
intensity in W/m^2. Since $\rho/k_o B^2 \gg 1$,

$$k \, k_o \approx \frac{\rho}{B^2} \ . \tag{8}$$

From Eq. (3), the ratio of the "height" to the width of the tube
section is

$$\frac{\Delta \xi}{r \sin \theta \, \Delta \varphi} = \frac{B_o}{B \sin^6 \theta} \ \frac{\Delta r_o}{r_o \Delta \varphi} \tag{9}$$

when the dipole-field expression for r is used:

$$r = r_o \sin^2 \theta \ . \tag{10}$$

But, again for a dipole field,

$$B \sin^6 \theta = B_o (1 + 3 \cos^2 \theta)^{\frac{1}{2}}. \tag{11}$$

Hence,

$$\frac{\Delta \xi}{r \sin \theta \, \Delta \varphi} = \frac{1}{(1 + 3 \cos^2 \theta)^{\frac{1}{2}}} \ \frac{\Delta r_o}{r_o \Delta \varphi} \ . \tag{12}$$

17

Since the magnetic bubble is nearly spherical in shape, the ratio of the "height" to the width of the section containing the burst point ($\theta=\theta*$) is taken to be 1 for the initial position of the tube. Thus,

$$\frac{\Delta r_o}{r_o \, \Delta\varphi} = (1 + 3 \cos^2 \theta*)^{\frac{1}{2}}. \tag{13}$$

When the tube moves to L values away from its initial location, L_o, conservation of magnetic flux requires that Δr_o increase as L^2 whereas $r_o \, \Delta\varphi$ increases as L. Therefore, in general,

$$\frac{\Delta \xi}{r \sin \theta \, \Delta\varphi} = \left(\frac{1 + 3 \cos^2\theta^*}{1 + 3 \cos^2\theta} \right)^{\frac{1}{2}} \frac{L}{L_o}. \tag{14}$$

By substituting (8) and (14) into (6) and summing, the initial capacitance of the tube is given by the equation

$$C(t=0) = \sum_k \frac{\rho_k}{B_k^2} \left(\frac{1 + 3 \cos^2 \theta_k^*}{1 + 3 \cos^2 \theta_k} \right)^{\frac{1}{2}} \Delta S_k. \tag{15}$$

At later times it is necessary to take into account the fact that the initial ambient plasma in each section of the tube remains approximately in that section while the tube moves. Hence, the ambient plasma mass, $\rho_k^{(A)} A_k \Delta S_k \propto \rho_k \Delta S_k / B_k$ is a constant of the motion. (A_k, the cross sectional area of the tube section, is proportional to $1/B_k$). Hence, the general expression for the tube capacitance is,

$$C(t) = \sum_k \left[\left(\frac{\rho_k^{(A)} \Delta S_k}{B_k} \right)_{t=0} \cdot \frac{1}{B_k} + \frac{\rho_k^{(H)} \Delta S_k}{B_k^2} \right] \left(\frac{1 + 3 \cos^2 \theta_k^*}{1 + 3 \cos^2 \theta_k} \right)^{\frac{1}{2}} \frac{L}{L_o} \tag{16}$$

where $\rho_k^{(H)}$ is the density of the energetic ions in the kth section. All of the quantities in this expression vary with time with the exceptions of θ_k^*, L_o and the invariants within the brackets designated by the subscript t=0.

A model of the ambient plasma density in the magnetosphere with its dependence on the local time, season, and phase of solar activity has been developed to compute the tube capacitance. The model incorporates a computer program written by Dr. Y.T. Chiu of the Aerospace Corporation (Ref. 10) that

18

computes the electron number density in the altitude range 90-500 km.
This code includes the diural, annual, and solar-activity cycle variations.
The electron number density is then set equal to the sum of the number den-
sities of the principal ions in that altitude range, i.e. O_2^+, NO^+, and O^+,
and the plasma density is computed by using published data (e.g. Johnson,
Ref. 11) on the fractional abundances of the ions.

At altitudes above 500 km extensive data on ion-densities are available
only from satellite measurements at altitudes near 1000 km and at regions
near the equator. Accordingly, the following procedure is used to compute
the ion density.

The L value of the plasmapause is determined from the whistler data
(Ref. 12) on the mean location of the plasmapause as a function of local time.
For L values below the plasmapause, the ion densities (O^+, He^+, and H^+) are
extrapolated upward along the magnetic field assuming diffusive equilibrium
and computing scale heights based on the ion temperatures at 500 km. The
same method is used for the altitude region 500 km $\leq$ h $\leq$ h_t beyond the plasma-
pause, where h_t is the "transition" altitude, the altitude in the mid-latitude
trough where the principal ionic constituent changes from H^+ at the lower lati-
tudes to O^+ at the higher latitudes. The transition altitude is computed
from a model based on the work of Titheridge (Ref. 13). At latitudes beyond
the O^+/H^+ transition region, the O^+ ion density is computed from the scale
height as discussed above, but the He^+ and H^+ densities are interpolated
along the magnetic field using the satellite measurements at the equator
and near 1000 km. In the interpolation procedure a B^n variation of the
plasma density along the magnetic field is assumed.

Typical results given by the model are shown in Figures 4 through 7
for a variety of geographic positions, local times, seasons, and solar
activity. Figure 4 shows the computed concentrations of O_2^+, NO^+, O^+, He^+,
and H^+ ions, and the total ion concentration, N_I^+, at altitudes below 500 km.
The results are for the local time 1200, the month of December, and the
geographic coordinates of 0° latitude and 280^oE longitude. Figure 5
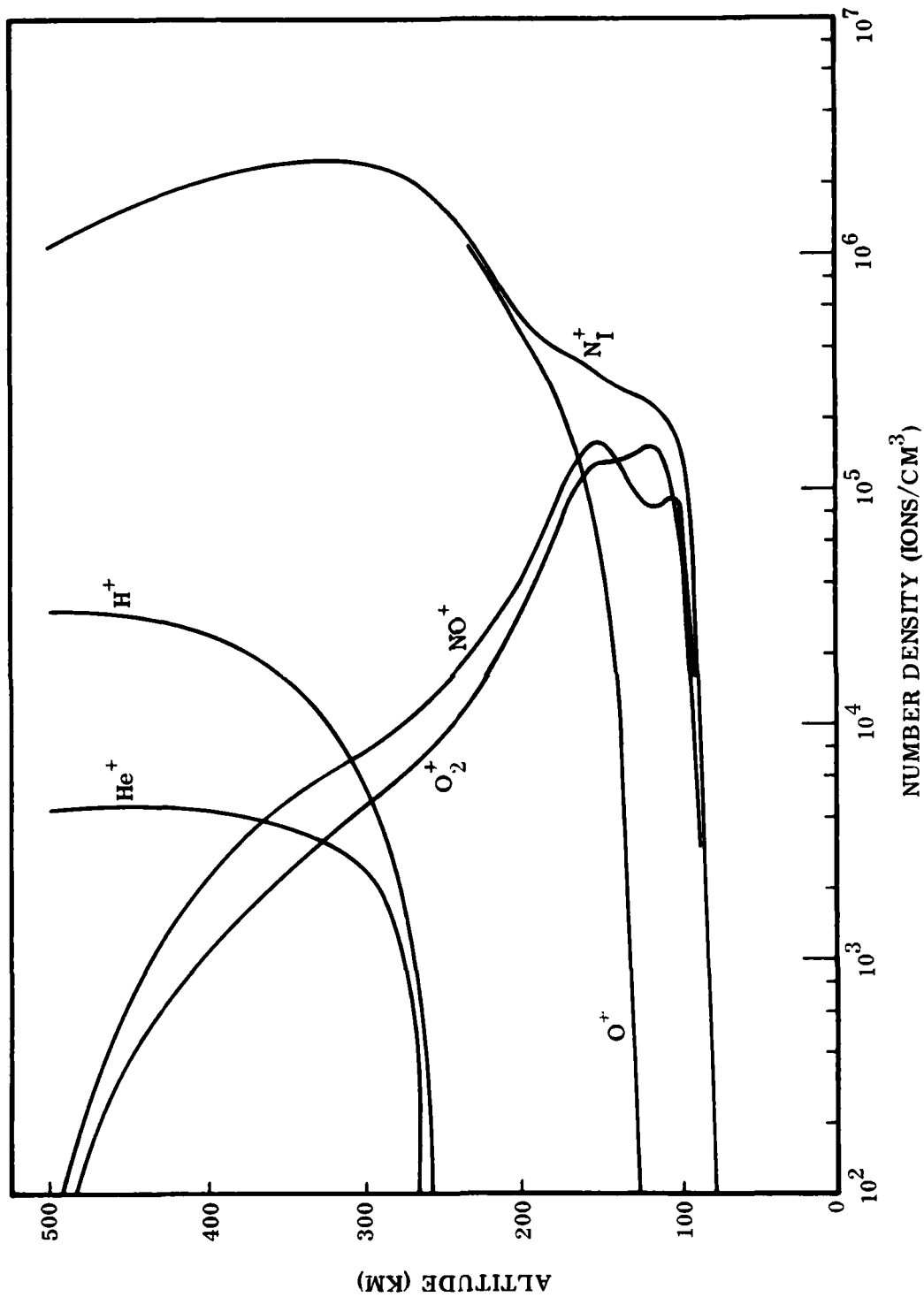
Figure 4. Concentrations of ionic constituents at altitudes below 500 km at noon in December at Latitude 0°, Longitude 280°E.

20
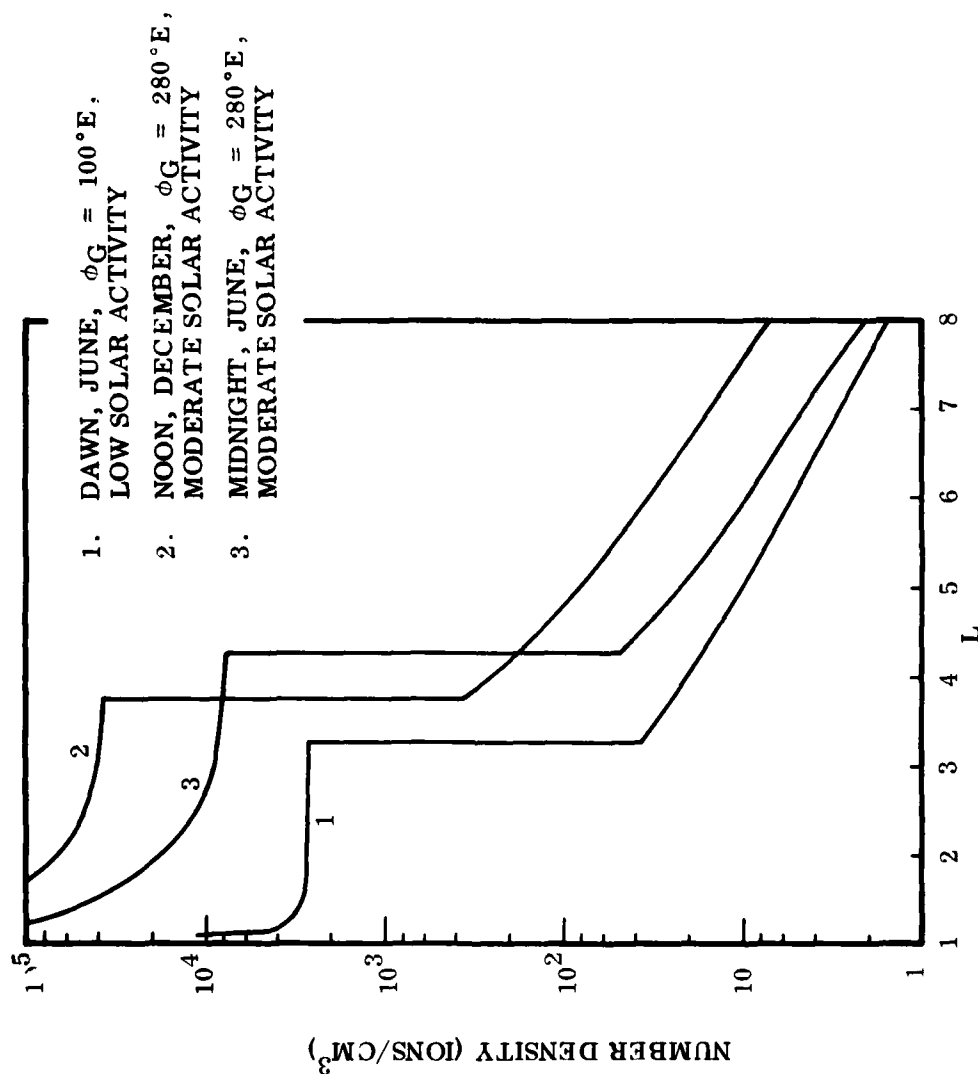
Figure 5. Equatorial distributions of total ion concentrations. Curve 1 is for dawn in June at geographic longitude of 100°E and for conditions at low solar activity. Curve 2 is for noon in December at geographic longitude of 280°E and for moderate solar activity. Curve 3 is for midnight in June at geographic longitude of 280°E and for moderate solar activity.
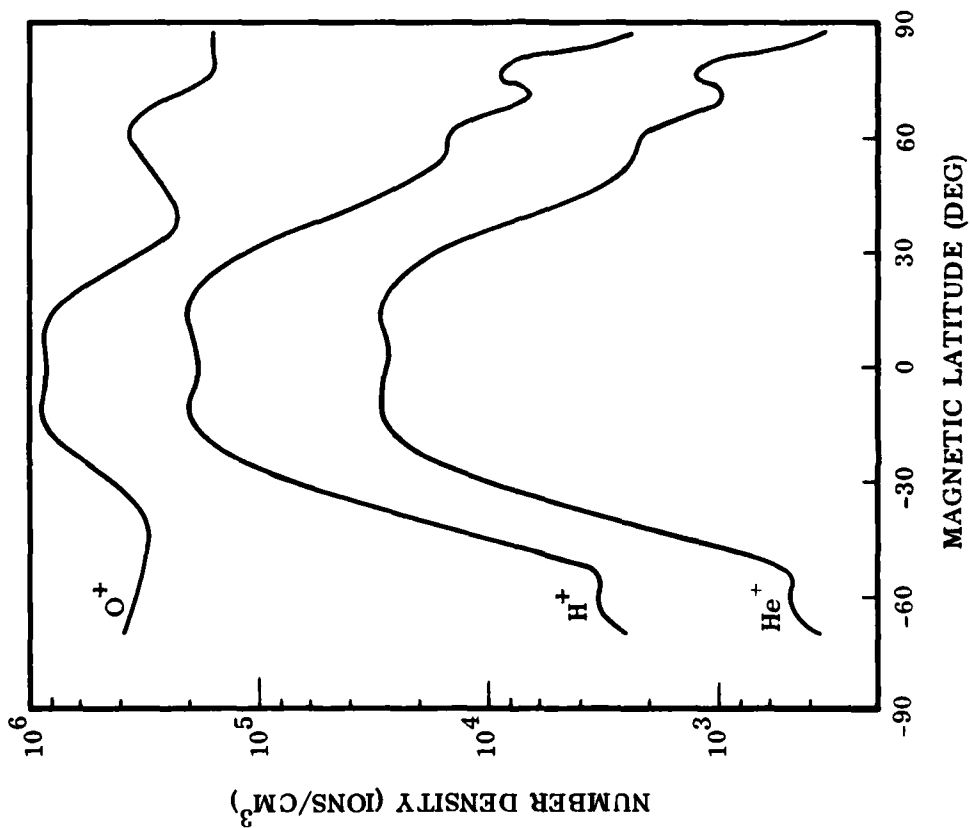
Figure 6. O^+, H^+, and He^+ ion concentrations vs. magnetic latitude at an altitude of 500 km along the geographic meridian 280° East Longitude at local noon in December.

22
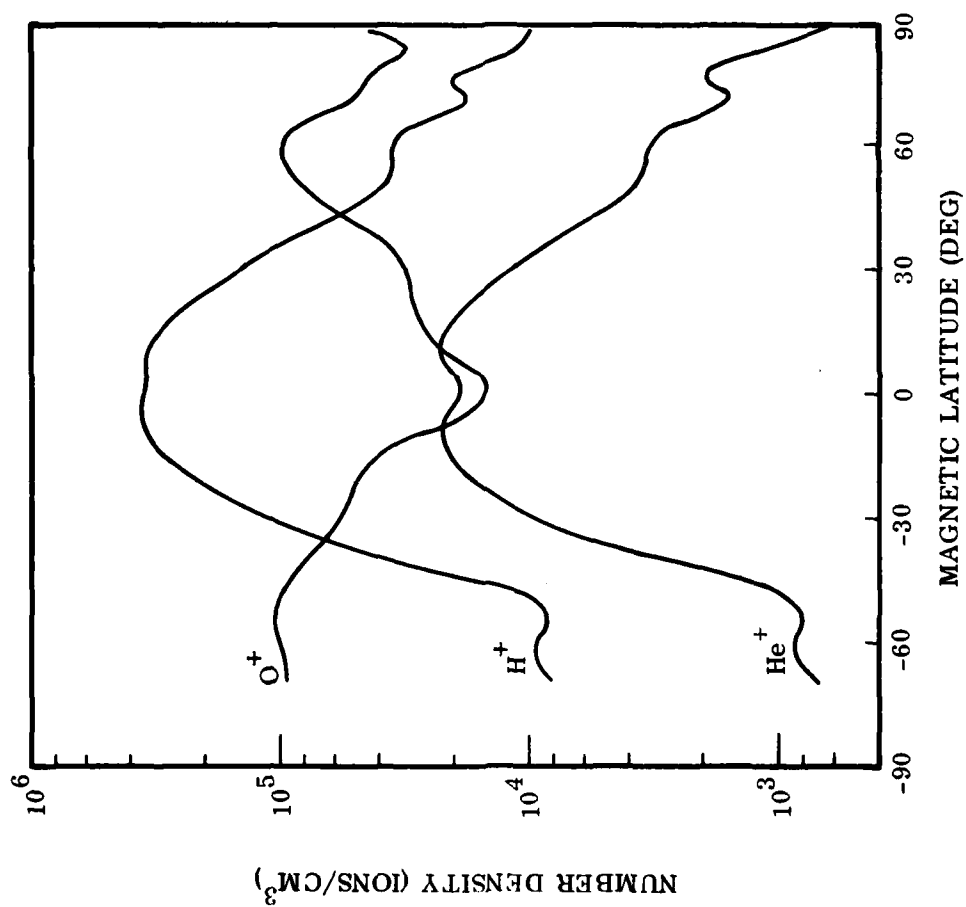
Figure 7. O^+, H^+, and He^+ ion concentrations vs. magnetic latitude at an altitude of 1000 km for conditions described in caption of Figure 4.

23

illustrates the radial variation of the total ion concentration at the equator
for several combinations of the available parameters (local time, month,
geographic position, and solar activity). This figure clearly indicates
the plasmapause positions. Figures 6 and 7 illustrate the O^+, He^+, and H^+
ion concentrations in a geographic meridian as a function of magnetic latitude
at altitudes of 500 and 1000 km, respectively. The high-latitude, light-ion
trough is visible in Figure 7. Here, the light ions, H^+ and He^+, are depleted
through their outward flow and convection out of the magnetosphere, and the O^+
ions become dominant at 1000 km.

The tube capacitance due to the ambient plasma alone is shown as a
function of L in Figure 8. The results are shown for local times of noon and
midnight, the months of December and June during moderate solar activity,
and for the geographic longitude of 100^OE. As expected, the capacitance
rapidly increases as the lengths of the field lines that thread plasma increase
above the 100 km level, reaches a local maximum for field lines that lie in
much of the F-layer, then decreases above the F-layer as shorter sections of
the field lines lie in the dense ionosphere. At higher L values the B^2
factor in the denominator of Equation (16) causes the capacitance to increase
again beyond the local minimum at $1.5 \leqslant L \leqslant 1.7$. The sharp reduction near
L=4 is, of course, due to plasma reduction beyond the plasmapause. In addition
to the differences in the capacitances shown in the figure due to the local
time and season, the capacitances are also sensitive, especially at $L \leqslant 2.5$,
to geographic longitude. Near the Atlantic geomagnetic anomaly, the capaci-
tances for $L \leqslant 2$ are lower than those shown in Figure 8 by about an order of
magnitude.

(2)   Inductance

If the surfaces of the tube containing the excess charge are regarded
to be rigid conductors, the inductance of the circuit carrying the neutralizing
current (See Figure 1) is, approximately,

$$L_f = \frac{4}{\pi^2} \mu_o S_o \qquad (17)$$

24
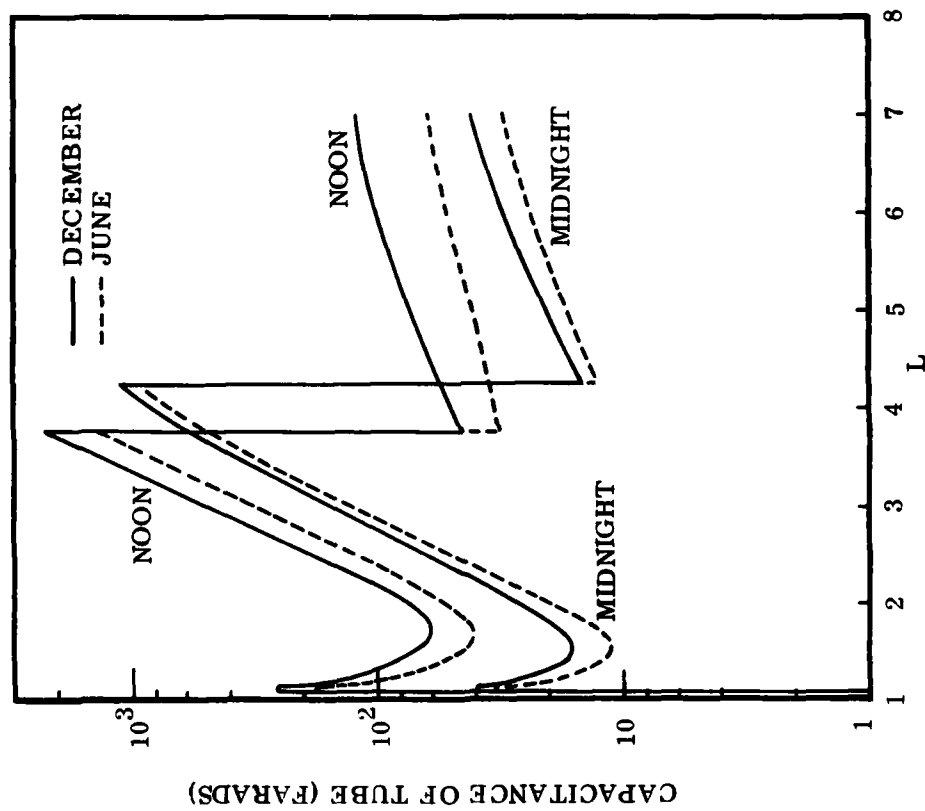
Figure 8. Ambient capacitance vs. magnetic L-value for the local times noon and midnight and months of June and December along a geographic longitude of 100°E.

25

where μ_0 is the permeability of free space ($4\pi \times 10^{-7}$ H/m), and S_0 is the length in meters of the field line from the E-region of the ionosphere to the equator. For a dipole magnetic field,

$$S_0 = \frac{r_0}{2} \left[x\sqrt{1 + 3x^2} + \frac{1}{\sqrt{3}} \ln\left(\sqrt{3}\,x + \sqrt{1 + 3x^2}\right) \right] \qquad (18)$$

where r_0 is the geocentric distance to the field line crossing of the equator, and $x = \sin \Lambda$.

$$\Lambda = \cos^{-1}\left(\frac{1 + h/r_E}{L}\right)^{\frac{1}{2}} \qquad (19)$$

Where h is the altitude of the E-region of the ionosphere ($\approx$ 110 km), r_E is the radius of the earth, and L is the L value of the field line.

(3)   Resistance
(a)   Undisturbed Ionosphere

When the tube has drifted to regions away from the burst where the ionosphere is not appreciably perturbed by the nuclear explosion, the following equations are used to compute the resistance R:

$$R = \frac{\Sigma_1}{\Sigma_1^2 + \Sigma_2^2} \qquad (20)$$

where Σ_1 and Σ_2 are the height integrated Pederson and Hall conductivities, respectively.

$$\Sigma_1 = \int_{h_i}^{h_f} \sigma_1 \, dh, \qquad (21)$$

$$\Sigma_2 = \int_{h_i}^{h_f} \sigma_2 \, dh, \qquad (22)$$

$$\sigma_1 = n_e e^2 \left[\frac{\nu_e/m_e}{(\nu_e^2 + \omega_e^2)} + \sum_i \frac{n_i}{n_e} \frac{\nu_i/m_i}{(\nu_i^2 + \omega_i^2)} \right], \qquad (23)$$

26

$$\sigma_2 = n_e e^2 \left[\frac{-\omega_e/m_i}{(\nu_e^2 + \omega_e^2)} + \sum_i \frac{n_i}{n_e} \frac{\omega_i/m_i}{(\nu_i^2 + \omega_i^2)} \right],$$ (24)

$$\nu_e = \nu_{en} + \nu_{ei} ,$$ (25)

$$\nu_{en} = 5.4 \times 10^{-10} \, n_n \, T_e^{\frac{1}{2}}, \quad \text{(Ref. 49)}$$ (26)

$$\nu_{ei} = [34. + 4.18 \, \log_{10}(T_e^3/n_e)] \, n_e T_e^{-3/2}, \quad \text{(Ref. 49)}$$ (27)

$$\nu_i = \nu_{in} = 2.6 \times 10^{-9} (n_n + n_i)/\sqrt{M} , \quad \text{(Ref. 50)}$$ (28)

$$M = \sum n_i W_i / \sum n_i ,$$ (29)

$$n_n = \rho_n/M ,$$ (30)

$$\omega_e = eB/m_e,$$ (31)

and

$$\omega_i = eB/m_i ,$$ (32)

where Σ_1 and Σ_2 are in abmohs, σ_1 and σ_2 are in abmohs/cm, $e = 1.602 \times 10^{-20}$ emu, $n_e = \sum_i n_i$, T_e is the electron temperature in $^\circ$K, m_i = ion mass in gm, $m_e = 9.1058 \times 10^{-28}$ gm, ν_{en} is the electron-neutral collision frequency, ν_{ei} is the electron-ion collision frequency, ν_i is the ion-neutral collision frequency, M is the mean molecular weight of the ions, ρ_n is the neutral density in gm/cm^3, B is the magnetic-field intensity in gauss, ω_e is the electron-cyclotron frequency, ω_i is the ion-cyclotron frequency, W_i is the molecular weight of the i th ion species, $h_i = 80 \times 10^5$ cm, and $h_f = 400 \times 10^5$ cm. Using these values, Eq. (20) must be multiplied by 10^{-9} to obtain R in ohms.

The variables required for the calculation of R are the geographic position of the foot of the flux tube containing the burst, the local time, the 10 cm solar flux, and the temperature T_e (this is assumed to remain constant).

Eq. (20) gives values near the equator that vary from about 0.7 ohms to 0.06 ohms through the local time sector 0-6 hrs.

(b)   Disturbed Ionosphere

A nuclear burst at altitudes within several thousand kilometers decreases this resistance by many orders of magnitude. Recombination proceeds rapidly at low altitudes, but at the altitudes of the effective E-region of the ionosphere the conductivity remains extremely high for tens to hundreds of seconds. For the equivalent electrical circuit under consideration — a series resonant circuit — the resistance does not appreciably influence the voltage across the capacitor, hence the tube motion, if,

$$R << \frac{2L_f}{\sqrt{L_f C/2}} \tag{33}$$

Note that the period of the resonant circuit is:

$$\tau = 2\pi \sqrt{L_f C/2} \approx 2\pi \left[\frac{4}{\pi^2} \mu_o S_o \int_o^{S_o} \frac{\rho}{B^2} ds \right]^{1/2} \tag{34}$$

And for ρ/B^2 = constant along the field, Eq. (34) becomes,

$$\tau = 4 S_o / V_A \tag{35}$$

where V_A is the Alfvén velocity,

$$V_A = B / \sqrt{\mu_o \rho} \tag{36}$$

Hence, the inequality (33) becomes,

$$R << \frac{4}{\pi} \mu_o V_A = 1.6 \times 10^{-6} V_A \tag{37}$$

V_A is about 10^6 m/sec in the natural magnetosphere, but the injected ions will reduce the Alfvén velocity in the debris tube, perhaps by as much as an order of magnitude. Therefore, the tube motion will be insensitive to the value of R

28

if $R << \sim .2\ \Omega$, i.e., if R is about 0.02 Ω or less.

This circumstance is fortunate because the resistance of the ionospheric path after a nuclear explosion is difficult to compute accurately and it changes rapidly in time. Eq. (37) indicates that the resistance may be set equal to zero until the foot of the debris tube in the ionosphere moves away from the sub-burst point by about 1500 km, where the ionosphere would not be disturbed appreciably and the value of R given by Eq. (20) would apply.

<div align="center">(c)   Anomalous Resistivity</div>

As mentioned in the introduction, anomalous resistivity may develop along the current path above the ionosphere if the burst yield is sufficiently high. Kindel and Kennel (Ref. 5) have shown that field-aligned currents of 2×10^{-5} to 2×10^{-6} Amps/m^2 can destabilize ion cyclotron waves within a wide range of the electron to ion temperature ratio and for critical drift velocities of the current carriers that are a small fraction ($\geqslant 0.1$) of the electron thermal velocity. The resulting ion cyclotron turbulence would produce anomalous resistivity and cause high electrostatic potential differences to appear along the magnetic field across the turbulent region. These predictions have been verified recently in the auroral region with data obtained with the Air Force S3-3 satellite. On repeated passes at high latitudes, simultaneous observations are made of field-aligned currents of $\sim 10^{-6}$ Amps/m^2, electrostatic ion cyclotron waves, plasma turbulence, and electrostatic potential differences of several kV along the magnetic field (Refs. 6 - 8). In analyzing these data, Hudson et al. (Ref. 9) infer an anomalous resistivity $\eta = 100$ ohm-m compared with the classical resistivity at the satellite altitude of 1.5×10^{-3} ohm-m.

For the MT-yield test devices, the field aligned current was of the order of 10^5 Amps/(150 km $\times$ 15 km) $\approx 5 \times 10^{-5}$ Amps/m^2. Hence, the essential criterion for the instability is met. If we assume the anomalous resistivity to be 100 ohm-m and to extend for a distance d $\approx$ 1000 km along the field as observed in the auroral zone, then the total resistance along the field would be R = ηd/A $\approx 100 \times 10^6$ m/2 $\times 10^9$ m^2 = .05 ohms. This value of R is so small that it will not appreciably affect the tube motion, and it is not taken into account in the

<div align="center">29</div>

injection model. However, the potential drop along the field established by the resistivity reduces the $\overline{E} \times \overline{B}$ drift motion of the debris at low altitudes relative to that computed by the model. This effect is discussed in Section III.

c. Motion of Debris Tube

As discussed in Section II.2.a., the assumption that the magnetic field lines are equipotentials allows one to determine the cross-L distribution of the debris by computing the motion of the magnetic flux tube containing the debris. Using the symbols defined in Section II.2.a., the tube moves in L at the rate,

$$\frac{dL}{dt} = \frac{\cdot E_o}{B_o \, r_E} \tag{38}$$

Since,

$$E_o = -\frac{V}{r_E \, L \, \Delta \varphi} \tag{39}$$

$$V = Q / C \tag{40}$$

and

$$B_o = B_E / L^3 \tag{41}$$

where B_E is the field intensity at the equator (3.12×10^{-5} W/m^2), Eq. (38) may be written as,

$$\frac{dL}{dt} = \frac{Q \, L^2}{r_E^2 \, B_E \, C \, \Delta \varphi} \tag{42}$$

Q is the net charge across the tube. It is given by the solution of the circuit equation,

$$L_f \, \frac{d^2 Q}{dt^2} + R \, \frac{dQ}{dt} + \frac{2Q}{C} = L_f \, \frac{dI_D}{dt} + RI_D \tag{43}$$

As discussed above, L_f, R, C, as well as I_D, are, in general, functions of time.

In an attempt to verify a code (TUBE) that was written to compute the tube motion, the values of L_f, R, and C were taken to be constants, with $R/2L_f < (L_{f2}\frac{C}{2})^{-1/2}$, and the right hand side of (43) was also set equal to a constant, F. The exact solution of (43) is then,

$$Q = \frac{CF}{2} \left[1 - \frac{e^{-\alpha t}}{\omega} (\alpha \sin \omega t + \omega \cos \omega t) \right] \qquad (44)$$

where $\alpha = R/2L_f$ and $\omega^2 = 2/L_f C - \alpha^2$ and the exact solution of (42) is

$$\frac{1}{L} = \frac{1}{L_o} - \frac{F}{r_E^2 B_E \Delta \varphi} \left\{ t + L_{f2}\frac{C}{2} \left[e^{-\alpha t}(2\alpha \cos \omega t - (\frac{\omega^2 - \alpha^2}{\omega}) \sin \omega t) - 2\alpha \right] \right\} \qquad (45)$$

The results of this test are given in Table 1 which list the exact value of L computed from Eq. (45) with the numerical solution obtained by TUBE with a time step of 0.3 sec. The parameters were R = 1 Ω, L_f = 4.64 h, and C = 10 f.

Table 1

Comparison of Numerical and Exact Solutions of Differential Equation

t sec.	L exact	L computed	ΔL error
0.0	1.8000	1.8000	.0000
6.0	1.8096	1.8096	.0000
12.0	1.8594	1.8594	.0000
24.0	1.9714	1.9716	.0002
36.0	2.0058	2.0060	.0002
48.0	2.1571	2.1574	.0003
60.0	2.2018	2.2023	.0005

31

d. Azimuthal Drift Current

(1)   Drift Current Due to Ionized Debris

The azimuthal drift current of the hot ions (debris and hot air) at the western face of the debris tube is,

$$I_D^h = q \frac{dN}{d\phi} \dot{\phi}_D \qquad (46)$$

where q is the mean charge of the hot ions, $dN/d\phi$ is the azimuthal gradient of the energetic ions, and $\dot{\phi}_D$ is the mean azimuthal drift velocity (radians/sec) of the hot ions. I_D^h is in Amperes if q is in Coulombs. The hot ions will be assumed to be uniform in every cross sectional area A, of the tube normal to the field. Hence, Eq. (46) can be written as,

$$I_D^h = \frac{q}{\Delta \phi} \int n_H (v, s) A(s) \dot{\phi}_D (v, s) ds \qquad (47)$$

where $\Delta \phi$ is the width of the debris tube, $n_H (v,s)$ is the number density of the hot ions at point s along the magnetic field (ion velocity is v at that point), A(s) is the cross sectional area of the tube at s, and $\dot{\phi}_D (v, s)$ is the azimuthal-drift velocity of the hot ions at s. The integration is over the entire length of the tube above an altitude of 200 km.

If a net force $\bar{F}$ acts on a charged particle over its gyro motion, the particle drifts with a velocity $\bar{F} \times \bar{B}/q B^2$.

The hot-ion velocity, as discussed in Section II.3, is principally along the field, hence the force F is essentially equal to the centrifugal force Mv^2/R. Thus,

$$\dot{\phi}_D = \left(\frac{Mv^2}{R} \right) \frac{1}{qBr\cos \lambda} \qquad (48)$$

where M is the mean mass of the hot ions, and R is the radius of curvature of the field line at s. Note that the particle charge cancels when $\dot{\phi}_D$ is put into Eq. (47). Hence, information on the degree of ionization of the hot ions is not required.

32

For a dipole field,

$$RBrcos\ \lambda\ = \left(\frac{B_E r_E^2}{3L}\right)\ \frac{(1 + 3u)^2}{1 - u^2} \tag{49}$$

where

$$u\ = sin^2\ \lambda \tag{50}$$

Hence,

$$I_D\ =\ \frac{3\ LM}{B_E r_E^2\ \Delta\ \varphi}\quad \int n\ v^2\ A(s)\ f(u)\ ds \tag{51}$$

where,

$$f(u)\ =\ \frac{1 - u^2}{(1 + 3u)^2} \tag{52}$$

The mean mass, number density, and velocity of the hot ions at s are computed as described in Section II.3 from the ion distributions provided by NRL at certain reference planes, normal to the magnetic field, above and below the burst point.

Since the ions in the burst-point region, between the reference planes, are temporarily trapped. their velocities are mainly perpendicular to the magnetic field. The net force F is then $1/2\ MV^2/R$, derived from the product of the ion magnetic moment and the perpendicular gradient of the magnetic field. Hence, $\dot{\phi}_D$ is just one-half that given by Eq.(48). Moreover, since the interval between the reference planes is small, the integral (47) for the hot ions in that region, i.e.,

$$I_D^h\ =\ \frac{3L}{r_E^2 B_E\ \Delta\ \varphi}\quad \int (1/2\ Mv^2)\ n_H af(u)\ ds \tag{53}$$

is taken to be,

$$I_D^h\ =\ \frac{3L\ W(t)\ f(u*)}{r_E^2 B_E\ \Delta\ \varphi} \tag{54}$$

33

where $W(t)$ is the kinetic energy of the hot ions remaining between the reference planes at time t, and $f(u*)$ is given by Eqs. (52) and (50) evaluated at the burst point latitude, $\lambda*$.

(2)   Drift Current Due to Injected Electrons

The azimuthal drift current of the electrons is somewhat more difficult to determine analytically. For this case the general expression, (47), for the electron drift current at the eastern face of the debris tube, where $\varphi = \omega_2$ as shown in Figure 9,
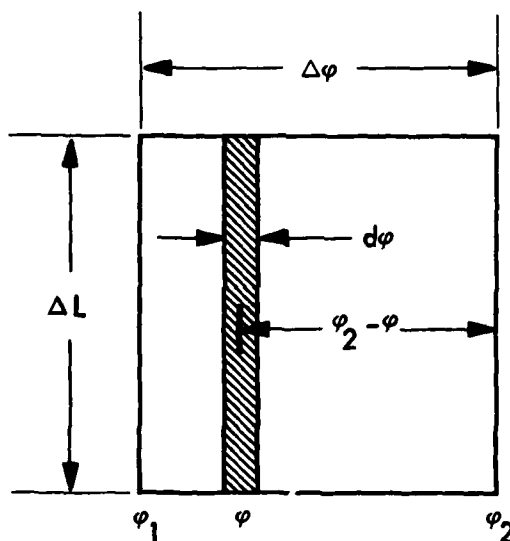
Figure 9.   Schematic diagram of tube cross section illustrating computation of electron drift current at $\phi = \phi_2$.

may be written as,

$$I_D^e(t) = \frac{q}{\Delta \omega} \int_0^\infty dw \int_0^{T(w)} S_e(t-t')R(t-t')G(w;t-t')\dot{\phi}_D(w)dt' \qquad (55)$$

where q is now the electron charge,

$$S_e(t) = 6 \int n_f(s, t) \, A(s) \, \frac{\Delta \Omega(s)}{4\pi} \, ds \tag{56}$$

n_f is the number density of the fission fragments,

$$\frac{\Delta \Omega(s)}{4\pi} = (1 - B(s)/B_c)^{1/2} \tag{57}$$

is the trapping fraction of the electrons that are emitted (isotropically) at s, and B_c is the field intensity at the local atmospheric cut-off altitude. The factor 6 in Eq. (56) accounts for the number of electrons per fission fragment that are emitted during the decay of gross fission fragments.

$$R(t) = \frac{0.2}{(1 + t)^{1.2}} \tag{58}$$

is the beta decay rate of the fission fragments in electrons/sec, normalized to one electron, i.e.,

$$\int_0^\infty R(t) \, dt = 1 \tag{59}$$

and

$$G(w, t) = \frac{e^{-w/w_0(t)}}{w_0(t)} \tag{60}$$

is taken to be the energy spectrum of the electrons in electrons/MeV. Here, the characteristic energy, $w_0(t)$, is a monotonically decreasing function of time. The spectrum is normalized to one electron, i.e.,

$$\int_0^\infty G(w, t) \, dw = 1 \tag{61}$$

The quantity $S_e RG/\Delta\phi$, therefore, gives the number of trapped electrons that are injected in the debris tube per second per MeV per unit azimuthal

35

angle. Multiplication by q and by $\dot{\phi}_D(w)$, the mean azimuthal drift velocity of electrons of energy w, gives the azimuthal drift current due to that increment of the electron source. The double integral, (55), sums the contributions to the current at t and $\varphi = \varphi_2$ of the electrons which are injected at $\varphi_1 \leq \varphi \leq \varphi_2$ at the earlier times $t - t'$, where

$$t' = \frac{\varphi_2 - \varphi}{\dot{\phi}_D(w)} \tag{62}$$

the upper limit of the t' integration is

$$T(w) = \begin{cases} t & , \ t \leq \dfrac{\Delta \varphi}{\dot{\phi}_D(w)} \\[3ex] \dfrac{\Delta \varphi}{\dot{\phi}_D(w)} & , \ t > \dfrac{\Delta \varphi}{\dot{\phi}_D(w)} \end{cases} \tag{63}$$

Since the electron energy ($\approx 2\%$ of fission yield) is much less than the hot-ion energy the drift current due to the electrons is much less than that of the hot ions. Hence, it need not be computed very accurately, and the following approximations seem justified,

$$S_e(t - t') = S_e(t) \tag{64}$$

$$w_o = <w_o(t)>_t \approx 1\,\text{MeV} \tag{65}$$

$$\text{and} \quad \dot{\phi}(w) = a\,w\,L = 2.44 \times 10^{-3} w\,L \tag{66}$$

In addition, by using Eq. (62) to change the variable of integration from t' to φ, Eq. (55) becomes,

$$I^e_D(t) = \frac{0.2\,q\,S_e(t)}{w_o\,\Delta\varphi} \int_o^\infty e^{-w/w_o}\,dw \int_{\varphi_L}^{\varphi_2} \left(t - \frac{\varphi_2 - \varphi}{\dot{\phi}_D(w)}\right)^{-1.2} d\varphi \tag{67}$$

36

where

$$\varphi_L = \begin{cases} \varphi_2 - \dot{\Phi}_D(w)\, t, & t \le \dfrac{\Delta \varphi}{\dot{\Phi}_D(w)} \\[4ex] \varphi_1 & , \quad t > \dfrac{\Delta \varphi}{\dot{\Phi}_D(w)} \end{cases} \qquad (68)$$

The φ integration gives,

$$\frac{1}{0.2}\left[\frac{1}{\left(1 + t - \dfrac{\varphi_2 - \varphi_L}{\dot{\Phi}_D(w)}\right)^{.2}} - \frac{1}{(1+t)^{.2}} \right]$$

Furthermore, since

$$\frac{\varphi_2 - \varphi_L}{\dot{\Phi}_D(w)} = t \quad \text{for } w \le w_1 = \frac{\Delta \varphi}{aLt} \qquad (69)$$

Eq. (67) may be written as,

$$I_D^e(t) = \frac{q\, S_e(t)}{w_0\, \Delta \varphi}\left\{ \int_0^{w_1} e^{-w/w_0}\left[1 - (1+t)^{-.2}\right]\dot{\Phi}_D(w)\, dw \;+ \right.$$

$$\left. \int_{w_1}^{\infty} e^{-w/w_0}\left[\left(1+t - \frac{\Delta \varphi}{\dot{\phi}_D(w)}\right)^{-.2} - (1+t)^{-.2}\right]\dot{\Phi}_D(w)\, dw \right\} \qquad (70)$$

$$\approx q\, S_e(t)\left\{ \frac{1}{\tau(L)}\left[1 - (1+t)^{-.2}\right]\cdot\left[1 - e^{-\frac{\tau(L)}{t}}\left(\frac{\tau(L)}{t} + 1\right)\right] \right.$$

$$\left. + R(t)\, e^{-\frac{\tau(L)}{t}} \right\} \qquad (71)$$

where $\tau(L) = \dfrac{\Delta \varphi}{\dot{\Phi}_D(w_0, L)}$ $\qquad (72)$

is the time for an electron of energy w_0 to drift across the debris tube.

37

3. DISTRIBUTION OF IONIZED DEBRIS

As mentioned in the introduction, the distribution of the debris and the accompanying energetic, ionized air in the vicinity of the magnetic bubble have been provided by NRL. Initially, however, this ion distribution included only the debris, and the codes that computed the subsequent distribution of the ions were based on the analyses described below in subsections a. and b. for the debris alone. The modifications of the codes to include the effects of the hot air are described in subsection c.

a. Initial Motion of Debris Along Magnetic Field

The Starfish debris data provided by NRL specify certain properties of the debris in reference planes perpendicular to $\bar{B}$ above and below the burst point. For each time step of 0.1 sec, $0 \leq t \geq 10$ sec, the data are given at various radial distances, r_i, from the central field line of the tube; the data are cylindrically symmetrical about this field line. The properties which are pertinent to the injection process are the mass flux, $d\dot{M}/da$, and the mean values of the velocities parallel and perpendicular to the field, v_{11} and $v_{\perp}$. Here $d\dot{M}/da$ is the debris mass in grams per second per cm^2 of the reference plane. The reference planes are 550 km above and below the burst.

The data do not include the fraction of the debris that escapes through the "neck" of the magnetic bubble at early times. In a private communication, Dr. R. Clark of NRL notified us that only about 1.5 percent of the debris escapes in this manner, and that it becomes distributed **over a radial distance** of about 10 km at the 550 km reference planes.

The data were received on magnetic tape, and were, therefore, easily processed for inclusion in the model. First, the data were averaged over 5 time steps (0.5 sec). This averaging was necessary because the data on the tape were quite noisy. Examples of the resulting mass flux that crosses the upper reference plane at various time intervals are shown in Figures 10 - 12. Here, the debris mass flux, integrated over the 0.5 second intervals shown in the

38
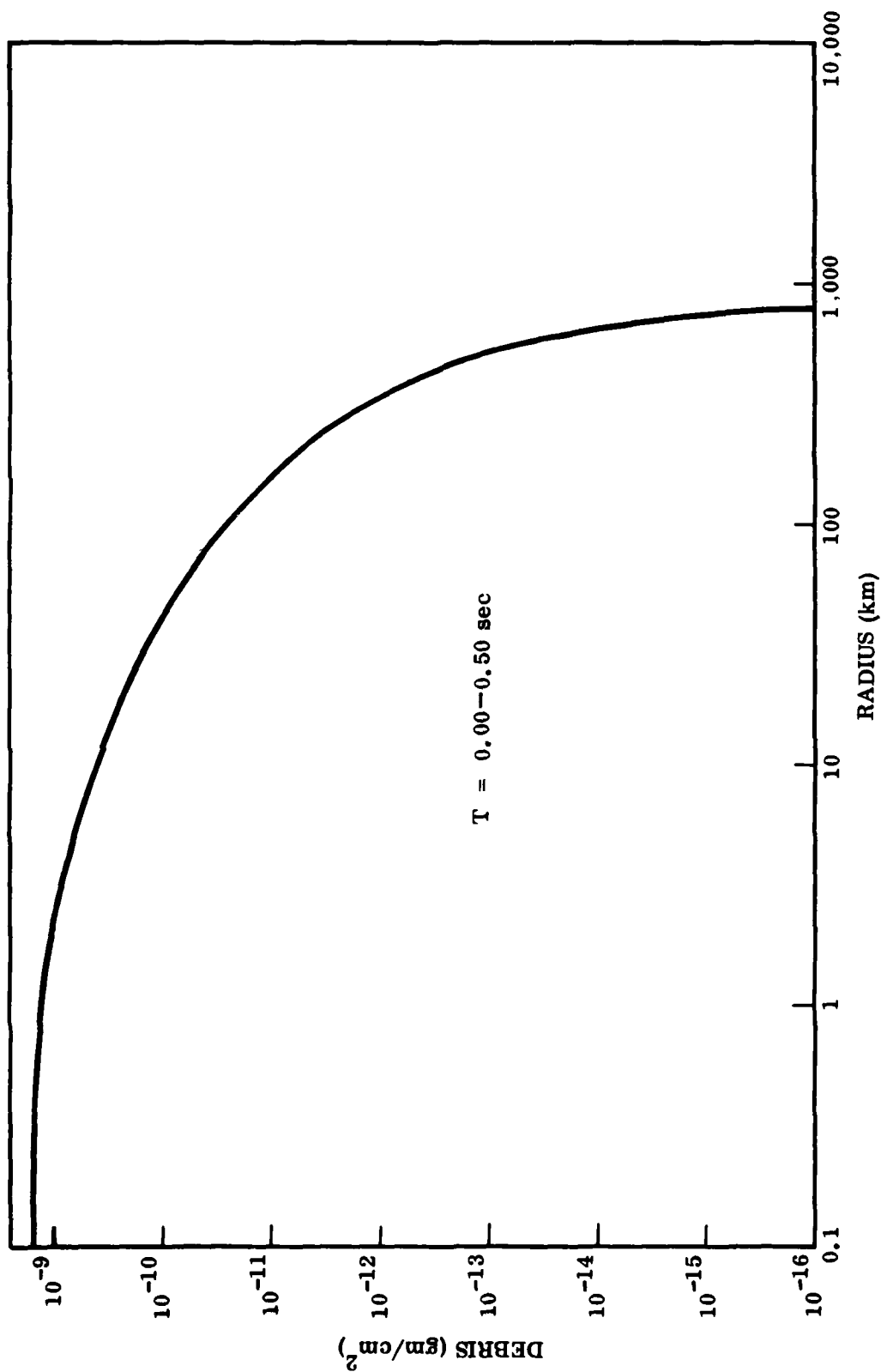
Figure 1C Integral of debris mass flux from 0 to 0.5 sec as function of radial distance in upper reference plane.

39
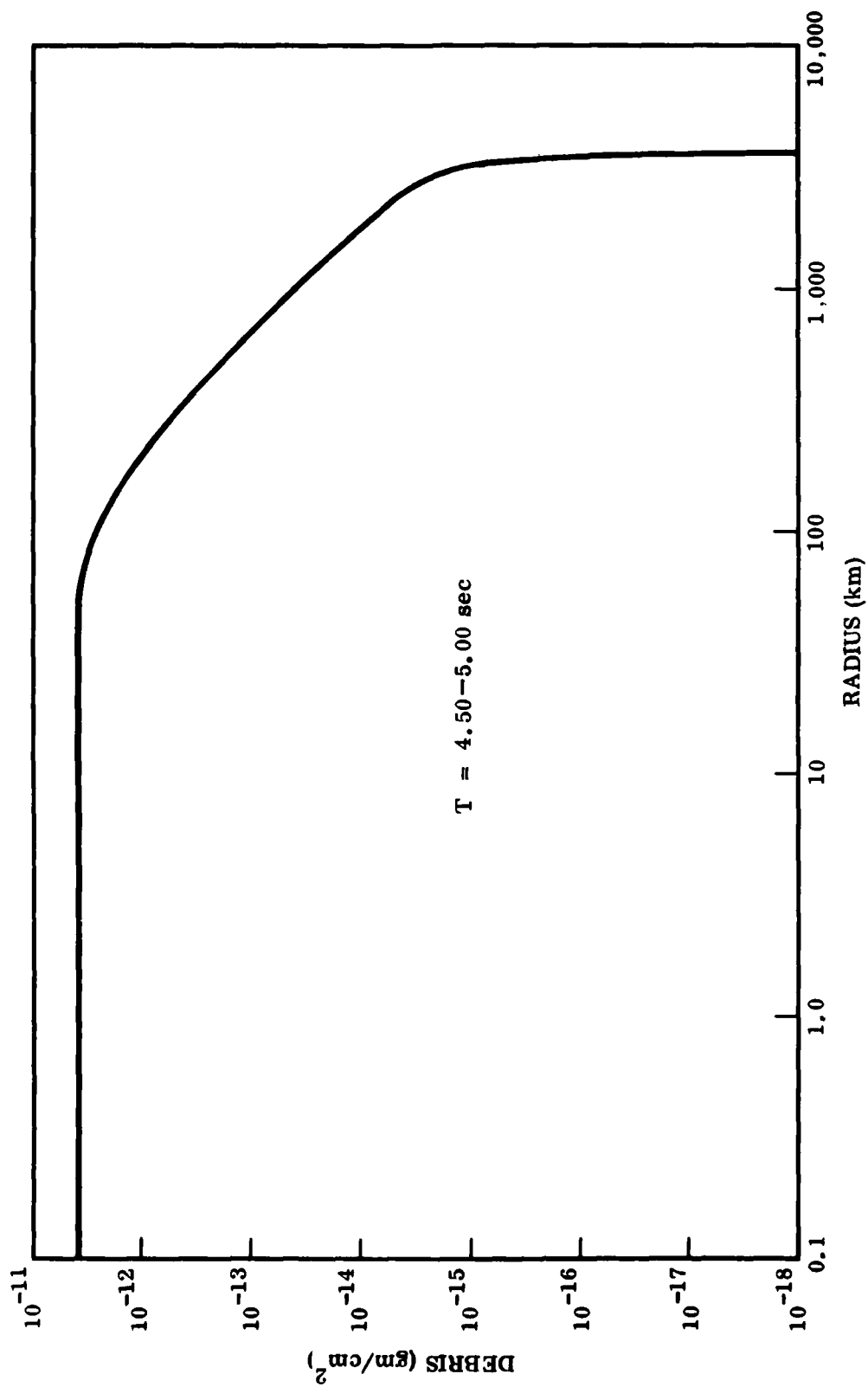
Figure 11 Integral of debris mass flux from 4.5 to 5 sec. as function of radial distance in upper reference plane.

40
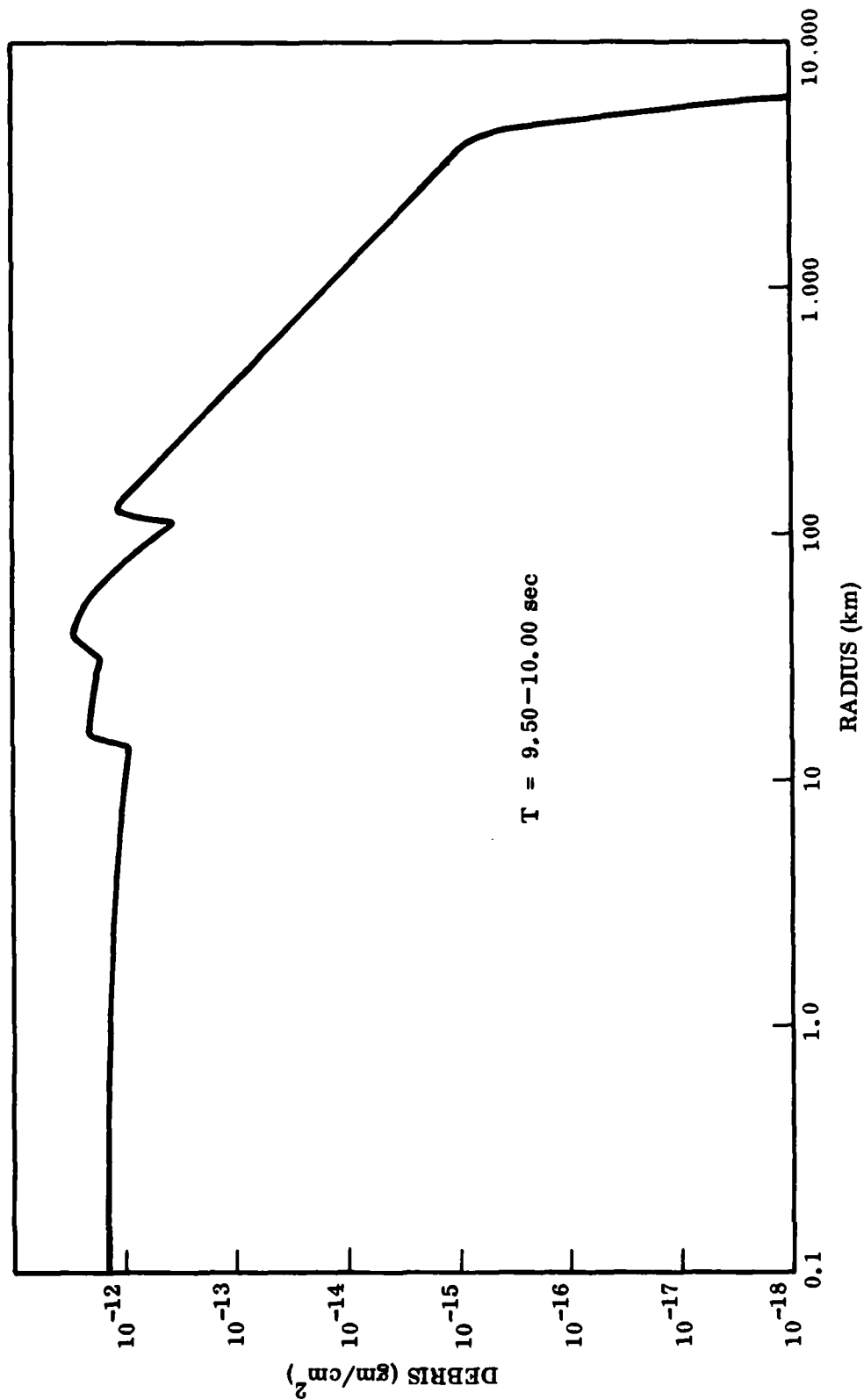
Figure 12 Integral of debris mass flux from 9.5 to 10 sec. as function of radial distance in upper reference plane.

41

figures, is plotted against the radial distance from the central field line in the reference plane. Note that at early times (0-0.5 sec) the flux is much higher near the central field line and it extends to smaller radial distances than at later times. The velocities of the debris do not vary more than by about a factor of five, either as a function of r at a given time or as a function of time at r = 0. Furthermore, the v_{11} components were greater than the $V_\perp$ components by more than an order of magnitude.

The data were then averaged to determine an effective width of the debris tube over which the mass flux and velocity were constant for each time step. Since the injection model utilizes a tube cross section that is square near the burst point, the distribution of the debris mass was first determined as a function of a rectangular coordinate x. This distribution was obtained from the integral,

$$\frac{dM(x,t_i)}{dx} \doteq 2 \int_0^{\sqrt{r_{max}^2 - x^2}} M_A(\sqrt{x^2+y^2}, t_i) \, dy \qquad (73)$$

Where $M_A(\sqrt{x^2+y^2}, t_i)$ is the mass per unit area crossing the reference plane at the distance $r = \sqrt{x^2+y^2}$ from the central field line in the interval 0.5 sec and at the time t_i. The quantity $\frac{dM(x,t_i)}{dx}$ dx is thus the debris mass that crosses one of the reference planes at x in the interval dx at the time t_i in the interval 0.5 sec.

The effective width, X^+, of the area in the reference plane above the burst and the width, X^-, of the area in the plane below the burst were then determined from the equation,

$$X^\pm = \frac{2 \sum_1 \Delta M_i^\pm \times (x_{hw}^\pm)_i + 0.0075 \, M_T^\pm \times 20 \text{ km}}{(1 + 0.0075) \, M_T^\pm} \qquad (74)$$

42

where the superscripts + and - refer to values in the upper and lower reference planes at the time $t_i \pm .25$ sec; $(x_{hw}^+)_i$ is the half-width at half-height of the distribution given by Eq. (73) for the same time interval; and M_T^+ is the total debris mass that traverses the upper reference plane. The mass is increased by .75% to account for the debris that escapes through the neck of the bubble. These quantities are given by the equations,

$$\left(\frac{dM^-(x, t_i)}{dx} \right)_{x = x_{hw}^+} = \frac{1}{2} \left(\frac{dM^-(x, t_i)}{dx} \right)_{x = 0} \qquad (75)$$

$$\Delta M_i^\pm = \int_0^{r_{max}} M_A^\pm (r, t_i) \, 2\pi \, r \, d \, r \qquad (76)$$

$$M_T^\pm = \sum_{i=1}^{20} \Delta M_i^\pm \qquad (77)$$

The effective area was then obtained from the equation,

$$A = [(x^+ + x^-)/2]^2. \qquad (78)$$

The mean value of the debris flux over this area at t_i is,

$$\langle F_i^\pm \rangle = \frac{2 \, \Delta M_i^\pm}{A \, m_{Al}} \qquad (79)$$

$\langle F_i^\pm \rangle$ is the number of debris particles per cm^2 per second. The mean mass of a debris particle has been taken to be the mass of an aluminum atom m_{Al}.

The mean value of the debris velocity at time t_i is given by the equation,

43
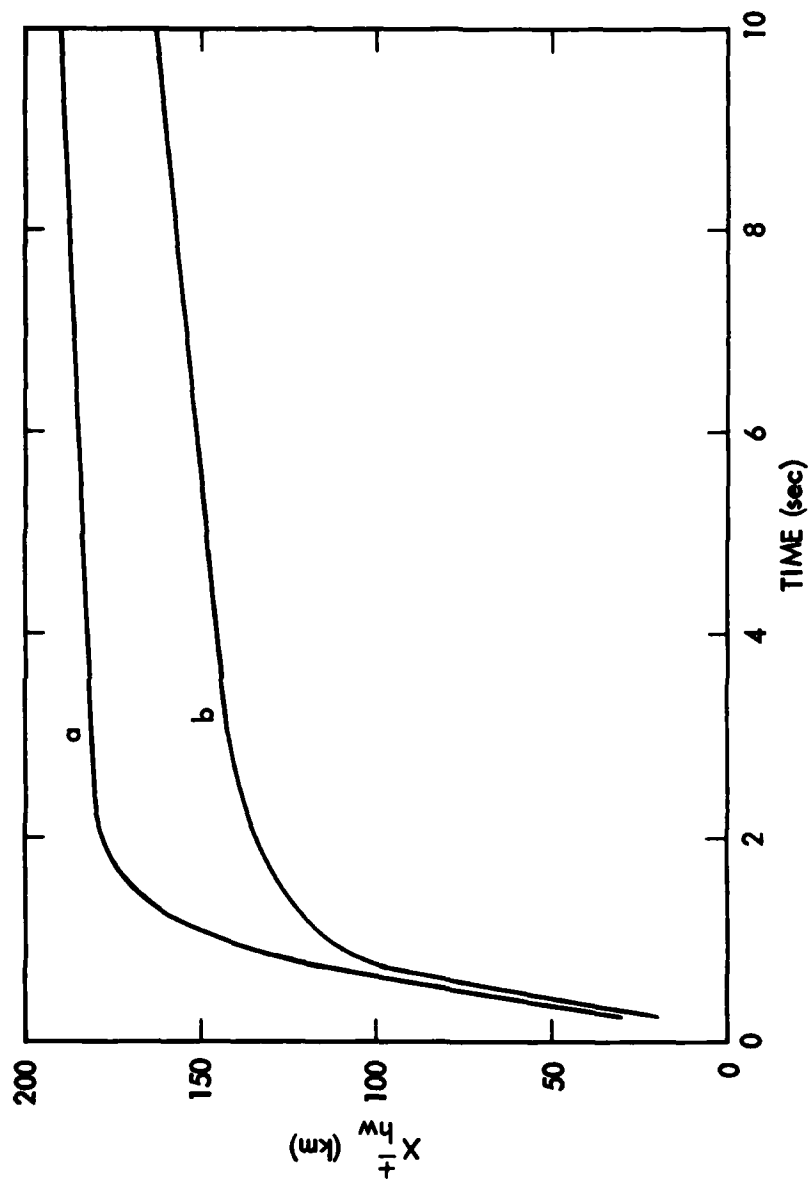
Figure 13. Half-width-at-half-height of mass flux distribution along rectangular coordinate as a function of time. Curves a and b refer to the distributions in the upper and lower reference planes respectively.

44
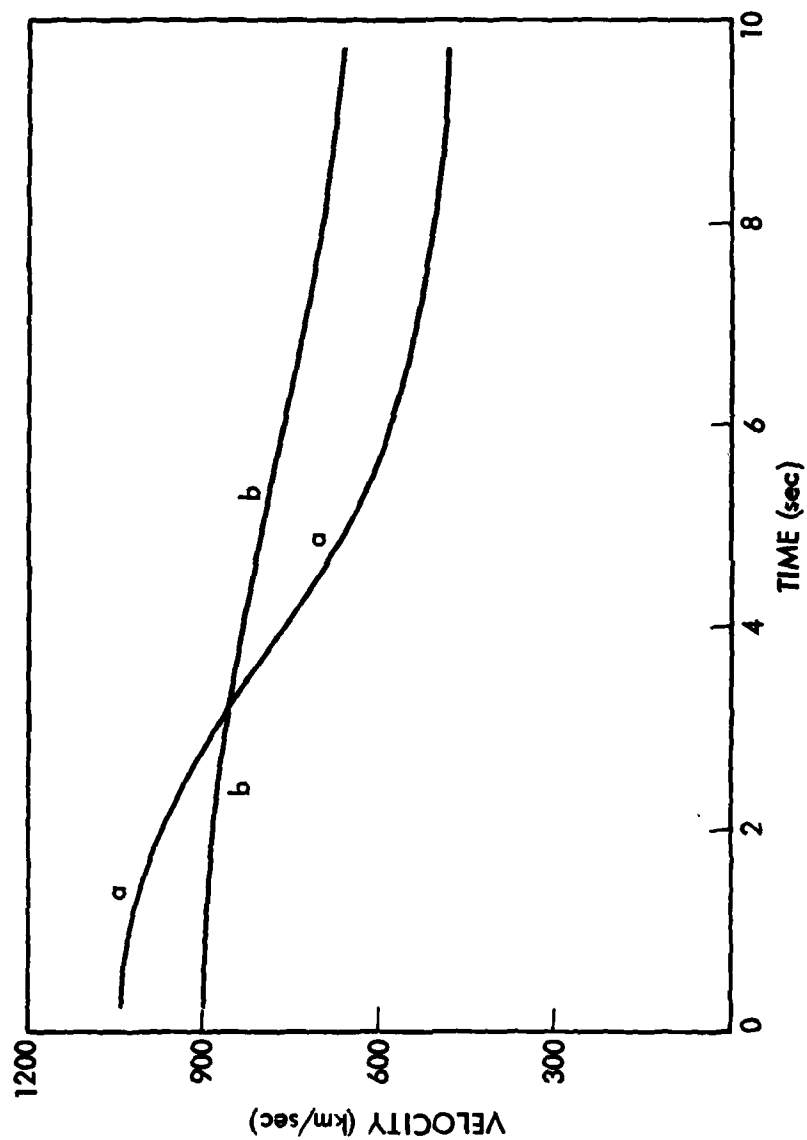
Figure 14. Mean parallel velocity component of debris in (a) upper reference plane and (b) lower reference plane as a function of time.

45

$$\langle v_i^{\pm} \rangle = \frac{\displaystyle\int_0^{r_{max}} v^{\pm}(r, t_1)\, M_A^{\pm}(r, t)\, 2\pi\, r\, d\, r}{\Delta M_i^{\pm}} \tag{80}$$

The half-width-at-half height of the mass flux distribution, $x_{hw}^{\pm}$, as a function of time is shown in Figure 13. The curve marked a in this figure gives the half width of the distribution in the upper reference plane, and curve b gives the half width of the distribution in the lower reference plane. The average values of the widths, weighted by the mass flux are 146 km for a and 109 km for b. The mean velocity components of the debris along the magnetic field at the upper and lower reference planes are shown in Figure 14 as a function of time.

The fission fragments are assumed to be uniformly mixed with the debris. Hence, the flux of fission fragments can be obtained by multiplying the debris flux by the fraction η, where:

$$\eta = \frac{N_{ff}}{N_D} \tag{81}$$

N_{ff} is the total number of fission fragments released by the burst (fission yield x 10^{26}), and N_D is the total number of debris particles $(M_T^{+} + M_T^{-})$ x $1.015/m_{Al}$.

b.   Distribution of Debris in Magnetosphere

The distribution of the debris in the magnetosphere is determined by combining the cross-L motion of the debris tube with the motion of the debris along the magnetic field. For this purpose, as well as for the computation of the capacitance of the tube, it is convenient to use the grid shown in Figure 15.
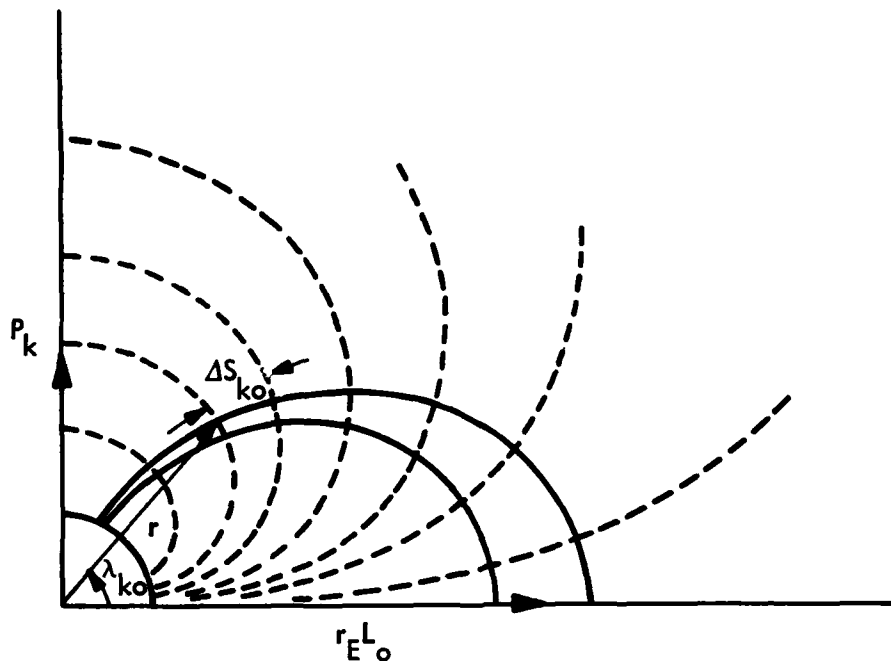
Figure 15. Illustration of partitioning of debris tube with surfaces normal to the magnetic field.

A family of curves,

$$r_k = p_k \sin^{1/2} \lambda_k \qquad (82)$$

orthogonal to the local dipole magnetic field lines are used to divide the debris tube into sections of length Δs_k. The initial sections are defined by a set of $N + 1$ latitudes $\{ \lambda_{ko} \}$ such that $\lambda_{ko} > \lambda_{k+1, o}$ with $\lambda_{k,o} = \cos^{-1} [(r_E + h_o)/L_o r_E]^{1/2}$ and $\lambda_{N+1,0} = 0$. Here, h_o is the limiting altitude due to the atmosphere. As the tube moves outward, the boundaries of the sections remain on the orthogonal curves, (82), which are defined by the N+1 set of polar intercepts $\{ p_k \}$. Since the curves pass through the predetermined set $\{ \lambda_{ko} \}$, the polar intercepts are given by the equations,

47

$$
p_k = \begin{cases} L_0 \cos^2 \lambda_{ko}/\sin^{1/2} \lambda_{ko}, & k \le N \\[3mm] 0, & k = N+1 \end{cases} \tag{83}
$$

A subroutine DPLATR has been written to compute λ_k given p_k and L.

First, an approximate value, λ_k^0, is computed using the equations:

$$
\lambda_k^0 = \begin{cases} 0 & , \ p_k = 0 \\[2mm] u_k(1 - .41\, u_k) & , \ u_k < 1.3 \\[2mm] [\log_{10} u_k]^{(u_k/(2.9\, u_k + 1.5))} & , \ i_1 < 75 \\[2mm] \pi/2 - [(1-.25/\sqrt{u_k})/\sqrt{u_k}]^{1/2} & , \ u_k \ge 75 \end{cases} \tag{84}
$$

where $u_k = (L/p_k)^2$.

The approximate value, λ_k^0, is then refined by using Newton's method with:

$$
\lambda_k^{i+1} = \lambda_k^i - f_i/(df/d\lambda_k)_i, \quad i = 0,1,... \tag{85}
$$

where $\qquad f_i = f(\lambda_k^i) = u_k \cos^4 \lambda_k^i - \sin \lambda_k^i$

and $\qquad \left(\dfrac{df}{d\lambda_k}\right)_i = -\cos \lambda_k^i\, (4u_k \cos^2 \lambda_k^i \sin \lambda_k^i + 1). \tag{86}$

The iteration sequence is stopped when $|(\Delta\lambda_k^{i+1})/\lambda_k^i| < \epsilon \doteq 10^{-6}$.

Knowing λ_k and L, other useful quantities along the tube can be computed, such as the magnetic field intensity at the center of a section which is needed to compute the tube capacitance and the electron trapping fraction. This field intensity, e.g., is given by the equation,

48

$$B_k \doteq \frac{B_E}{L^3} \cdot \frac{\left[1+3\sin^2\left(\frac{\lambda_k+\lambda_{k+1}}{2}\right)\right]^{1/2}}{\cos^6\left(\frac{\lambda_k+\lambda_{k+1}}{2}\right)} \tag{87}$$

The grid is specified in three separate regions: 1) the region below the lower reference plane, 2) the region between the reference planes, and 3) the region above the upper reference plane.

For each position of the tube, the number density of the debris along the tube in regions 1 and 3 is computed from the initial conditions of the debris in the reference planes. This computation is somewhat simplified because, as mentioned in the previous section, the velocities $v_\perp$ are negligible in comparison with $v_{||}$. Moreover, the specified values of $v_{||}$ are so high at the reference planes that $v_{||}$ can be regarded to be constant all along the tube. The near uniformity of $v_{||}$ can be verified with the equation that gives the variation of $v_{||}(s)$ along the tube; viz.,

$$v_{||}^2(s) = v_{||}^2(s') + v_\perp^2(s')\left(1-\frac{B(s)}{B(s')}\right) - 2gr_E^2\left(\frac{1}{r'} - \frac{1}{r}\right) \tag{88}$$

Here, the reference planes are located at s', $B(s)$ and $B(s')$ are the field intensities at s and s', g is the gravitational acceleration at the surface of the earth, and r and r' are the geocentric distances to s and s'. This equation reveals that a debris particle with the lowest specified velocity components will loose only a few percent of its initial $v_{||}$ component as it travels along the limiting field line of the trapping region, from near the surface of the earth to the equator. Accordingly, by using the equations for the continuity of the debris particles and the conservation of magnetic flux (BA = const.) along the tube, the mean value of the debris number density in the tube sections of regions 1 and 3 is given by the equations:

$$\langle r_D(s,t)\rangle_{\Delta s} = \frac{1}{2}\frac{B(s,t)}{B(s',t')}\left[\frac{F(s',t')}{v(t')} + \frac{F(s',t'+\Delta t')}{v(t'+\Delta t')}\right] \tag{89}$$

where F is the debris flux in particles/cm^2, and

$$\Delta t' = \frac{\Delta s}{\left(\frac{dv}{dt'}\right)_{t'} (t-t') - v(t')} \tag{90}$$

The latter equation follows from the definitions,

$$s(t) - s'(t') = v(t') (t-t') \tag{91}$$

and

$$s(t) + \Delta s(t) - s'(t') = v(t' + \Delta t') (t - t' - \Delta t') \tag{92}$$

In region 2, between the reference planes, the number density is,

$$< n_D(t) > = \frac{N_R(t)}{V(t)} \tag{93}$$

where $\qquad N_R(t) = N_{ff} - \sum_{+,-} \int_o^t F^{\pm} (t') A^{\pm} (t') dt' \tag{94}$

and $V(t)$ is the volume of the region at the time t. N_{ff} is the total number of fission fragments released by the burst, and the integrals in (94) give the number of fission fragments which have left the region at the time t through the upper and lower reference planes.

A subroutine, DEBATL, has been written to compute, for each time step of the tube motion, the distribution of the debris, as described above, and other quantities that are dependent on the debris distribution; namely, the tube capacitance due to the debris loading, the integral (42) for the computation of the drift current due to the debris, and the integral $S_e(t)$ for the computation of the drift current due to the trapped electrons.

50

c.   Code Modifications for Inclusion of Hot Ionized Air

The new data supplied by NRL include the hot ionized air that expands into the
debris tube at early times. The data that are now listed against time, t, and
radius, r, in the reference planes are:

   $Q_M(t, r)$, the mass flux (g/cm^2) of hot ions (debris and ionized air)
   integrated over the time step,

   $V_{11}(t, r)$, the velocity of the hot ions parallel to the magnetic field,

   $f(t, r)$, the ratio of the debris mass to the hot-ion mass, and

   $M(t)$, the mean mass (A.M.U.) of the ions averaged over the reference plane,
   at the time t.

The effective area of the debris tube and the values of ion velocity, $v(t)$,
and hot-ion flux, $F(t)$, averaged over the reference planes at the specified
times t, are computed as discussed in subsection a. above, except that
$Q_M(t, r)$ is used instead of $M_A(t, r)$ in equations (73), (76) and (80), and
the mean ion mass, $M(t)/(Avogadro's\ Number)$, is used instead of m_{A1} in equation
(79).   Examples of the results for Standard Spartan bursts at altitudes of
200, 300, 400 and 600 km, all at L=3, are shown in Figures 16 - 18.   The
input data were the same in the upper and lower reference planes; therefore,
the results apply for either plane. Figure 16 shows the sector width, $\Delta\phi$, of
the debris tube as a function of the altitude of the burst. The sector width,
of course, is determined from the square root of the effective area of the
debris tube at the burst altitude. In Figure 16 $\Delta\phi$ is plotted on semi-log
paper to emphasize the different scaling regime's. For bursts at altitudes
less than about 350 km, the results indicate that the lateral expansion of
the debris is limited by the atmospheric density (the slope of the straight
line is consistent with the scale height of the atmosphere in the range 200-
350 km). At altitudes above about 400 km the debris expansion is evidently
limited by the pressure of the magnetic field. The velocities of the hot ions
along the magnetic field as a function of time are shown in Figure 17. At
times less than about 0.6 sec, the ion velocities are about the same for all
of the burst altitudes. At such early times the ions consist principally of
debris particles alone. At later times, the velocities of the ions increase
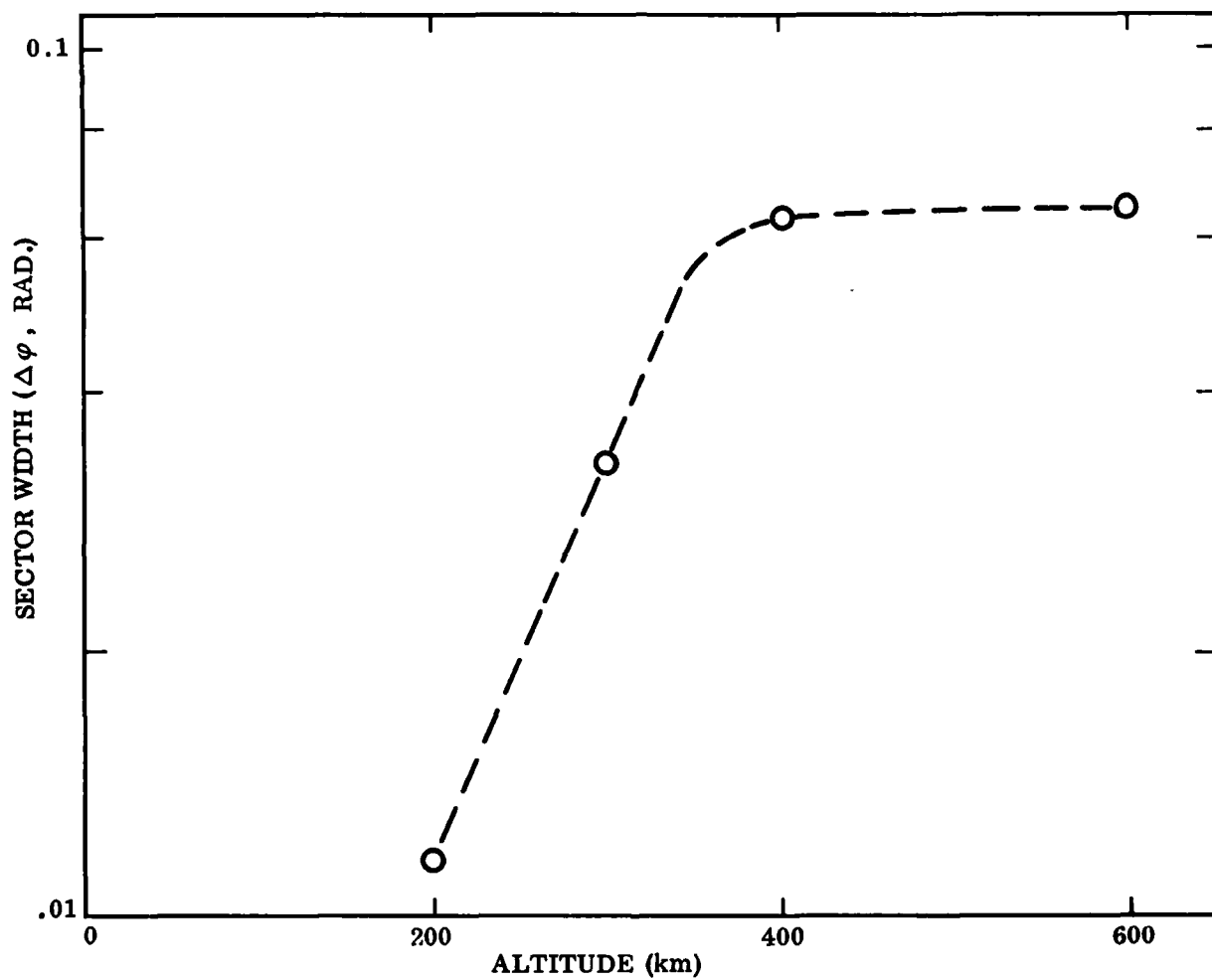
Figure 16. Sector width of Standard-Spartan debris tube as function of height of burst.

52
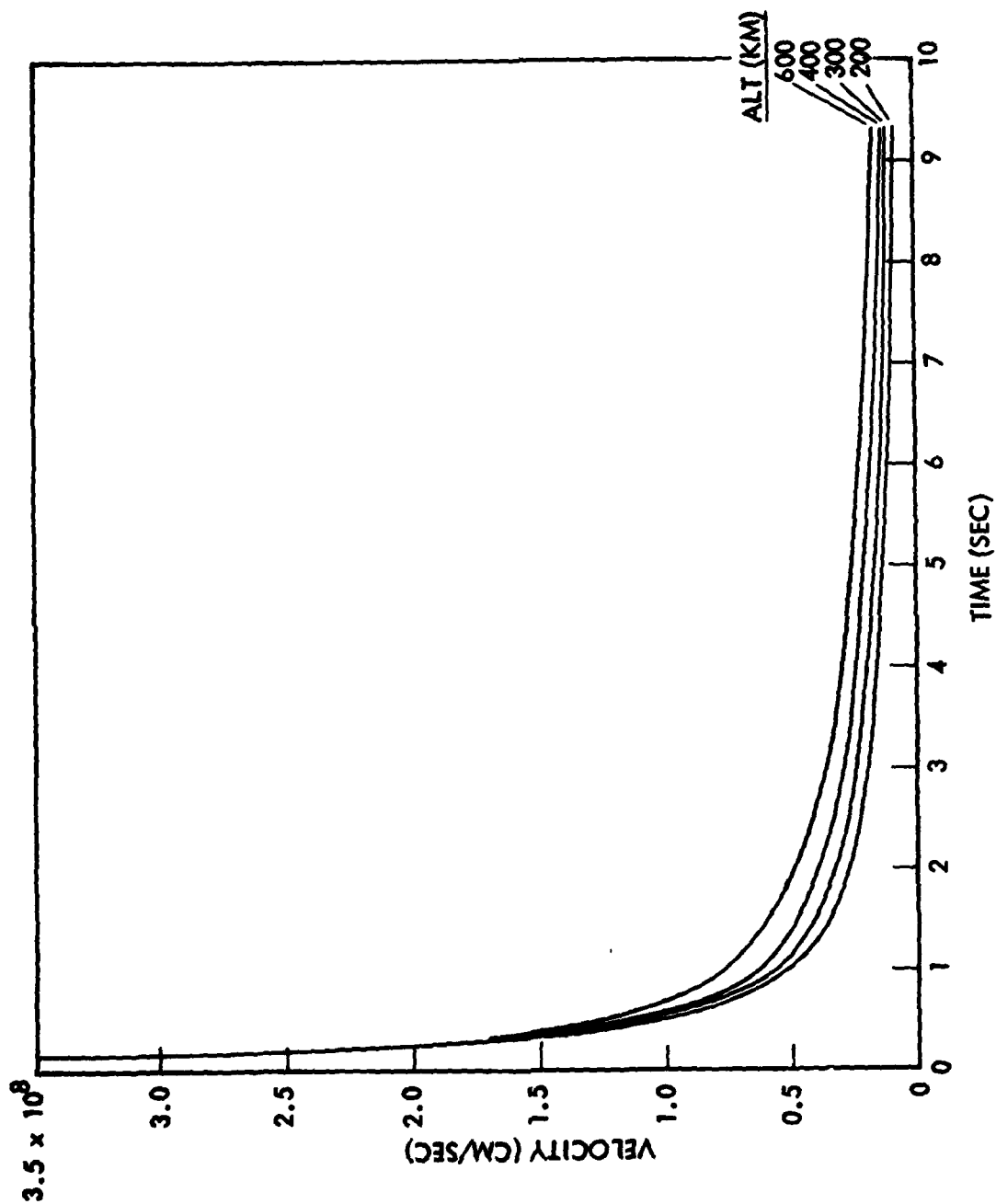
Figure 17. Velocity of ions along magnetic field in reference plane, versus time for Standard Spartan bursts at altitudes of 200, 300, 400, and 600 km (L = 3).

as the burst altitude increases. The ion fluxes as a function of time are shown in Figure 18. In this figure the ion flux for the 200-km burst is given directly by the ordinate. The flux for the other bursts is obtained by dividing the ordinate by the factors given in parentheses at the curves. At times beyond a few seconds, the ion flux consists mainly of air ions.

In the injection model, it is necessary to compute the number flux of fission fragments $F_{ff}(t)$ averaged over the reference plane at time t. This was done by computing, as a function of time, $n(t)$, the ratio of the number of fission fragments crossing the reference plane during the time-step interval to the corresponding number of hot ions. This is given by the equation,

$$n(t) = \left[\frac{Y_f \times 10^{26}}{M_T(\text{Debris})/M_{Al}} \right] \cdot < f(t) >_{R.P.} \cdot \frac{M(t)}{M_{Al}} \tag{95}$$

where Y_f is the fission yield in MT, $M_T(\text{Debris})$ is the total mass of the debris, and $< f(t) >_{R.P.}$ is the mass ratio $f(t, r)$ averaged over the reference plane; i.e.,

$$< f(t) >_{R.P.} = \frac{\int_0^\infty f(t)Q_M(t, r) \, 2\pi r dr}{\int_0^\infty Q_M(t, r) \, 2\pi r dr} \tag{96}$$

Note that the term in brackets in (95) is the total number of fission fragments divided by the total number of debris (this ratio is assumed to remain constant in any sample of debris). Recall that M_{Al}, the mass of aluminum, is the mean mass of the debris. This mass cancels in (95). The factor outside the bracket gives the ratio at time t of the number of debris ions crossing the reference plane during the time-step interval to the corresponding number of the hot ions. The sum of the numerator of (96) over the time steps gives $M_T(\text{Debris})$. The fission-fragment number flux is given by the equation,

$$F_{ff}(t) = \frac{n(t) \int_0^\infty Q_M(t, r) \, 2\pi r dr}{M(t) \, A_R \, \Delta t} \tag{97}$$

where A_R is the effective cross sectional area of the debris tube in the reference plane, and Δt is the time step. An example of the fission-fragment flux is shown in Figure 19, where $F_{ff}(t)$ and $F(t)$, for the Argus-3 burst, are plotted against time.
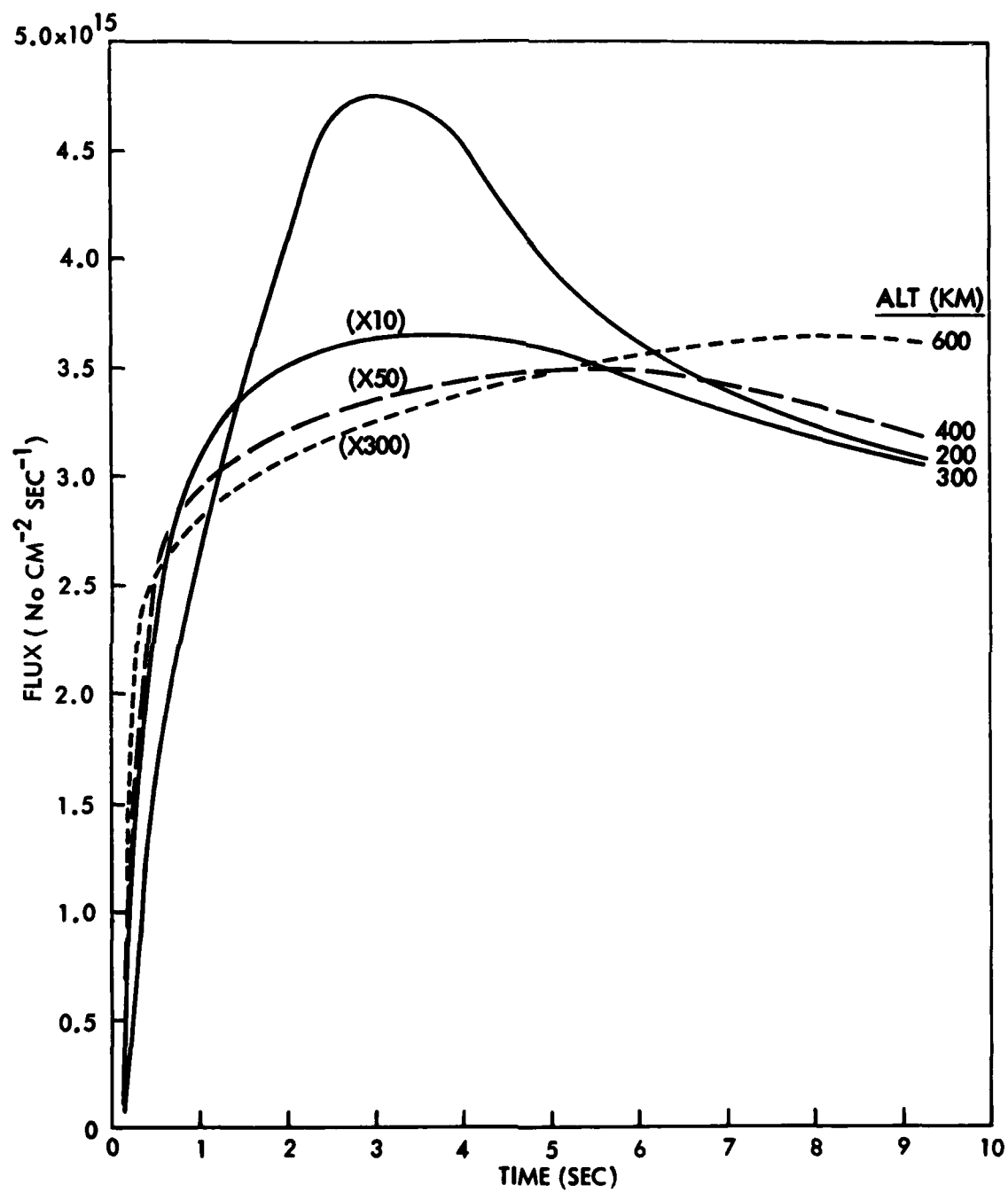
Figure 18. Hot-ions flux at reference planes vs. time for Standard-Spartan
bursts at altitudes of 200, 300, 400, and 600 km.

55
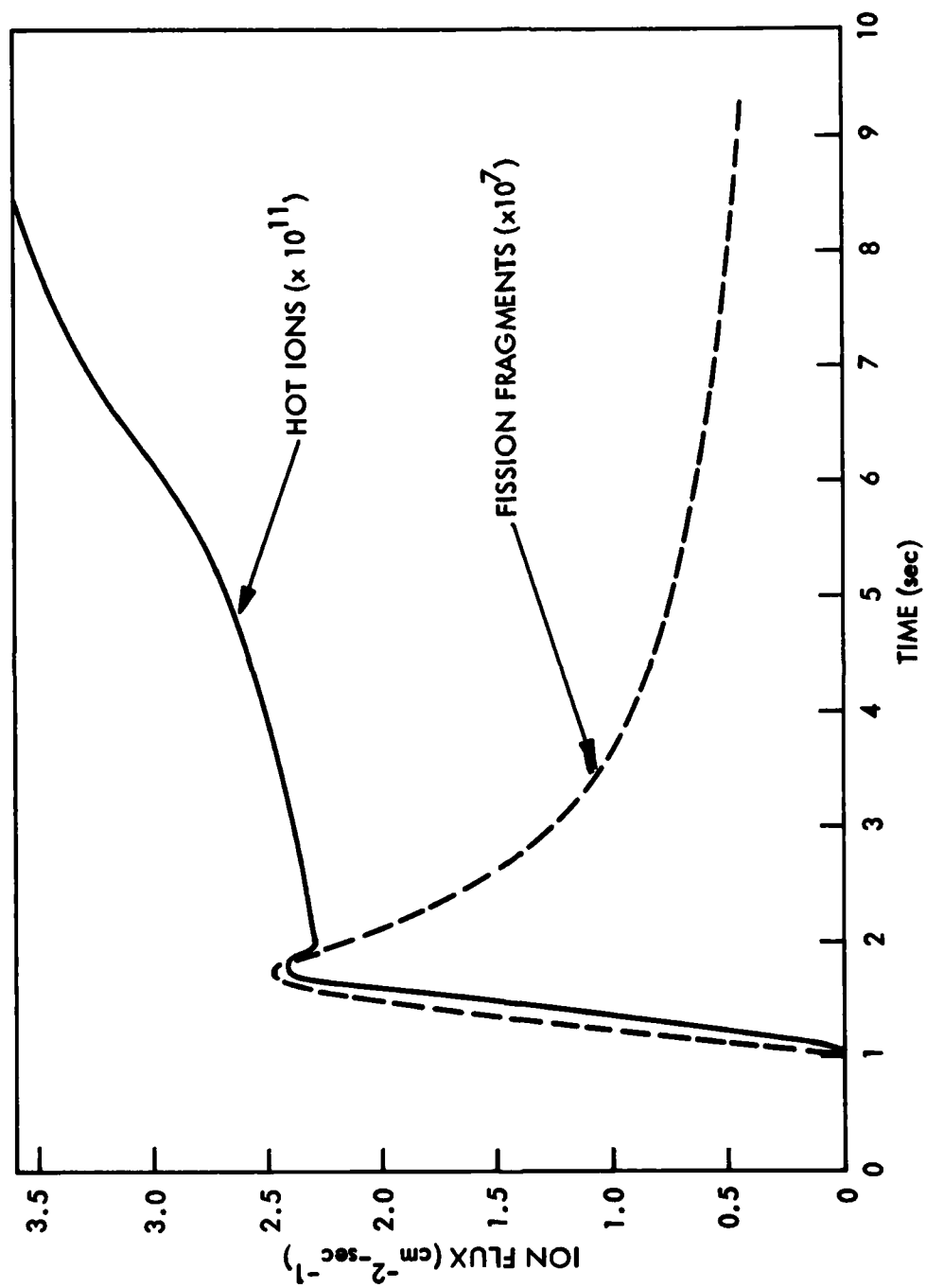
Figure 19. Fission-fragment flux and total hot-ion flux at reference planes vs. time for Argus-3 burst.

According to Dr. R. Clark of NRL, the accuracy of the data on the hot ions diminishes rapidly at times greater than a few seconds. This inaccuracy in the available data, as well as the incompleteness of the data (t< 10 sec), introduces an uncertainty in the tube motion. The sensitivity of the tube motion to different ion distributions has not been fully assessed. However, from limited tests that have been made with and without the hot-air ions, it appears that the error in the tube motion may not be severe.

The main program DEBCON and the subroutine DEBATL have also been modified to include the effect of the hot ionized air. DEBCON now allows input data that specifies $M_I(t)$ (the mean mass $M(t)$ in A.M.U.) and $\eta(t)$ which vary with time. Previously, when the NRL data included the debris alone, the mean mass was a constant, $M_I = 27$ A.M.U., and η was a constant.

As discussed in the previous section, the subroutine DEBATL computes the capacitance of the tube, the azimuthal drift current, and the integral of the number density of the fission fragments in the tube. The density of the hot plasma (debris and hot air) in the tube is required to compute the capacitance and the azimuthal drift current. The fission-fragment number density is computed from $F_{ff}(t)$ that is specified in the reference planes. The density of the hot plasma at a point along the tube is then computed from the number density of the fission fragments at that point by utilizing the values of $M_I(t)$ and $\eta(t)$ at the earlier time t when the fission fragments, moving the velocity $v_{11}(t)$, crossed the reference plane.

4. EARLY-TIME REDISTRIBUTION OF ELECTRONS

    a. Redistribution in Convecting Debris Tube

The redistribution of electrons in the debris tube is appreciable when the electrostatic potential V across the tube is high; i.e., when the tube is moving outward rapidly ($\dot{L}$ large). The situation is depicted in the sketch (Figure 20).

The electric field E in the tube causes the electrons to drift outward at the same rate as the tube. However, the energetic electrons also drift toward the east owing to the configuration of the magnetic field. Hence, in a stationary frame of reference, electrons that are injected at the western edge of the tube, ϕ_w, will follow a trajectory such as that shown by the broken-line curve in the sketch.

57
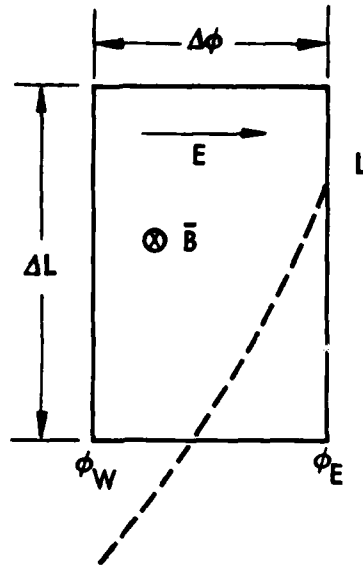
Figure 20 Illustration of displacement of electron in L due to outward drift motion of debris tube.

The trajectory is given by the differential equation,

$$\frac{dL}{\dot{L}} = \frac{d\phi}{\dot{\phi}_D} \tag{98}$$

where the dots indicate time derivatives; $\dot{\phi}_D = \dot{\phi}_D$ (w,L,μ_0) is the mean azimuthal drift velocity of an electron of kinetic energy w and equatorial pitch-angle cosine μ_0 at L.

The electron flux j at L,ϕ_E,t is related to the flux j' originating in the tube at L',ϕ',t', through Liouville's equation for relativistic electrons $(p^2 = w^2 + 2m_0c^2w)$. Hence,

$$\frac{j(L,w,\mu_0,\phi_E,t)}{w(w+2m_0c^2)} = \frac{j'(L',w',\mu_0',\phi',t')}{w'(w'+2m_0c^2)} \tag{99}$$

where m_0c^2 is the electron rest mass energy, the points L,ϕ_E and L',ϕ' are connected by the trajectory given by Equation (98),

58

$$w' = w + \frac{1}{\Delta\phi} \int_{\phi}^{\phi_E} \psi(t_\phi) \, d\phi \qquad (100)$$

ψ is the potential energy, qV, in the tube when the electron is at ϕ, i.e., at the time,

$$t_\phi = t - \int_{\phi}^{\phi_E} \frac{d\phi}{\dot{\phi}_D} \qquad (101)$$

and μ_o and μ_o' are related through the conservation of the first and second adiabatic invariants.

Now, since the fission fragments emit electrons continuously, the flux at L, ϕ_E, t is equal to the sum of the fluxes of the electrons which are emitted at ϕ_E at time t plus those which were emitted at earlier times along the trajectory shown in Figure 20 and drifted to ϕ_E, L at the time t. Thus, using (99), the flux may be written as,

$$j(L, w, \mu_0, \phi_E, t) = \int_{\phi_1}^{\phi_E} \frac{w(w+2m_0c^2)}{w_\phi(w_\phi+2m_0c^2)} \frac{dj_\phi}{d\phi} (L_\phi, w_\phi, \mu_{0_\phi}, \phi, t_\phi) \, d\phi \qquad (102)$$

where the subscript ϕ denotes source parameters, and the limit

$$\phi_1 = \text{Maximum of} \begin{cases} \phi_w \\ \phi \text{ at } t = 0 \\ \phi_c \text{ where } \mu_{0\phi} = \text{critical value} \end{cases} \qquad (103)$$

But, as discussed in our earlier work (Reference 1),

$$\frac{dj_\phi}{dt_\phi}(L_\phi, w_\phi, \mu_{o\phi}, \phi_\phi, t_\phi) = R(t_\phi)\frac{e^{-w/w_o}(t_\phi)}{w_o(t_\phi)} \int \frac{n(s_\phi)}{2\pi\mu_\phi t_b} \, ds_\phi \qquad (104)$$

59

where $R(t_\phi)$ is the emission rate at t_ϕ normalized to one, i.e.,

$$R(t_\phi) = \frac{0.2}{(1+t_\phi)^{1.2}} \tag{105}$$

$w_o(t_\phi)$ is the characteristic energy of the source spectrum at t_ϕ; $n(s_\phi)$ is 6 times the number density of the fission fragments at the point s_ϕ along the debris tube (6 is the number of electrons released per fission fragment); μ_ϕ is related to $\mu_{o\phi}$ through the conservation of the magnetic moment, viz.,

$$\mu_\phi{}^2 = 1 - \frac{B(s,\phi)}{B_o(L_\phi)} (1-\mu_{o\phi}^2) \tag{106}$$

where $B(s,\phi)$ and $B_o(L_\phi)$ are the magnetic field intensities at s and at the equator, respectively in the meridian ϕ, and $t_b = t_b(w_\phi, \mu_{o\phi}, L_\phi)$ is the electron bounce time. The integral is over the length of the debris tube between the mirror points

$$B_M(s,\phi) = \frac{B_o(L_\phi)}{1-\mu_{o\phi}^2} \tag{107}$$

By substituting (103) into (102) and noting that the source is uniform in ϕ, Equation (102) becomes,

$$\frac{dj}{dt}(L,w,\mu_o,t,\phi_E) = \frac{w(w+2m_oc^2)}{2\pi\Delta\phi}\int_{\phi_1}^{\phi_E}\int \frac{n(s,t_\phi)R(t_\phi)\mathrm{Exp}\left[-w_\phi/w_o(t_\phi)\right]dsd\phi}{w_\phi(w_\phi+2m_oc^2)\left[1-\frac{B(s,\phi)}{B_o(L_\phi)}(1-\mu_o{}^2)\right]^{\frac{1}{2}}t_bw_o(t_\phi)} \tag{108}$$

where $\Delta\phi = \phi_E-\phi_W$, and as indicated above, $t_\phi = t(\phi)$, $t(\phi_E) = t$, $w_\phi = w(\phi)$, $w(\phi_E) = w$, $L_\phi = L(\phi)$, $L(\phi_E) = L$.

Here, the mirror points of the electrons at the different ϕ values are determined from the following equation, which conserves the first two adiabatic invariants of the electron motion:

60

$$\frac{B_m(S,\phi)}{B_m(S,\phi_E)} = \left[\frac{L(\phi_E)}{L(\phi)}\right]^n \tag{109}$$

where $\quad n = 3 - \dfrac{1+.853950y-1.853950y^{3/4}}{1-.463488y^{3/4}} \tag{110}$

and $\quad y = (1-\mu_o^2)^{1/2} \tag{111}$

The flux given by Eq. (108), as well as integrations of the flux over time, equatorial pitch angle, and energy, are computed by the code DSTRIB and associated subroutines described in Section II.6. The integration of (108) over the total time required for the debris tube to traverse the field line at L, i.e., over the full time available for the electrons to drift out of the tube onto L, times the dilution factor $\Delta\phi/2\pi$ gives the equatorial directional flux $(cm^{-2} \cdot sec^{-1} \cdot sr^{-1} \cdot MeV)$ of the electrons after they become spread uniformly in longitude. The additional integrations over pitch-angle and energy give the equatorial omnidirectional flux with energies above certain prescribed minimum energies. Of course, knowing the directional flux at the equator, the directional and omnidirectional fluxes at any B value off the equator can be computed easily.

The flux obtained from the integration of (108) over time and pitch angle at various L values for the Starfish burst is shown in Figure 21. Note that the spectra of the electrons are quite hard at low L values — more so than the equilibrium fission beta-decay spectrum — and they rapidly become softer toward higher L values. At large L values the redistribution integral includes most or all of the debris tube azimuthal width. However, near the beginning of the debris-tube motion, at the lower L values, the drift velocities of the lower-energy electrons are so small that the effective width of the source is reduced $(\phi_1 > \phi_w)$. This effect accounts for the fall-off of the flux toward lower energies. The comparison of these spectra with the measured spectra of the Starfish electrons is discussed in Section III.

The flux at $\phi > \phi_E$ during the early-time expansion of the trapped electrons around the earth can be computed from the flux given by (108) at ϕ_E by using Liouville's theorem, as was done in Ref. 1. However, the computation is now somewhat more difficult because the energy spectrum of the redistributed electrons does not have the simple exponential form that was used previously to perform the pertinent energy integration analytically. A discussion of the computation of this "drift-diluted" flux is given below in Section II.4.

61
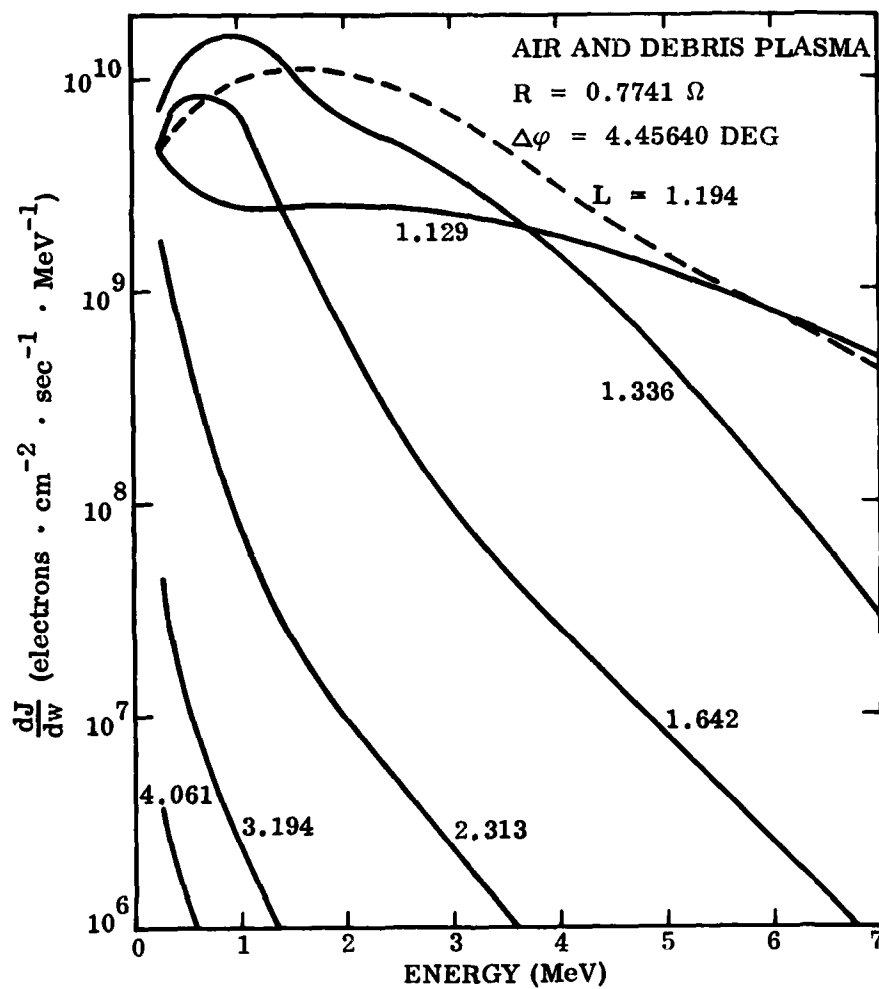
Figure 21. Energy spectra of redistributed Starfish-injected electrons at various L values.

b. Redistribution East of the Debris Tube

Even after the electrons drift out of the tube, they will continue to drift outward in L owing to an eastward electric field which exists in the region of the azimuthally-bunched electrons. This electric field develops because excess charge appears on field lines due to the azimuthal drift of the electrons that cannot be neutralized immediately. This charge can only be neutralized by currents that flow along the magnetic field lines containing the excess charge and across magnetic field lines in the ionosphere. Such neutralization cannot occur in times less than about the time, T_A, required for an Alfvén wave to traverse the length of a field line. The excess charge is roughly proportional to the rate of change of the number of trapped betas with respect to ϕ, $dN/d\phi$, times the product of T_A and the mean azimuthal drift rate of the electrons at ϕ. The charge is negative at the leading edge of the electron bunch and positive at the trailing edge. The excess charge is positive at the trailing edge because the betas drift away from the field lines on which their charges had been neutralized.

The analysis of the redistribution of the electrons due to this cause was carried out only until preliminary results indicated that it was not as large as that due to the convection of the debris tube. However, the process warrants further effort, especially since the Telstar satellite data indicate that the electrons injected by the high-yield tests were transported to higher L values than can be attributed to the convecting debris tube alone.

5. DEVELOPMENT OF THE DRIFT DILUTED FLUX

In the present injection model the electrons are presumed to be released when they reach the eastern edge of the debris tube. The source is therefore approximately a delta function in (magnetic) longitude coincident with the eastern edge. This is in contrast with the previous injection model where the source was spread out over the entire tube. The principal drawback in that model was that the source was assumed uniform in longitude, with no consideration given to how the electrons actually leave the tube. Now the motion of electrons within the tube can be predicted by the "redistribution" model. The motion after passing the eastern edge of the tube is entirely determined by uniform drift motion, in conjunction with the loss processes.

There are two principal methods for treating the drift dilution of a longitudinally nonuniform distribution of trapped electrons. The more straightforward method is to follow bunches of electrons with a finite energy spread. The longitudinal extent of a bunch then increases because of the energy dispersion of the angular drift velocity $\dot{\phi}_D$, thus

$$\Delta\phi \sim (T-t) \frac{d\dot{\phi}_D}{dw} w \tag{112}$$

where t is the injection time, T is the observation time, and w is the kinetic energy of the electrons. A distribution over the longitude segment, $\Delta\phi$ can then be assumed, and the contributions to the total distribution added up. The electrons may be assumed uniform over $\Delta\phi$; or, alternatively, a Gaussian distribution may be used to ensure a smooth distribution. This approach was rejected for the original Specter trapping model for two reasons. First, the simplest choices for the distribution over $\Delta\phi$ are quite non-physical, and could lead to serious errors if a bunch of electrons is followed for a complete circuit of the earth. The second objection is that following bunches of electrons for 1, 2, 3, 4, etc. circuits of the earth can lead to bookkeeping problems. Both problems can be minimized by reassembling the complete energy and longitude distribution at appropriate time intervals; but their implications remain very serious if a broad spectral range is to be treated properly.

The second approach, which was adopted for Specter, is to employ Liouville's theorem to follow the evolving distribution. Lieuville's theorem states that the phase space density remains constant throughout the drift motion. Thus a delta function distribution in energy, longitude, and time remains forever a delta function. The longitudinal spreading is accounted for by adding the contributions of an infinite number of delta functions. The distribution at any arbitrary time is then given by a single time integration over the source (Ref. 1). An apparent disadvantage is that the differential energy spectrum at early times may have a very irregular form. This leads to computational difficulties; but the irregularities are actually real — if they do not appear in treatments based on the alternate method, that is a consequence of artificial smoothing of the distribution. It is worthwhile to ask here whether the Liouville method can be altered or improved to remove the computational difficulties.

64

Consider a delta function (in time and longitude) source of injected electrons. At any longitude, electrons of a given energy will pass any point at regular intervals, corresponding to 1, 2, 3, etc. circuits of the earth. The instantaneous energy spectrum (see Figure 22) therefore consists of a series of delta functions, spaced at intervals

$$\Delta w = \frac{2\pi}{t} \frac{dw}{d\dot{\phi}_D} \tag{113}$$

The spacing decreases with time so that eventually the distribution appears to be uniformly filled, with nearly infinitesimal gaps. Obviously, if one wishes a smoothened representation of the spectrum, one must sample at intervals no closer than the spacing given by Eq. (113). Further smoothing is possible if it is recognized that any observation of a particle flux must take place over finite intervals of time and longitude. So a certain amount of time and longitude averaging — consistent with the duration of the observation — is appropriate, and in some cases, necessary.

The energy spectra of the redistributed electrons are nearly exponential and can be represented well by a sum of exponentials:

$$j\propto \quad C_o + C_1 \exp(-w/w_p) + C_2 \exp(-2w/w_o) + C_3 \exp(-3w/w_o) + \ldots \tag{114}$$

(This is simply a Taylor series in $\exp(-w/w_o)$.) Figure 23 demonstrates how well the computed spectra can be fitted by as few as 3 terms of the form $C_n \exp(-w/w_n)$, with w_1, w_2, and w_3 not commensurate. A fall-off at low energies is accounted for by a subtractive terms, $- C_n \exp(-w/w_n)$. A straightforward prescription for constructing the spectrum (114) is to select a w_o that gives the correct assymptotic behavior at large w. Then a least-squares method can be used to compute as many C_n's as desired; C_o is zero.

The contribution of the source at time t to the total flux of electrons above an energy w_1 is (Ref. 1)

$$\Delta j = \int_{w_1}^{\infty} \frac{dw}{w_o} \quad \sum_n C_n \sum_m \delta [\Phi - 2\pi m - \dot{\phi}_D (T-t)] \exp(-nw/w_o) \tag{115}$$

where δ is a Dirac delta function and m is the number of completed circuits of the earth.

65
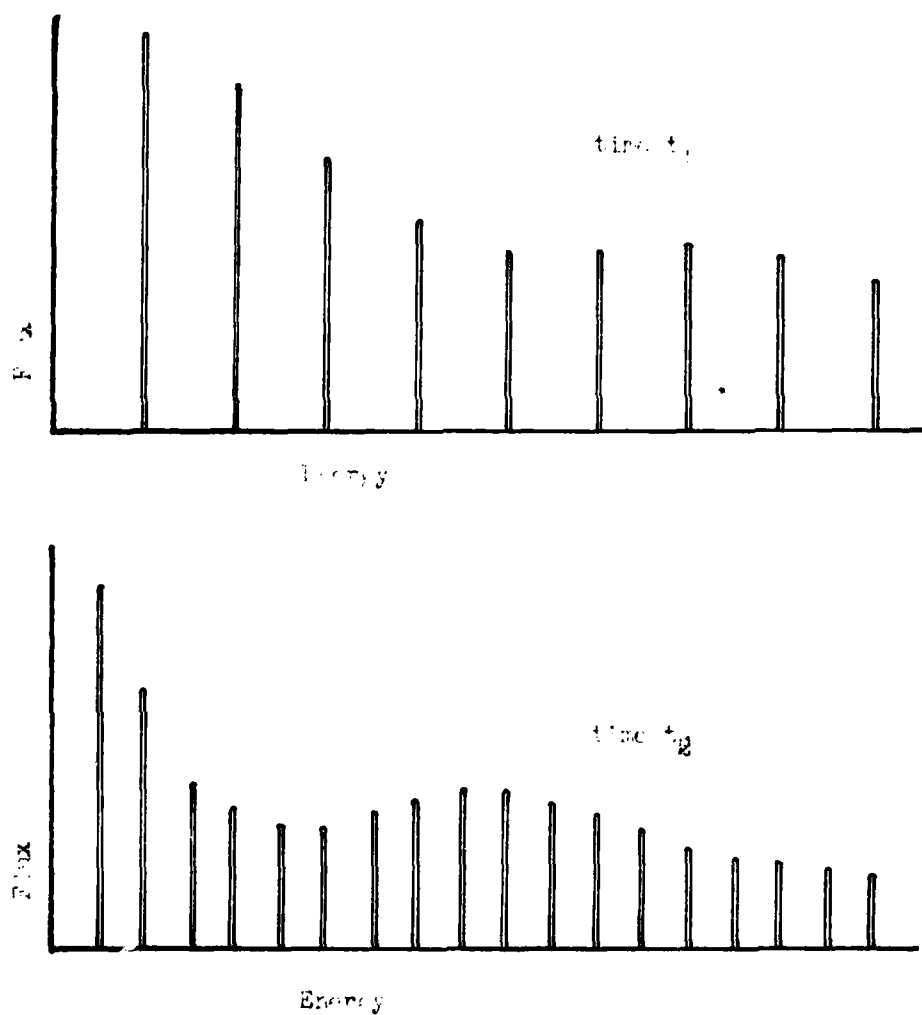
Figure 22. Energy spectra of drifting electrons at arbitrary
instants of time, t_1 and t_2 t_1. The source was
assumed very narrow in longitude.

66
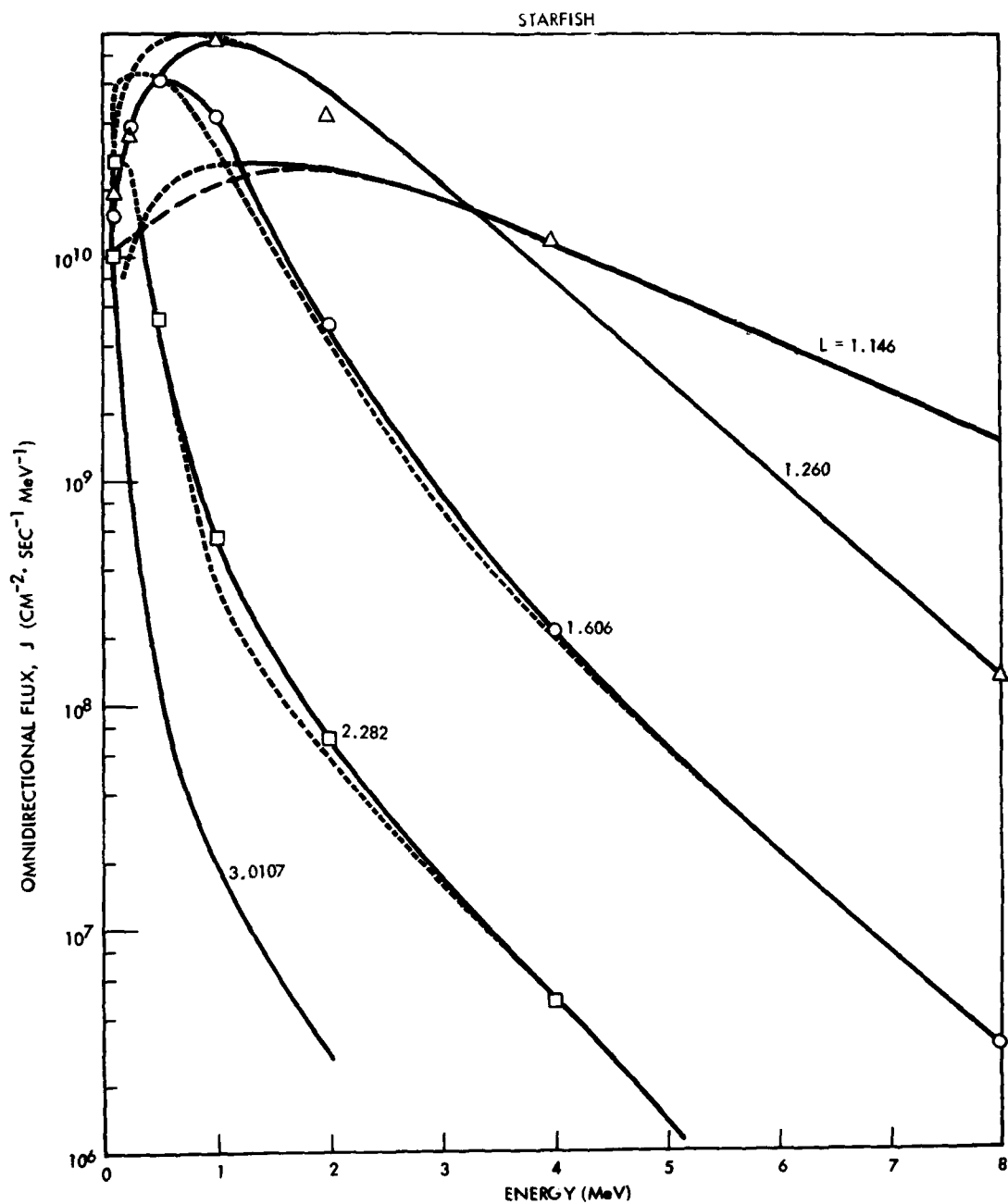
Figure 23. Energy spectra of the injected electrons at several
L-shells, as predicted by the new injection code.
The dashed curves are approximate representations by
sums of exponential functions.

67

The drift velocity is

$$\dot{\phi}_D = D_1 w \, \frac{w + 2 m_0 c^2}{w + m_0 c^2} \tag{116}$$

where D_1 is a function of L and pitch angle. To simplify the above integral, as in the treatment of Ref. 1, let

$$\dot{\phi}_D \approx DE \tag{117}$$

where the numerical value of D is somewhat different from D_1 and E is the total energy, $w + m_0 c^2$, of the electron. This approximation is valid at higher energies; at low energies, inclusion of the neglected factor leads to more complicated results. In the original model $\dot{\phi}_D$ was also assumed independent of pitch angle; this simplification has physical implications (in contrast to purely numerical approximations) but it is not really necessary. Integration of Eq. (115) now gives (Ref. 1), for a narrow source of width $\Delta\phi$:

$$j(E_1) \cong \int_0^T dt \; \Sigma_n K_n \, \frac{n\Delta\phi}{Dw_0(T-t)}$$

$$x \, \exp\{-n(\phi + 2\pi m_1)/Dw_0(T-t)\}/[1 - \exp\{-2\pi n/Dw_0(T-t)\}] \tag{118}$$

where m_1 is an integer

$$\frac{DE_1(T-t) - \phi}{2\pi} \leq m_1 < \frac{DE_1(T-t) - \phi}{2\pi} + 1 \tag{119}$$

The spectrum and source strength are included in the coefficients K_n.

In the existing Specter model the integration (118) is performed for each point E, ϕ, t in a grid, and is subsequently interpolated to obtain fluxes at intermediate points. This procedure has several disadvantages when one has to reconstruct the differential energy spectrum. The need for interpolations always introduces numerical errors. These errors are compounded when the differential spectrum at E is found by taking the difference

$$\frac{dj}{dE} \approx (j(E + \Delta E) - j(E))/\Delta E \tag{120}$$

Consider what happens as a pulse of electrons arrives at a point after completing an integral number of circuits of the earth. Figure 24 shows the peak
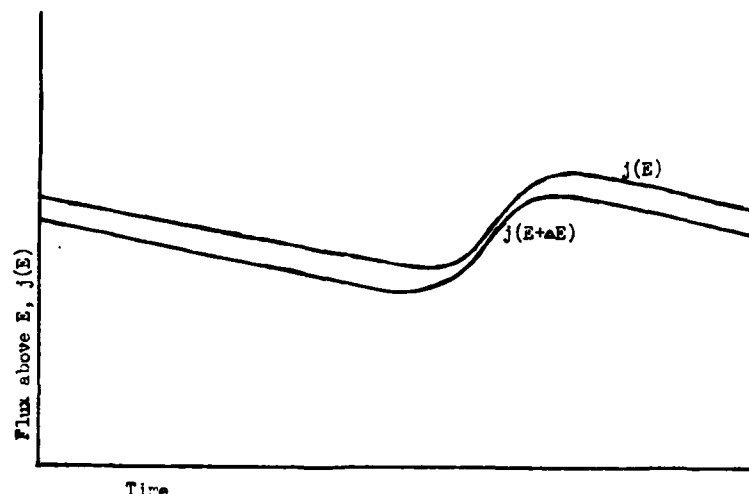
Figure 24. The variation of integral fluxes as a bunch of drifting electrons arrives at the observation point. The figure is exaggerated to emphasize how the difference between two integral fluxes changes with time.

of the pulse arriving later for the lower energy. Immediately before the pulse, however, there is a decrease in the differential flux as the two integral flux curves approach each other. It is easy to imagine situations where slight errors in the interpolation procedures could alter the relative positions of the integral flux curves, thereby accentuating the irregularities in the differential fluxes.

One way of dealing with spectral irregularities is to use relatively large energy intervals and average over time, as suggested above. However, a more elegant alternative is available that should completely eliminate the interpolation difficulties. That is to construct a formula that gives the fluxes as _algebraic functions_ of Φ, T, and E_1. Eq. (118) contains only one integration, and becomes algebraic for a source that is a delta function of time, t. The integration has been performed numerically by a finite differencing method. The source could be replaced by a series of delta functions at times t_1, t_2, t_3,...t_k, etc., with accuracies comparable to the present method. The physical consequences of this approximation are negligible if the spacing of the time points is sufficiently fine. The integral flux is then

$$j(E_1) \cong \sum_n \sum_k K_{n,k} \quad \frac{n\Delta\phi}{Dw_{ok}(T-t_k)}$$

$$x \ \exp\{-n(\phi+2\pi m_{1k})/Dw_{ok}(T-t_k)\}/[1-\exp\{-2\pi n/Dw_{ok}(T-t_k) \ ] \qquad (121)$$

$$\frac{DE_1(T-t_k)-\phi}{2} \leq m_1 < \frac{DE_1(T-t_k)-\phi}{2} +1 \qquad (122)$$

where w_{ok} is the value of w_o appropriate to t_k; and $K_{n,k}$ is the contribution to the n'th exponential at time t_k. The differential flux at E_1 is

$$\frac{\Delta j(E_1)}{\Delta E_1} \cong \sum_n \sum_k k_{n,k} \quad \frac{n\Delta\phi}{\Delta EDw_{ok}(T-t_k)} \ \exp\{-n(\phi+2\pi m_{1k})/Dw_{ok}(T-t_k)\}$$

$$x \ [\exp\{+ \pi n\Delta m/Dw_{ok}(T-t_k)\}-\exp\{-\pi n\Delta m/Dw_{ok}(T-t_k)\}]/[1-\exp\{-2\pi n/Dw_{ok}(T-t_k)\}] \qquad (123)$$

$$\Delta m = m_1(E_1+\Delta E/2)-m_1(E_1-\Delta E/2) \qquad (124)$$

The condition (113) on E arises naturally in the definition of m; if m_1 at $E_1+ E/w$ and at $E_1- E/w$ are identical, the differential flux is zero.

Eqs. (121) and (123) give accurate results, are easy to compute, and require minimal data storage. The source might be well represented by 20 to 50 t_k's and their associated w_{ok}'s. Each t_k might be associated with a spectrum that can be represented by 10 to 20 exponentails. Thus, at each pitch angle or mirror field, the flux could be adequately represented by a matrix of 200 to 1000 $K_{n,k}$'s.

6. DESCRIPTION OF COMPUTER CODES

The incorporation of the new tube motion debris model into the SPECTER codes
has resulted in the development of 3 new main programs AMBCAP, DEBCON and DSTRIB.
These main programs utilize some 21 new subprograms ACATL, ARANGD, BOUNCE,
BSFRMP, CONMAG, DEBATL, DPLATR, DTEQU, EXPINT, IONCON, LESSEN, LINTRP, MAGDEN,
MOVEL, PHIDOT, PLACE, PPLOC , SINMLT, SLATSQ, SLFS and TANDHI. Also, in order
to provide a basis for a necessary ionospheric model we have chosen to use
Chius 9 Fortran computer codes IONDEN, POLAR, PSI, SEMIAN, TVARFZ, TVEF1, W,
YONII and ZETA to compute the lower ionospheric density (Ref. 10). Some
modification to the old SPECTER code INJECT or SINJCT were also required.
Description of the 3 new main programs and the 21 new subprograms, together with
flow diagrams, are given below.

a. Program AMBCAP

Purpose:

This program computes the magnetic coordinates corresponding to the geographic
burst point, the ambient capacitance and the height integrated ionospheric
resistance along the field line passing through the burst point. The orthogonal
magnetic grid system used by this program and later by DEBCON to compute the
debris tube motion is also computed. See Figure 25.

Input:

HCOM	Labelling information for each case
NUSE	Default option index
ALT	Altitude of effective bomb center
DLAT	Geographic latitude of bomb center
DLONG	Geographic East Longitude of bomb center
TL	Local time in hours from midnight
DATE	Detonation day of the year

71

NIS	No. of integration steps
TEMP	Ionospheric temperature
BIGF	Instantaneous 10.7 cm solar flux
FBAR	10.7 cm solar flux averaged for one month
HM	Altitude of atmospheric cutoff
ELMAX	Maximum L value for L grids
RZUR	Smoothed Zurick sunspot number

Output:

Output from this program is to TAPE10.

RECORD-1   RE, BE, SQ3, ZMIN, NIS, NISMAX, MODE, DMLNG, EL, REQ, OHM, BDCK,
            CK(250,2), PK(250,2). See the AMBCAP code for definition of variables).

RECORD-2   F(100), 100 word array of useful Fortran variables (initial file A
            header information).

Externals:

ACATL, ATMOS, BLIMIT, CONMAG, DPLATR, DTEQU, EOF, HEDGE, INVAR, MAGDEN, SINMLT
and VALUE.

Method:

Subroutine INVAR is used to establish the burst point magnetic coordinates of B,
L and the magnetic latitude. Subroutine MAGDEN is used to compute the geo-
magnetic longitude. The ambient capacitance and the height-integrated ionospheric
resistance are computed as described in Section II.2b. The polar intercept array
that determine the orthogonal magnetic computational grid is computed by speci-
fying equal altitude intervals between the atmospheric cutoff and the equator
of the maximum chosen field line through which the orthogonal curves must pass
(See Figure 15).

AMBCAP

```
                START
                  │
    ┌─────────────────────────┐
    │        READ             │
    │        AND PRINT        │
    │        CARD INPUT       │
    └─────────────────────────┘
                  │
          YES   ◇────────◇
        ┌───────│  INPUT  │
        │       │  VALID  │
        │       ◇────────◇
        │            │ NO
        │      ┌───────────┐
        │      │   ERROR   │
        │      │   STOP    │
        │      └───────────┘
        │
        │
    ┌─────────────────────────┐
    │   COMPUTE J&C           │
    │   B* & L* VALUES        │
    │   AT BURST POINT        │
    └─────────────────────────┘
                  │
    ┌─────────────────────────┐
    │   COMPUTE DIPOLE        │
    │   λ*_m & φ*_m  VALUES   │
    │   AT BURST POINT        │
    └─────────────────────────┘
                  │
                 (1)
```

① COMPUTE DIPOLE POSITION AT FOOT OF FIELD LINE L*

COMPUTE R BY INTEGRATING UPWARD ALONG FOOT OF L*

COMPUTE ZMAX THE ALTITUDE AT $\lambda_m = 0$, $\phi_m = \phi^*_m$ AND $L = L_{max}$

WITH $\Delta Z \propto Z\,MAX$ COMPUTE POLAR INTERCEPTS AT EACH ALTITUDE FOR $L = L_{max}$

②

② INTEGRATE ALONG FIELD LINE L = L* TO COMPUTE C_A

OUTPUT RESULTS

COMPUTE VARIATION OF C_A WITH L VALUE

PRINT RESULTS

NORMAL STOP

Figure 25.   Program AMBCAP

73

b. Program DEBCON

Purpose:

This program reads in the AMBCAP values of ambient capacitance, ionospheric resistance, burst magnetic coordinates and the polar intercept array together with necessary card input values specifying the debris flux in order to compute the motion of the debris tube and the resulting debris density distribution along the flux tube. The debris distribution along the tube is determined from the motion of the tube, the given velocity and fission flux vs. time profiles at reference planes above and below the burst point and the fission and debris yield of the burst. See Figure 26.

Input:

TAPE10	See output of program AMBCAP
HCOM	Labelling information for each case
NUSE	Default option index
NT	No. of times where the fission debris velocity and flux are specified
YLD	Weapon yield in megatons
WF	Fraction of yield that is fission
RB	Radius of burst bubble
DSP	Initial distance of upper reference frame from the burst point
DSN	Initial distance of lower reference frame from the burst point
ETA	Time independent ratio of fission fragment to debris ions
AMI	Time independent mass per debris ion
TF	Maximum time the motion of the debris tube is computed
DT	Time increment used by the code to compute the tube motion
R	Ionospheric resistance (if other than AMBCAP value is to be used)
TD	The array of NT times where the fission debris distribution is specified
VIIP	The array of NT velocities parallel to the field line for the upper reference plane corresponding to the times in TD
FP	The array of fission fragment flux at the upper reference plane for the NT times in TD

VIIN   Same as VIIP but for lower reference plane

FN   Same as FP but for lower reference plane

ETAT   The array of the ratio of fission fragments to debris ions for each
        of the NT times in TD

AMIT   The mass per debris ion at the NT times in TD

NSBP   No. of computational time steps between print outs of the tube position

NDLG   No. of L values to output to file A

NTT   No. of times per L value to use 'in the file A output.

NTPI   No. of DEBATL print control times to read into array TPI

TPI   An array of DEBATL print control times where the odd values specify
        time print increments to use between the even values of TPI
        (TPI(0) = 0. is assumed)

Output:

Output of this program is to TAPE11 and TAPE18

TAPE11

RECORD-1   NIS   The no. of polar intercepts

                DPHI   The width of the flux tube

                PK   The array of polar intercepts

RECORD-2   EL   1st. L-shell value

                T   Time when the tube is at this L-shell

                EDEN   Array of fission debris density values at each of the
                        NIS points and each hemisphere for this L-shell

                .   .   .
                .   .   .
                .   .   .

RECORD-NDLG+1   EL   Last L-shell value

                T   Time when the tube is at this L-shell

                EDEN   Array of fission debris density values at each of the NIS
                        points and each hemisphere for this L-shell

TAPE18   File A (See output of DEBRIS code)

75
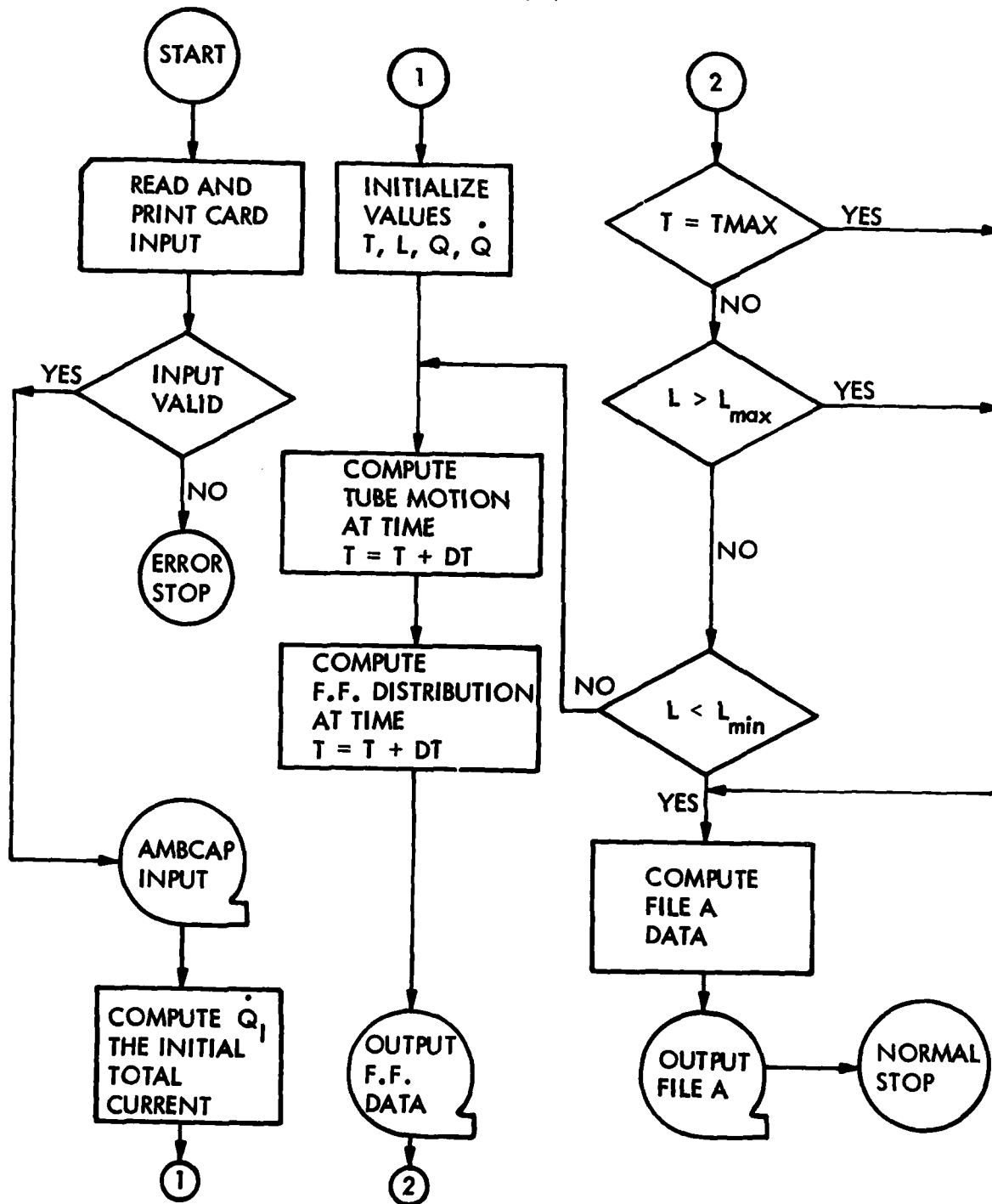
DEBCON

Figure 26. Program DEBCON.

76

Externals:
ACATL, ARANGD, DEBATL, DRIFTC, HEDGE, MOVEL, SINDEX and VALUE

Method:
This program computes the position of the flux tube and the fission-fragment distribution profile within the flux tube at discrete times. The tube motion is governed indirectly by the equivalent RLC circuit equation (Eq. 43). The height integrated ionospheric resistance is provided by AMBCAP or is defined via card input. Its value is assumed to remain constant.

At each time step an inline function routine FLF computes the inductance from Eq. (17), the ambient capacitance is computed by subroutine ACATL while the total capacitance and azimuthal drift current are computed by subroutine DBBATL which also updates the fission fragment distribution profile. The azimuthal drift current and RLC circuit values are used by subroutine MOVEL to solve the circuit equation and thus obtain the net charge across the tube. Thus, $\frac{dl}{dt}$ can then be computed from Eq. (42) and the new position of the flux tube evaluated. The above steps are repeated until the flux tube exceeds given L-shell bounds or until the time exceeds the maximum allowed.

c.   Program DSTRIB

Purpose:
This program computes the redistribution of injected electrons within the flux tube due to the generated electric field that moves the flux tube. The redistribution is computed for electrons at the eastern edge of the flux tube. The energy distribution of the redistributed electrons at the equator is also computed. This is necessary since these electrons will in general no longer have the simple fission beta energy spectrum. This complication in the spectrum is due to the fact that electrons with different energy do not drift to the east at the same rates.

77

<u>Input:</u>

TAPE11   See output of program DEBCON

DTMAX   Maximum time step increment allowed

DU   The cosine (pitch angle) increment to use for the pitch angle grid.

FK   The number of longitude intervals to use within the flux tube.

NEM   The number of discrete energy values where the electron distribution
            is to be computed.

EG   The array of NEM energy values

T   The time when the redistribution is to be computed (the time T
            specified the L-shell position of the flux tube)

PHIED   The east longitude of the eastern edge of the debris tube.

<u>Output:</u>

At present there is no output tape from this program. However, the printed
output provides details of the energy and pitch angle distribution of the
redistributed electrons.

<u>Externals:</u>

BLIMIT, BOUNCE, BSFRMP, EXPINT, LESSEN, LINTRP, PHIDOT, SINDEX, SLATSQ, VALUE
and YINOX.

<u>Method:</u>

The method used by this program is described in Section II.3a. The use of
Liouville's equation together with conservation of the first and second adiabatic
invariants, conservation of magnetic moment, and a uniform source in longitude
result in Eq. 108 that relates the time derivative of the directional flux
$\frac{dj}{dt}$ to a double integral over the fission fragment source function along the
appropriate field line at each possible longitude within the flux tube.

This flux $\frac{dj}{dt}$ gives the number of electrons per square cm per sec. per sec.
per steriadian per MeV at the eastern edge of the flux tube. This equantity
can be integrated over time within the flux tube and over pitch angle to obtain

78

the desired energy distribution at the equator. A further integration over
energy results in an omnidirectional flux that when divided by $2\pi/\Delta\phi$
can be compared with the equatorial longitude independent flux that is computed
by other SPECTER codes.

d. Subroutine ACATL

Purpose:
This subroutine computes for a given L-shell the ambient capacitance of the flux
tube (assuming the frozen-field model) the distance to the magnetic equator
from the earth's center, the distance to the equator along the field line from
the point of intersection of the orthogonal curve defined by each polar intercept
and the magnetic field intensity corresponding to these intersections.

Input:

ARG   Task option, set to zero if ambient capacitance and distance to equator
            REQ are not required

ACATLC   Labeled COMMON variables   RE, ZMIN, KM, MODE, DMLONG, EL, BDCK,
            CK and PK (See ACATL code for definitions of variables)

Output:

AC   Ambient capacitance of the flux tube at the L-shell EL in farads
REQ   Distance in earth radii from the center of the earth to the magnetic
            equator
SK   An array of distances in KM along the field line EL to the equator
            from the intersection points defined by the polar intercepts in PK
            for each hemisphere.
BK   An array of magnetic field intensities in gauss along the field line
            EL at the intersection points defined by the polar intercepts in PK
            for each hemisphere
FLATK   An array of magnetic latitude parameters equal to $(1 + 3 \sin^2\lambda)^{\frac{1}{2}}$
            where λ is of the magnetic latitude at each intersection point defined
            by the values of polar intercepts in PK for each hemisphere.

79

Externals:

BLIMIT, CONMAG, DPLATR and DTEQU

Method:

Subroutine BLIMIT is called to define the equatorial value of magnetic intensity B_o at the input L-shell. For each polar intercept, subroutine DPLATR is then called to compute the magnetic latitude that defines the magnetic field intensity since

$$B = B_o \ (1 + 3 \ \sin^2 \lambda \ )^{\frac{1}{2}}/\cos^6 \lambda \ . \tag{123}$$

The function subroutine DTEQU is called to compute, as a function of the distance along the field line, a quantity used later by BEBATL to determine the debris distribution. Subroutined CONMAG is called with the magnetic latitude and input longitude as arguments in order to compute the geographic altitude of the intersection points that define the flux tube segments. The contribution to the ambient capacitance from each flux tube segment k is then computed from the equation

$$C_k = C_{ko} \ (Y_k + Y_{k-1})/(B_k + B_{k-1}), \tag{124}$$

where

$$C_{ko} = \rho_{ko} \ \Delta S_{ko}/B_{ko}, \quad Y_k = (1 + 3 \ \sin^2 \lambda_k)^{\frac{1}{2}}$$

and the o subscript refers to the initial position of the flux tube where the mean ionospheric density in the segment was ρ_{ko} and the segment length was ΔS_{ko}. The above equation is used provided the altitude of the segment is above the atmospheric cutoff. An interpolation is made if the tube segment lies partly above and below the atmospheric cutoff. The total ambient capacitance is obtained by summing over each C_k. The distance to the equator from the earth's center is computed from the last altitude computed (corresponding to λ=o).

e.   Subroutine ARANGD

Purpose:

Subroutine ARANGD reads in and arranges a subset of the computed debris
distribution data on TAPE11 into the format specified by file A and writes the
arranged data on TAPE18. This data can then be processed by the SEPCTER
injection and flux codes. Only a subset of the DEBATL generated data is written
to TAPE11, however, this data in general is specified for many more points along
a field line than is practical for output as file A and must be reduced. Also,
since the tube motion may be sinusoidal in L, data on TAPE11 from various time
segments must in general be combined in order to specify the debris at any given
L-shell as a function of time as is required by the file A format.

Input:

NLG	The number of L values in array ELG where the fission debris density is to be evaluated
ELG	The array of monotonic increasing L-shell values that covers the range of tube motion. The debris is to be spedified at these L values
NLT	The number of L values in array ELTBL and the number of field line debris distribution density profiles written to TAPE11
ELTBL	The array of L values where the debris distribution density profiles are contained on TAPE11. These L values are separated by a constant time increment.
TI	The initial time relative to the burst when data is first written to TAPE11 (TI = 0).
TF	The last time when data is written
DT	The time increment in seconds between the stored data on TAPE11
CDEL	The ratio at the equator of the height of the debris tube to the distance to the equator from the earth's center
NT	The number of times when the field line debris density profiles are to be computed for each L value
ITL	The input tape number (11)
ITD	The output tape number for file A (18)

Output:

ARANDG writes data on TAPE18 according to the format described below:

Record No.	Description
2	A monotonic increasing array of L values for which the density is specified.
3	An array that specifies the number of points used along each L shell.

4	An array specifying distance to the equator in km for each point.
5	An array specifying magnetic intensity in gauss for each point.
6	An array specifying the corresponding equatorial cosine (pitch andle) for each point.

....

7	An array specifying the time for each point at which the debris number density is given in the following record.
8	An array specifying the debris number density for each point corresponding to the times specified in the previous record.

....

The records between the dashed lines are repeated for every L value contained in record 2 and the records between the dotted lines are repeated for as many times as is adequate to represent the desired debris distribution.

Method:

At the present time ARANGD handles as many as six entries of the debris tube into a particular L interval. Entrance and exit times, t_{in} and t_{out}, are computed for the times when the center lines of the debris tube cross the L values, L_{min} and L_{max}, which are separated approximately by the tube width L. The L limits are given by the equations,

$$L_{min} + \frac{L_{min}}{2} = L \qquad (125)$$

$$L_{max} - \frac{L_{max}}{2} = L \qquad (126)$$

where L is the location of the tube. Since the tube width, L, is proportional to L^2, the above equations can be solved to give,

$$L_{min} = [-1 + (1 + 2 \Delta L/L)^{\frac{1}{2}}] L^2/L \qquad (127)$$

$$L_{max} = [1 - (1 - 2 \Delta L/L)^{\frac{1}{2}}] L^2/L \qquad (128)$$

$$\Delta L = (L/L_o)^2 \Delta L_o \qquad (129)$$

and $$\Delta L_o = L_o \Delta\phi \qquad (130)$$

The debris density for the specified L values can then be computed by interpolation at the times $t_{in} \le t \le t_{out}$ from the previously-computed debris distribution data on input TAPE11.

f. Function BOUNCE

Purpose:

This routine computes the electron bounce period as a function of energy, pitch angle and L-shell.

Input:

EL   The L-shell
EMEV   The energy in meV.
S   The value 1 sine (pitch angle)

Output:

BOUNCE   The electron bounce period in seconds

Method:

The bounce period T is computed from the equation

$$T = f(L)*g(E)E*h(S) \qquad (131)$$

where

$$f(L) = .084949L \qquad (132)$$

$$g(E) \;=\; (1 + E/E_0)/[(1 + E/E_0)^2 - 1]^{\frac{1}{2}}, \tag{133}$$

$$h(S) \;=\; 1.380173 - 0.639693S^{0.74}, \tag{134}$$

$E_0 = .51098$, $L = EL$, $E = EMEV$ and $T = BOUNCE$

The routine attempts to economize by not recomputing $f(L)$, $g(E)$ or $h(S)$ if the corresponding input values do not change.

g. Subroutine BSFRMP

Purpose:

This routine computes for a given field line an array of magnetic intensities and distances along the field line to the equator corresponding to the intersection points defined by an input array of polar intercepts.

Input:

EL	The magnetic L-shell or field line
KM	The number of polar intercepts or intersection points
KMAX	The 1st. dimension of arrays PK, BK and SK
PK	The array of polar intercepts in earth radii for each hemisphere

Output:

BK	The array of magnetic intensities in gauss for each hemisphere
SK	The array of distances along the field line to the equator for each hemisphere. Distances are negative in the southern hemisphere.

Externals:

BLIMIT, DPLATR and DTEQU

Method:

The equatorial magnetic intensity B_0 at L-shell L is computed by calling subroutine BLIMIT. For each point on the field line defined as the intersection of the orthogonal curve that has an altitude equal to the polar intercept values at the poles, subroutine SPLATR is called to compute the magnetic latitude . The magnetic intensity B is computed from Eq. 123. Subroutine DTEQU is then called with L and as input arguments to compute the distance to the magnetic equator.

84

h. Subroutine CONMAG

Purpose:

Subroutine CONMAG is used to convert from geographic coordinates to magnetic coordinates when the accuracy required (between the real magnetic field and geographic position) is not larger and/or where the computer time for such conversions would be prohibitive otherwise (a modified version of INVAR could be used for this purpose if great accuracy was required and computer time of no concern). This routine is needed since, in general, the neutral and ionospheric model atmospheres required in this code use geographic coordinates as independent variables whereas magnetic coordinates must be used to describe charged particle motion.

Input:

M	A mode option index (M=1,2,3,4,5, or 6)	
	M=1,3 or 5 for centered dipole approximation	
	M=2,4 or 6 for displaced dipole approximation	
ALT	Geographic altitude	M=1,2,3, or 4
DLAT	Geographic latitude in degrees	M=1 or 2
DLONG	Geographic longitude in degrees	M=1 or 2
DMLAT	Sign of geomagnetic latitude	M=3 or 4
	Geomagnetic latitude in degrees	M=5 or 6
DMLONG	Geomagnetic longitude in degrees	M=3,4,5 or 6
EL	Magnetic L-shell value	M=3,4,5 or 6

Output:

ALT	Geographic altitude	M=5 or 6
DLAT	Geographic latitude in degrees	M=3 or 4
DLONG	Geographic longitude in degrees	M=3 or 4
DMLAT	Geomagnetic latitude in degrees	M=1,2,3 or 4
DMLONG	Geomagnetic longitude in degrees	M=1 or 2
DDIP	Magnetic dip angle in degrees	M=1,2,3 or 4
B	Magnetic intensity in gauss	M=1,2,3 or 4
EL	Magnetic L-shell value	M=1 or 2

<u>Method</u>:

For modes M=1 or 2 geographic cartesian coordinates $X_G = (X_G, Y_G, Z_G)$ are computed from the equations

$$X_G = (1 + h/R_E) \cos \lambda_G \cos \phi_G \tag{135}$$

$$Y_G = (1 + h/R_E) \cos \lambda_G \sin \phi_G \tag{136}$$

$$Z_G = (1 + h/R_E) \sin \lambda_G \tag{137}$$

where h is the altitude, R_E is the earth's radius, λ_G is geographic latitude and ϕ_G is geographic longitude. These coordinates are then translated to a magnetic origin by the matrix equation

$$X_T = X_G + T \tag{138}$$

where $T = (.05764855, - .03208677, - .01842101)$ if $M = 2$ and $T = 0$ if $M = 1$. The magnetic cartesian coordinates X_m are then computed by the rotation

$$X_m = AX_T \tag{139}$$

where

$$A = \begin{pmatrix} .97129205 & - .22646696 & .07283175 \\ .23641749 & .95294113 & - .18976292 \\ - .02642934 & .20153391 & .97912490 \end{pmatrix} \tag{140}$$

and $A^T = A^{-1}$

The desired spherical magnetic coordinates are then computed using the relations

$$\lambda_m = \sin^{-1} (Z_m/R_m) \tag{141}$$

86

$$\phi_m = \tan^{-1}(X_m, Y_m) + \Delta\phi \tag{142}$$

where $R_m = (X_m^2 + Y_m^2 + Z_m^2)^{1/2}$ and $\Delta\phi = 1.4137167$ radians (chosen to fit magnetic longitude values obtained from the world data center). The desired magnetic parameters are then computed using the relations

$$L = 1/\max(1. \times 10^{-4}, \cos \lambda_m/R_m), \tag{143}$$

$$B = 0.312 (1 + 3 \sin^2 \lambda_m)^{1/2}/R_m^3 \tag{144}$$

$$\eta = \text{sign}\left[\sin^{-1}(4 \sin^2 \lambda_m/(1 + 3 \sin^2 \lambda_m))^{1/2}, \lambda_m\right] \tag{145}$$

where L is the L-shell, B is the magnetic intensity, and η is the dip angle.

For modes $M = 3$ or 5, the X_m coordinates are first computed and the above equations used in an iterative way to compute the corresponding geographic position (we use the fact that the dipole displacement T is small compared with the distances to regions outside the earth to compute R_m). For modes $M = 5$ or 6, the X_m coordinate is also computed first given R_m. The geographic coordinates are then computed as above from

$$X_G = A^{-1}X_m - T. \tag{146}$$

The altitude can then be obtained since

$$h = 6371.2 \left[(X_G^2 + Y_G^2 + Z_G^2) - 1\right]^{1/2}. \tag{147}$$

1. Subroutine DEBATL

Purpose:

Subroutine is used to perform three basic tasks. First, it is used to compute some required burst parameters and to print out the input debris distribution data for each data plane. Secondly, it is used to compute

87

polar intercepts for the burst point and the data planes, to establish
indicies relating the position of the data planes in the computational
grid, to compute the total number of fission fragments, the total hot-
ion mass and energy and then to scale the input distribution to the total
fission yield as given by the input data (these quantities should be con-
sistent but may not be!). Finally, DEBATL is used to compute the fission
fragment density distribution profile along the length of the flux tube
as is dictated by the motion of the tube on the flux and velocity distribu-
tion at the data planes.

Input:

T   Time in seconds

ACATLC   The labeled common array variables RE, BE, NIS, DMLONG, EL, BDCK,
          PK, SK, BK and FLATK

DEBC   The labeled common array variables TI, ELI, IH, BX, DPR, C, CLDG,
          Q, BALT, BPHID, BLATD, YLD, WF, BR and DEBIN

DATAC   The labeled common array variables NT, DSP, DSN, NTPI, TPI, ETAT,
          AMIT, TD, VIIP, FP, VIIN, FN and DATA
          (See DEBATL code for definitions of variables.)

Output:

TAPE9   Print file (should be rewound and copies to OUTPUT to be listed)

DEBC   The labeled common array variables DPHI, SET, SE, BEQ, BY, C,
          ELO, VI, TDEB, TTBP and SIGMA

DATAC   The labeled common array variables FP and FN

MOVEC   The labeled common array variables ADI and ADID

DEBDAT   The labeled common array variable EDEN
          (See DEBATL code for definitions of variables.)

Externals:

BLIMIT, DPLATR, DTEQU, LINTRP, SFROMB, SLFS, XINDX and YINDX.

Method:

DEBATL defines the burst area A_B in terms of the bubble radius r_b where

$$A_B = \pi r_b^2 \tag{148}$$

The constant azimuthal tube width is defined to be

$$\Delta\phi = \sqrt{A_B}/(R_E L_b \cos \lambda_m)^3 \tag{149}$$

where R_E is the radius of the earth, L_b is the burst L-shell, and λ_m is the magnetic latitude. The total number of available fission fragments, n_{ft} is computed assuming

$$n_{ft} = 1. \times 10^{26} W_f \cdot YLD \tag{150}$$

where W_f is the fission fraction and YLD is the yield in megatons.

However, the total number of fission fragments N_{ft} is also defined by the fission fragment flux at the input data planes since

$$N_{ff} = \left[A_+ \int_0^T F_+ \, dt + A_- \int_0^T F_- \, dt \right] \tag{151}$$

where $A_+ = A_b B_b / B_+$ is the initial area of the higher data plane where the magnetic intensity is B_+, $A+ = A_b B_b / B_-$ is the initial area of the lower data plane where the magnetic intensity is B_-, F_+ is the fission fragment flux at the + data plane, F_- is the fission fragment flux at the – data plane, T is the maximum time, and B_b is the magnetic intensity at the burst point. Thus, this code defines a scaling coefficient C_{ff} such that

$$C_{ff} = n_{ff}/N_{ff} \tag{152}$$

and new flux values $f_+ = C_{ff} F_+$ and $f_- = C_{ff} F_-$ so that the total number of fission fragments is leaving the data planes is n_{ff}.

The flux tube is broken up into three distinct regions (region 1, 2 and 3) for the purpose of computing the fission fragment profile along the flux tube. Region 1 is defined as the portion of the flux tube below the lower data plane (this region exists in only one hemisphere); region 2 is defined as the portion of the flux tube between the lower data plane and the upper data plane (this region includes the burst point). Region 3 is defined as the remaining portion of the flux tube (this region can exist in both hemispheres). The fission-fragment distribution in region 2 is ambiguous and we have chosen to compute the unambiguous mean density of fission fragments in this region and assume it is valid everywhere within the region. Regions 1 and 3 are similar except that region 1 is constrained to the burst hemisphere.

The fission fragment number density at time t in region 2 is computed from the equation

$$n_2(t) = n_2(t') - \left[f_+^A(t) + f_+^A(t') + f_-^A(t) + f_-^A(t') \right] \frac{\Delta t}{2V_2(t)} \quad (153)$$

where $t' = t - \Delta t$ and V_2 is the volume of the flux tube in region 2, $f_+^A = A_+ f_+$ and $f_-^A = A_- f_-$. (Note that f_+^A and f_-^A are the number of fission fragments/sec. Leaving the data planes and that these are conserved quantities independent of the motion of the tube.)

In regions 1 and 3, the debris distribution is assumed to have a front corresponding to time 0 when particles first left the data plane and a tail corresponding to time t if t<T or time T if time t>T when particles last left the data plane. At each time step and for each point along the flux tube occupied by debris, an array of times τ and velocities V are kept that indicate when the particles at the point in question left the data planes and the velocity they had when they left. Similar times and velocities are kept for the head and tail of the distribution. Thus, at each time step the new position of the head and tail, as well as that of the particles that were at the given grid points, can be computed from the

90

old velocity, V. The arrays τ and V can then be updated by interpolating in distance along the field line (note that we assume that the velocity does not change in the particles frame of reference). Then, for each grid point k between the front and tail $f_+^A(\tau_k)$ say, can be computed from which the number density ρ_{ff} can be expressed as

$$\rho_{ff}(k,t) = f_+^A(\tau_k)\left[\tau_k - \tau_k'\right]/\left[A_+(k)\cdot(S_k' - S_k')\right] \tag{154}$$

where $\tau_k' = \tau_k(t - \Delta t)$, $S_k' = S_k(t - \Delta t)$ and $A_+(k)$ is the cross-sectional area of the flux tube at point k and time t.

j. Subroutine DPLATR

Purpose:

This subroutine computes the dipole magnetic latitude λ_m at the point where the L-shell defined by

$$R = L \cos^2\lambda_m \tag{155}$$

intersects the orthogonal shell defined by the relation

$$R = P/\sin^{1/2}\lambda_m. \tag{156}$$

Input:

EL   The magnetic L-shell

P   The polar intercept

Output:

RLAT   The magnetic latitude λ_m in radians.

Method:

The subroutine DPLATR uses the following method to compute λ_k given P_k and L.

First, an approximate value, λ_k^o, is computed using the equations:

$$\lambda_k^o = \begin{cases} 0 & , \; p_k = 0 \\ u_k(1 - .41\, u_k) & , \; u_k < 1.3 \\ \left| \text{Log}_{10}\, u_k \right| (u_k/(2.9\, u_k + 1.5)) & , \; u_k < 75, \; u_k \ge 1.3 \quad (157) \\ \pi/2 - \left| (1-.25/\sqrt{u_k})/\sqrt{u_k} \right|^{\frac{1}{2}} & , \; u_k \ge 75 \end{cases}$$

where $u_k = (L/p_k)^2$.

The approximate value, λ_k^o, is then refined by using Newton's method with:

$$\lambda_k^{i+1} = \lambda_k^i - f_i/(df/d\lambda_k)_i, \quad i = 0,1,\ldots$$

where $f_i = f(\lambda_k^i) = u_k \cos^4 \lambda_k^i - \sin \lambda_k^i$ \hfill (158)

and $\left(\dfrac{df}{d\lambda_k}\right)_i = -\cos \lambda_k^i (4u_k \cos^2 \lambda_k^i \sin \lambda_k^i + 1).$ \hfill (159)

The iteration sequence is stopped when $\left| (\Delta_k^{i+1})/\lambda_k^i \right| < \epsilon \doteq 10^{-6}$.

k. Function DTEQU

Purpose:

This routine computes the distance along a dipole field line to the equator.

Input:

EL   The L-shell defining field line

X   The quantity sine (magnetic latitude)

Y   The quantity $(1 + 3 x 2)^{1/2}$

Output:

DTEQU   The distance to the equator in km where distances are positive north to south.

Method:

The distance to the equator DTEQU is evaluated using the equation

$$\text{DTEQU} = \text{sign} \left[3185.6 \ \text{EL}(|x| y + \ln(\sqrt{3} \ |x| + y)/\sqrt{3}), \ x \right] \tag{160}$$

1. Subroutine EXPINT

Purpose:

This subroutine computes the integral

$$I = \int_{X_1}^{X_2} f(x) \ dx \tag{161}$$

Input:

X1   The value of the independent variable at the lower limit of integration

Y1   The value of the integrand at X1

X2   The value of the independent variable at the upper limit of integration

Y2   The value of the integrand at X2

Output:

DINT   The positive value $|I|$

A   The reciprocal e folding distance between X1 and X2

Method:

$$\text{DINT} = (Y2 - Y1)/A; \ \text{if} \ \begin{cases} Y1 > 0 \\ Y2 \geq 0 \\ Y1 \neq Y2 \end{cases} \tag{162}$$

where $A = \ln (Y2/Y1)/(X2 - X1),$ (163)

and $\text{DINT} = (Y2 + Y1) |(X2 - X1)|/2$ (164)

otherwise

m. Subroutine IONCON

Purpose:

This routine interpolates in altitude from a table of observed relative ion concentrations vs. altitude below 500 km, to compute the ion concentrations of O_2^+, NO^+, O^+, H_e^+ and H^+ given the total ion concentration and altitude.

Input:

H   The altitude where the ion concentration is TC

TC   The total ion concentration or number density at altitude H

Output:

CI   An array of O_2^+, NO^+, O^+, H_e^+ and H^+ ion concentration at altitude H.

Externals:

XINDX

Method:

The relative ion concentrations R_i are interpolated from a table taken from the results of C. Y. Johnson (Ref. 11). The above ion number densities n_i are then computed from the equation

$$n_i = (N/\Sigma \ R_i) \ R_i, \tag{165}$$

where $N = TC$, $n_1 = n(O_2^+($, $n_2 = n(NO^+)$, ..., $n_7 = n(H^+)$ and $n_i = CI(i)$.

n. Subroutine LESSEN

Purpose:

This subroutine is used to store a subset of points from one array into another array each of which are two dimensional with the second dimension equal to two corresponding to two hemispheres.

94

NI	The number of values/hemisphere in AI
NID	The first dimension of AI
NFM	The maximum number of values/hemisphere in AI to be placed in AF
NFD	The first dimension of AF
AI	The array of values to be chosen

Output:

NF	The number of values/hemisphere in AI placed in AF
AF	The array of placed values (note that AI = AF is OK)

Method:

For each hemisphere the array AF is formed from AI such that:

$$AF(J) = AI(K), \quad J=1,2,\ldots,NF$$
$$K=1, \; 1+2I,\ldots,1+(NF-1)I \tag{166}$$

where $I = 1 + (NI - 1)/(NFM -1)$ (167)

$NF = 1 + (NI -1)/I$ (168)

o.   Subroutine LINTRP

Purpose:

This routine does linear interpolation over a monotonic increasing array of independent variables.

Input:

M	=1, when independent variable has changed
	=0, when X, NX and XT have not changed
NX	The number values in arrays XT and YT
X	The value where Y is to be elevated
XT	The independent monotonic increasing variable array
YT	The dependent variable array

95

Output:

Y   The interpolated dependent variable corresponding to X

Externals:

XINDX

Method:

Straight line linear interpolation is used. Some economy in computation can be obtained as in DEBATL where several quantities are interpolated for the same value of independent variable by setting M=0, in which case the interpolating coefficient is not updated.

      p. Subroutine MAGDEN

Purpose:

A model of the earth's ambient ion-plasma is required to evaluate coefficients in the differential equation that governs the motion of the debris tube. MAGDEN provides a global model of the earth's ambient ion concentration as a function of position with annual, diurnal and solar-activity cycles.

Input:

M	=1, for centered dipole field
	=2, for displaced dipole field
ZL	Altitude limit of CHIU's IONDEN code in km
Z	Altitude of geographic point in km
DGLT	Geographic latitude of point in deg.
DGLNG	Geographic longitude of point in deg.
RZUR	Zurich smoothed sunspot number
TL	The local time in hours
TM	Time in months from December 15th of the previous year

Output:

C   The total ion concentration at altitude Z

CI   The array of O_2^+, NO^+, O^+, H_e^+ and H^+ ion concentrations at
        altitude Z

DMLT   The magnetic latitude in deg.

DMLNG   The magnetic longitude in deg.

DDIP   The dip angle of the field line in deg.

B   The magnetic intensity in gauss

EL   The L-shell value

ELP   The L-shell value of the plasmapause at time TL

TIK   The ion temperature in deg. K.

ZIKM   The O_+/H_+ ion transition height in km

Externals:

CONMAG, IONCON, IONDEN, PPLOC and TANDHI

Method:

MAGDEN computes ion concentrations by extrapolating as required Chiu's
ionosphere model (Ref.10) in a theoretical manner that is consistent
with observations. The ion concentrations are extrapolated beyond alti-
tudes of 500 km with the help of new subroutines PPLOC, TANDHI, and CONMAG.
PPLOC interpolates to compute the mean L value position of the plasmapause
as a function of local time. TANDHI computes ion temperatures and O^+/H^+
ion transition heights as a function of magnetic latitude and local time
from a model based on the work of Titheridge (Ref.13). CONMAG computes
the magnetic latitude, λ_m, magnetic longitude, ω_m, field intensity, B, and
L-value as a function of geographic position. It also computes geographic
latitude, magnetic latitude, and intensity for a given altitude, field
line and magnetic longitude.

At a given geographic point (h, λ, Φ) above 500 km and local time, MAGDEN
computes the ion concentration in the following manner:

97

1. The L-value of the plasmapause Lpp is computed from the local time.

2. The magnetic coordinates (λ_m, ϕ_m), B, and L are computed.

3. The magnetic latitude, λ_m (1000) at an altitude of 1000 km along the field line (L, ω_m) is computed.

4. The ion temperature, T, and O^+/H^+ transition height, h_t, are computed from λ_m (1000), local time, and perhaps season.

5. The latitudes, λ_m (500) and λ (500), at an altitude of 500 km along the field line are computed.

6. The total ion concentration, $N_I = N_e$ (500), is computed from Chiu's model where we assume N_I (500) = $[O^+(500)] + [He^+(500)] + [H^+(500)]$.

7. Assuming diffusive equilibrium and a constant ion temperature, T, the scale heights of H^+ and O^+ are computed. Then the ratio $[H^+]/[O^+]$ at 500 km is determined knowing that at the transition altitude, $[O^+(h_t)] = [H^+(h_t)]$.

8. The ratio $[H^+]/[O^+]$ at 500 km is computed by using the observation that at this altitude $[H^+]/[He^+] \approx 7$; hence $[He^+]/[O^+] = [H^+]/7[O^+]$.

9. The concentration $[O^+(500)]$ is then computed from the equation $[O^+] = N_I/(1 + [H^+]/[O^+] + [He^+]/[O^+]$ whence the concentrations $[He^+(500)]$ and $[H^+(500)]$ are determined.

---------------- For $500 < h \le h_t$ or $L \le Lpp$ --------------------

10. The concentrations of O^+, He^+, and H^+ are computed using the known values at 500 km (from step 9) and the computed scale heights.

------------------ For $h > h_t$ and $L > Lpp$ ----------------------

q.   Subroutine MOVEL

Purpose:

This subroutine is used to solve the equivalent circuit differential Equation
(43) at each time step and thus, to compute the motion of the convecting flux
tube via Equation (42).

Input:

T	Input time in seconds
DT	Time increment of step
EL	L-shell value at input time
Q	Charge on flux tube in coulombs at input time
QD	1st time derivative of Q at input time
R	Ionospheric resistance in ohms
C	Capacitance of flux tube in farads at input time
FL	Inductance of flux tube in henrys at input time
DPHI	Longitudinal width of the flux tube in radians
PHID	The mean drift rate for electrons in the flux tube at input time
SE	The total integrated undecayed, trapped electrons in the flux tube at input time
ADI	The azimuthal drift current in amps due to debris at input time
ADID	The 1st time derivative of ADI in amps/sec. at input time.

Output:

T	Output time in seconds
EL	L-shell value at output time
Q	Charge on the flux tube in coulombs at output time
QD	The 1st time derivative of Q at output time
QDD	The 2nd time derivative of Q at input time
F	The right hand side of equation 43
DI	Drift current in amps due to both debris and injected electrons
DID	The 1st time derivative of DI at input time.

Method:

A simple modified Euler numerical method is used to solve the circuit equation for
Q. The L-shell value is updated by integrating Equation (42) over the input time
step.

r.   Function PHIDOT

Purpose:

This routine computes the azimuthal drift velocity for electrons as a function of
L-shell position, energy and pitch angle.

Input:

EL	The L-shell position
EMEV	The electron energy in meV
S	$\mid$ sine (pitch angle)$\mid$

Output:

| PHIDOT | The angular drift velocity in radians/sec. |

Method:

The azimuthal drift velocity $\dot{\phi}_D$ is computed from the equation

$$\dot{\phi}_D = f(L)g(E)h(\alpha) \tag{169}$$

where

$$f(L) = .0012071L, \tag{170}$$

$$g(E) = (1+E/.51098) - (1+E/.51098)^{-1}, \tag{171}$$

$$h(\alpha) = \frac{C_1 + C_2\alpha + C_3(\alpha \mid n\alpha + \sqrt{\alpha})}{\beta_1 + \beta_2(\alpha + \sqrt{\alpha})}, \tag{172}$$

and where $L = EL$, $E = EMEV$, $\alpha = S$, $C_1 = .460058$, $C_2 = -.036510$, $C_3 = -.053308$,
$\beta_1 = 1.380173$ and $\beta_2 = -.319846$. The code gains economy in computation by not
recomputing $f(L)$, $g(E)$ or $h(\alpha)$ if the corresponding input arguments do not change.

s.   Subroutine PLACE

Purpose:

This subroutine places a subset of values from an array dimensioned (ND, 2), where
the second dimension is 1 for northern hemisphere data and 2 for southern hemis-
phere data, into a single dimensioned array in such a manner that the new data
array is monotonic from south to north.

100

Input:

N	The number of values in the input array D for each hemisphere
ND	The maximum value of N and the 1st dimension of array D
D	The input data array dimensioned (ND, 2) with data arranged in each hemisphere from cutoff to equator

Output:

| R | The single dimensioned output array of 2N-1 values where R(1) is the southern most R(N) is the equatorial and R(2N-1) is the northern most values. |

Method:

N data from the southern hemisphere of D are stored sequentially into R and N-1 data from the northern hemisphere of D are stored in reverse order.

        t.   Function PPLDC

Purpose:

This routine interpolates to find the mean location of the L-shell value of the plasmapause boundary as a function of local time. This boundary represents a transition between open and closed field lines. Within this boundary the ionosphere is well represented by a diffusive equilibrium model, while just outside the boundary a convective model applies.

Input:

| TL | The local time in hours from midnight |

Output:

| PPLOC | The L-shell boundary of the plasmapause |

Method:

The plasmapause position is interpolated for in time from a table obtained from the observations of D. L. Carpenter (Reference 12).

u.   Subroutine SINMLT

Purpose:
This subroutine computes the absolute value of the sine of the magnetic latitude at a point given by the ratio of the magnetic intensity at the point to the magnetic intensity at the equator.

Input:
BTBEQ   The ratio B/B_0

Output:
SMLT   The value $|\text{sine (magnetic latitude)}|$

Method:
Subroutine SINMLT computes the absolute value of $x = \sin \lambda_m$ given the ratio B/B_0 of magnetic intensity of the point in question to that at the equator. Newton's method is used where the solution to the equation

$$f(x) = 1 + 3x^2 - (1-x^2)^6 \, (B/B_0)^2 = 0 \tag{173}$$

is sought. An initial guess for $x=x_1$ is taken to be $x_1 = [(B/B_D)^2 + 1] / [6(B/B_0)^2 + 3])^{1/2}$ if $B/B_0 < 2.66$, or $x_1 = (1 - 3(B_0/B)^{1/6})^{1/2}$ if $B/B_0 \geq 2.66$. Thus, given the initial value of x the subroutine iterates using the relationship $x_{i+1} = x_i - f(x_i)/f^1(x_i)$, i=1, 2, 3 ... until $|x_{i+1} - x_i| \leq 10^{-6}$, where $f' = \dfrac{df}{dx}$.

v.   Subroutine SLATSQ

Purpose:
This subroutine computes η_m^2 the square of the dipole latitude corresponding to the mirror point of an electron with a given equatorial pitch angle.

Input:
K   = 0, if SLAT2 is input
               = 1, if SLAT2 is not input

SPA	The sine of the equatorial pitch angle
SPA2	The square of SPA
SLAT2	The initial guess if $k = 0$

Output:

| SLAT2 | The square of the sine of the dipole latitude |

Method:

Subroutine SLATSQ computes η_m^2 given $\sin^2\alpha_0$ by an iterative method using the relationship

$$\sin^2\alpha_0 = (1-\eta_m^2)^3/(1 + 3\eta_m^2)^{1/2}. \tag{174}$$

This method consists of computing a first approximation for η_m^2 using the equation,

$$\eta_{m,1}^2 = \frac{(23/16)-\sqrt{(23/16)^2 - 4\,(1231/1024)\,(T/T_0-1)}}{2\quad(1231/1024)}, \tag{175}$$

$$T \leq T^* = T_0 \left[1 + 1/4\,\frac{(1024)}{(1231)}\,\frac{(23)^2}{(16)} \right]$$

$$= \quad 1, \text{ when } T > T^*$$

where

$$T = 1.380173 - .639693(\sin^2\alpha_0)^{0.37} \tag{176}$$

and

$$T_0 = \pi/3\sqrt{2} = 1.380173 - .639693. \tag{177}$$

Equation (174) is then used in the following iterative manner

$$\eta_{m,i+1}^2 = 1 - \left[\sin^2\alpha_0(1 + 3\eta_{m,i}^2)^{1/2} \right]^{1/3} \tag{178}$$

to obtain a precise value of η_m^2

w.   Function SLFS

<u>Purpose</u>:

This routine computes the sine of the dipole latitude corresponding to a given distance along a specified field line.

<u>Input</u>:

EL   The L-shell value of the field line

S   The distance in km to the equator from the point of interest

<u>Output</u>:

SLFS   The sine (dipole latitude)

<u>Method</u>:

An initial guess is provided by the equation

$$\alpha_0 = |S/LRe| \tag{179}$$

This guess is constrained to be less than 1.380173 and then refined using a quadratic approximation

$$\alpha_1 = \alpha_0(1 - .199579\alpha_0) \tag{180}$$

This is followed by two iterations using the following equation.

$$\alpha_{i+1} = \frac{1}{2} \quad \alpha_i + (2\alpha_0 - \ln(\sqrt{3}\alpha_i + R)/\sqrt{3})/R \tag{181}$$

where SLFS = α and R = $\sqrt{1+3\alpha_i^2}$

x.   Subroutine TANDHI

<u>Purpose</u>:

This subroutine computes a mean ionospheric temperature and the O^+/H^+ transition height (the altitude where $n(O^+) = n(H^+)$) as a function of magnetic latitude and local time.

104

<u>Input</u>:

M   = 1, if TIK and HIKM are both to be computed

     = 2, if only TIK is to be computed

     = 3, if only HIKM is to be computed

DML   The magnetic latitude in deg.

TL   The local time in hours from midnight

<u>Output</u>:

TIK   The ion temperature in deg. K

HIKM   The O^+/H^+ transition altitude in km

<u>Externals</u>:

VOFY

<u>Method</u>:

The data used in this code is taken from the work of J. E. Titheridge (Reference 13). The ion temperature is computed for daytime (noon) and nighttime (midnight) from previously stored spline interpolating coefficients as a function of the absolute value of magnetic latitude. A simple linear interpolation in local time is made between these two values to obtain the temperature at the input local time.

The O^+/H^+ transition altitude is similarly computed as a function of magnetic latitude, however, we are forced to assume that the day night variation which we can compute for the northern hemisphere also applies in the southern hemisphere.

   y. Test Cases

Three test cases for the tube-motion model, including the new input data have been provided. These test cases are for ARGUS-3, STARFISH and TALL BEAR. All of these runs use AMBCAP to compute the tube capacitance and resistance, DEBCON

to compute the tube motion and debris distribution and the old SPECTER INJECT and FLUXS code to compute drift dilution and decay of the injected electrons. The STARFISH test case also exercised the new DSTRIB code to estimate the redistribution of the injected electrons by the electric field in the tube.

The input to AMBCAP specifies the geographic altitude, latitude and longitude, the local time and the day of the year. The DEBCON input is yield, kinetic-yield fraction, burst radius, NRL reference plane distances, final time and time increment. The ARGUS-3 case is a low-yield, high-latitude, southern hemisphere run; STARFISH is a medium-yield, low-latitude, northern hemisphere run, and TALL BEAR is a high-yield, high-latitude, northern hemisphere test. In all cases the tube motion time increment was chosen so that the details of the debris flux and velocity profiles specified in the reference planes could be resolved. The burst radii were taken from the results of the LMSC code that computes the reference plane parameters and cross-sectional area.

A test case has also been provided for the new saturation model based of flux limiting due to strong diffusion. In this test the injection rate is 100 MT/sec for a duration of 6 hours. This rate establishes a flux which exceeds J^*, the equilibrium flux, except at very low L values where the decay rate is very high due to collisions. The flux is iso-tropic and constant along the magnetic field until after the duration of the nuclear exchange (6 hours). It then decays at a diminishing rate, approaching the normal-mode decay rate asymptotically, as discussed in Section IV.4.

The results of the test cases are described in the detailed output listings which have been provided.

106

SECTION III

COMPARISON OF COMPUTED FLUXES WITH TESTS DATA

In this section the distributions of trapped electrons computed for the Argus-3 and Starfish bursts are described and compared with the available data on the radiation belts produced by those nuclear tests.

1. ARGUS-3

During the Argus tests, three identical devices, Argus 1, 2, and 3, were detonated at altitudes greater than about 200 km in the region of the South Atlantic geomagnetic anomaly in late summer, 1958. The yields were in the range 1-2 KT. Each device produced an intense, narrow radiation belt that persisted for several weeks. The belts, at least at early times, were quite similar.

For the Agrus-3 test, we received from NRL the initial distribution of the hot ions (the ionized debris and accompanying energetic-air ions) at the reference planes described in Section II.3a. The fission-fragment flux and the total ion flux at the reference planes are shown in Figure 19. The velocities of the ions in the reference planes were initially about 510 km/sec but rapidly diminished monotonically, qualitatively in the manner of the fall-off of the velocities of the ions for the Spartan bursts shown in Figure 17, reaching a value of about 80 km/sec 10 seconds after the burst. The effective azimuthal width of the debris tube was 0.044115 rad, and the resistance was taken to be less than the critical value discussed in II.2b, subsection (b).

The motion of the debris tube, computed by using the above data as input to the new injection model, is shown in Figure 27. There, the L value of the center line of the tube is plotted against time. As expected for small dis-placements of the tube, the motion is oscillatory. The thickness of the intense region of the resulting radiation belt, according to the model, can-not be less than the width ΔL of the debris tube, which is $\Delta L = L_o \Delta \phi = .10 R_E$.
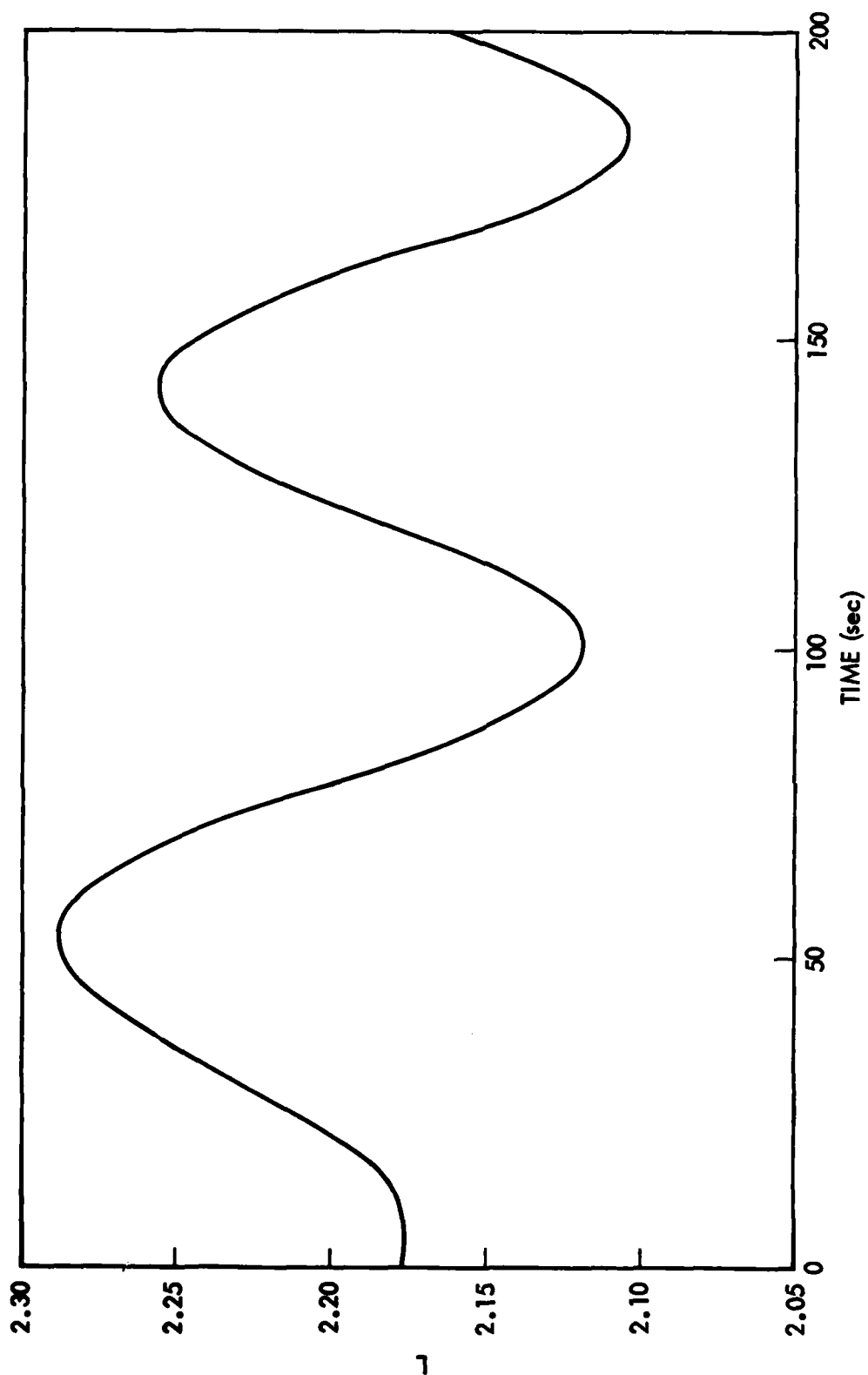
Figure 27. Motion of Argus-3 debris tube.

108

If the source of the injected electrons remains strong in the tube at times greater than 15 or 20 seconds, the displacement of the tube toward higher L values would spread the electrons over a wider range in L. The thickness in L of the Argus-3 shell, based on a measurement by the Explorer IV satellite at $B \simeq .23$ gauss, about four hours after the burst, was about 0.146 R_E (Ref. 14). This thickness is consistent with the width of the debris tube and the effective duration of the electron source during the tube motion.

Unfortunately, the L grid selected to read out the fluxes of the injected electrons was not fine enough to resolve the shell thickness. The maximum flux was at an L value near burst L value. At the next grid joint, displaced from the first by $\Delta L = .07 R_E$, the flux had dropped off substantially. The flux computation in the belt has been compared only with a measurement made with Van Allen's Geiger counter (Channel 3) during the Explorer IV traversal of the belt 4 hours after the burst. This detector had a nominal threshold energy of 3 MeV and a geometric factor of about 0.6 cm^2. Its counting rate at $B \simeq .23$ gauss, as given in a graph in Ref. 14 depicting the decay rate of the belt, was about 4×10^4/sec. Hence, the measurement implies an omnidirectional flux of $6 \times 10^4 cm^{-2} \cdot sec^{-1}$ of electrons of energy greater than about 3 MeV. The computed flux in the most intense region of the belt just after the flux became uniform in longitude, at a B value near .23 gauss, was 4.7×10^7 1 MeV-equivalent electrons per cm^2 per sec. This flux corresponds to a fission beta spectrum of electrons of energy greater than 3 MeV of about $4 \times 10^5 cm^{-2} \cdot sec^{-1}$, an order of magnitude greater than the measured value given above. This discrepancy is not regarded to be excessive in view of the uncertainties in the measurement and in the fission-fragment distribution. Moreover, the comparison was made at a low altitude where the flux was changing rapidly in time and in B value. Further comparisons of the computed fluxes with experimental data are needed. Such comparisons will be facilitated by the results of a separate effort funded by the AFWL to assemble and assess all of the data obtained in the high altitude nuclear tests.

In the Argus tests the debris tube moved so slowly that the redistribution of the electrons was negligible. Indeed, all of the available measurements indicated that the energy spectra of the electrons were indistinguishable from the equilibrium fission beta-decay spectrum.

2.   STARFISH

The fission-fragment flux in the reference planes for the Starfish burst, determined from the data provided by NRL, is shown in Figure 28. The dashed curve in that figure shows the ratio of the fission-fragment flux to the total, energetic-ion flux. At the earliest time, about 0.2 sec, at which the hot ion flux appears at the reference plane, the flux ratio is .00917, and the hot ion flux consists almost entirely of debris at that time. The hot air predominates at later times as mentioned previously. The velocity of the hot ions at the reference plane as a function of time is shown in Figure 29. The azimuthal width of the debris tube was .07778 rad, and the resistance appropriate for the undisturbed ionosphere along the tube motion was .774 ohms.

The debris tube motion resulting from these input data is shown in Figure 30. Note that the tube accelerates monotonically as it convects through the magnetosphere to L values beyond the trapping limit. This behavior of the tube motion was found to be the same for all the high-yield (>1 MT) bursts for which input data was received from NRL, viz, for Tall Bear and the Standard Spartan bursts at L-3 and at altitudes 200, 300, 400, and 600 km. The energy-differential, omnidirectional fluxes of the redistributed electrons at various L values are shown in Figure 21. As discussed previously, the corresponding fluxes that are uniform in longitude, neglecting the small effects due to decay and the "atmospheric-wiper" action, can be obtained from the values in Figure 21 by multiplying by the ratio $\Delta\phi/2\pi$. Measurements of the trapped-electron spectra in the L range 1.25 to 1.70 were made by West et al. (Refs. 15 and 16), several months after the Starfish test, with a mass spectrometer on the Starad satellite. Their spectra at various L values, together with the computed spectra (the fluxes of Figure 21 multiplied by $\Delta\phi/2\pi$) for the specified L values, are shown in Figure 31. Because of the presence of natural

110
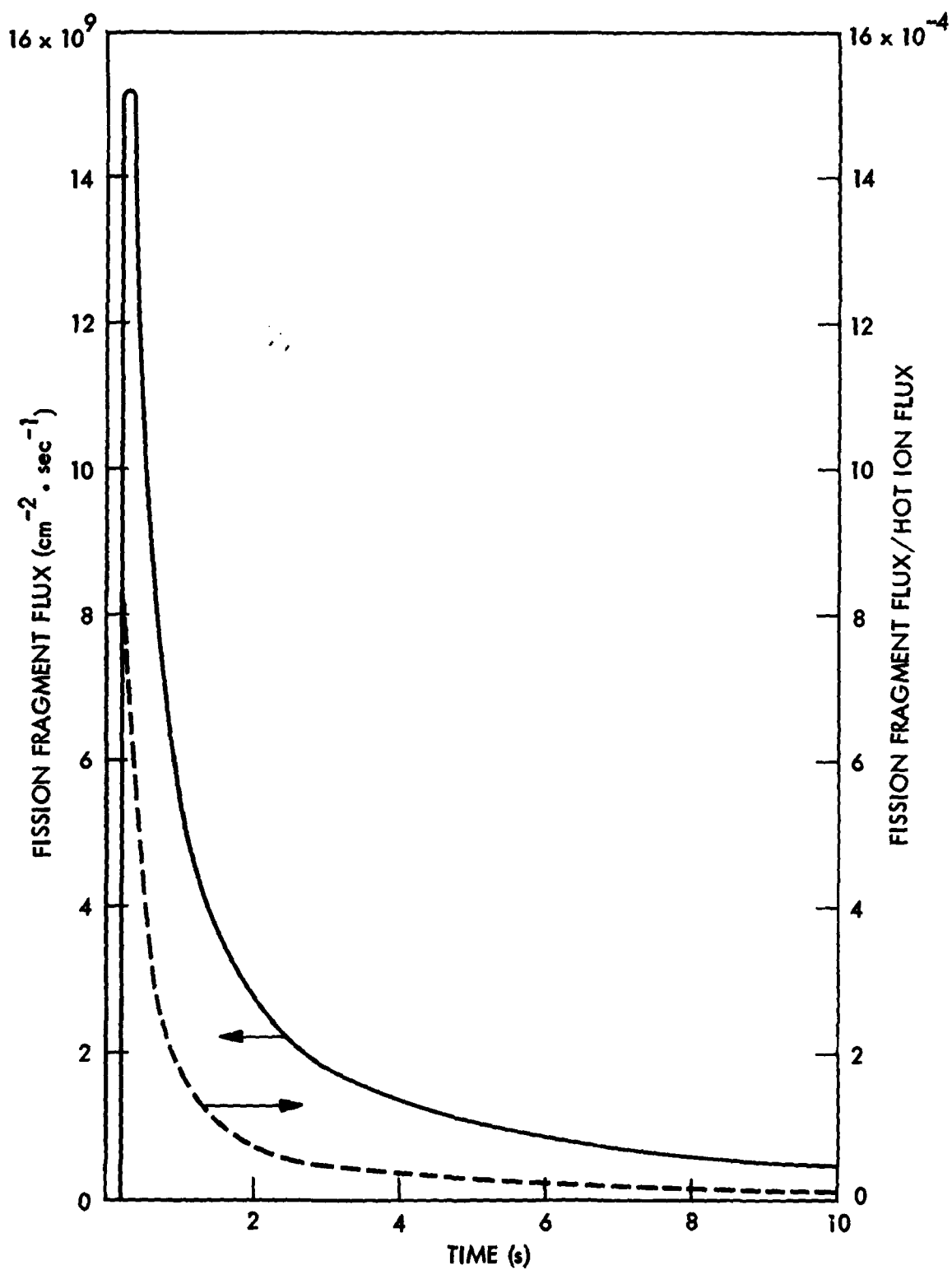
Figure 28.   Flux of Starfish fission fragments (solid line)
and ratio of fission-fragment flux to total hot-
ion flux (dashed line) at reference planes as
function of time.

111
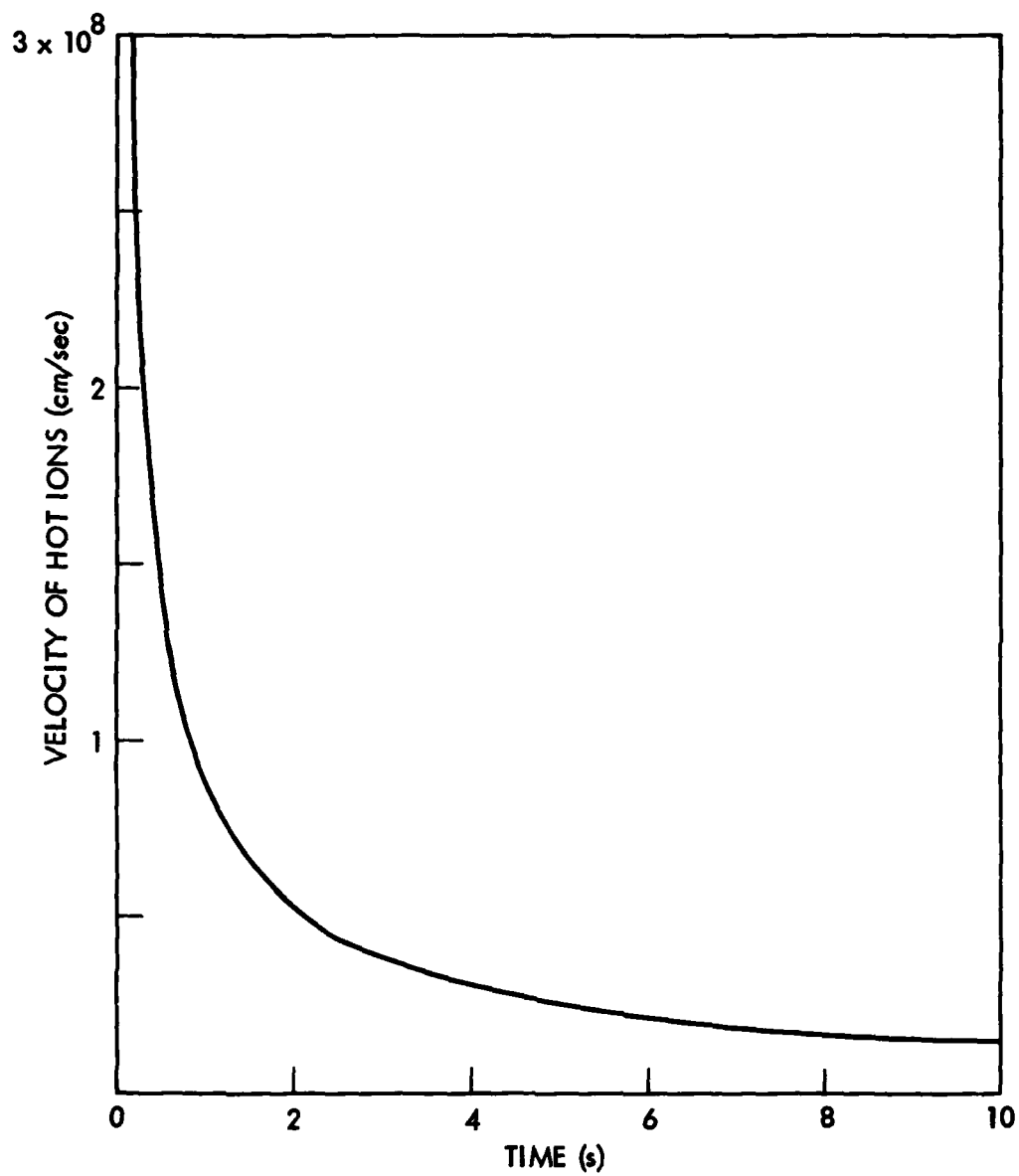
Figure 29.   Velocity of Starfish hot ions along magnetic field, at reference planes, as function of time.

112
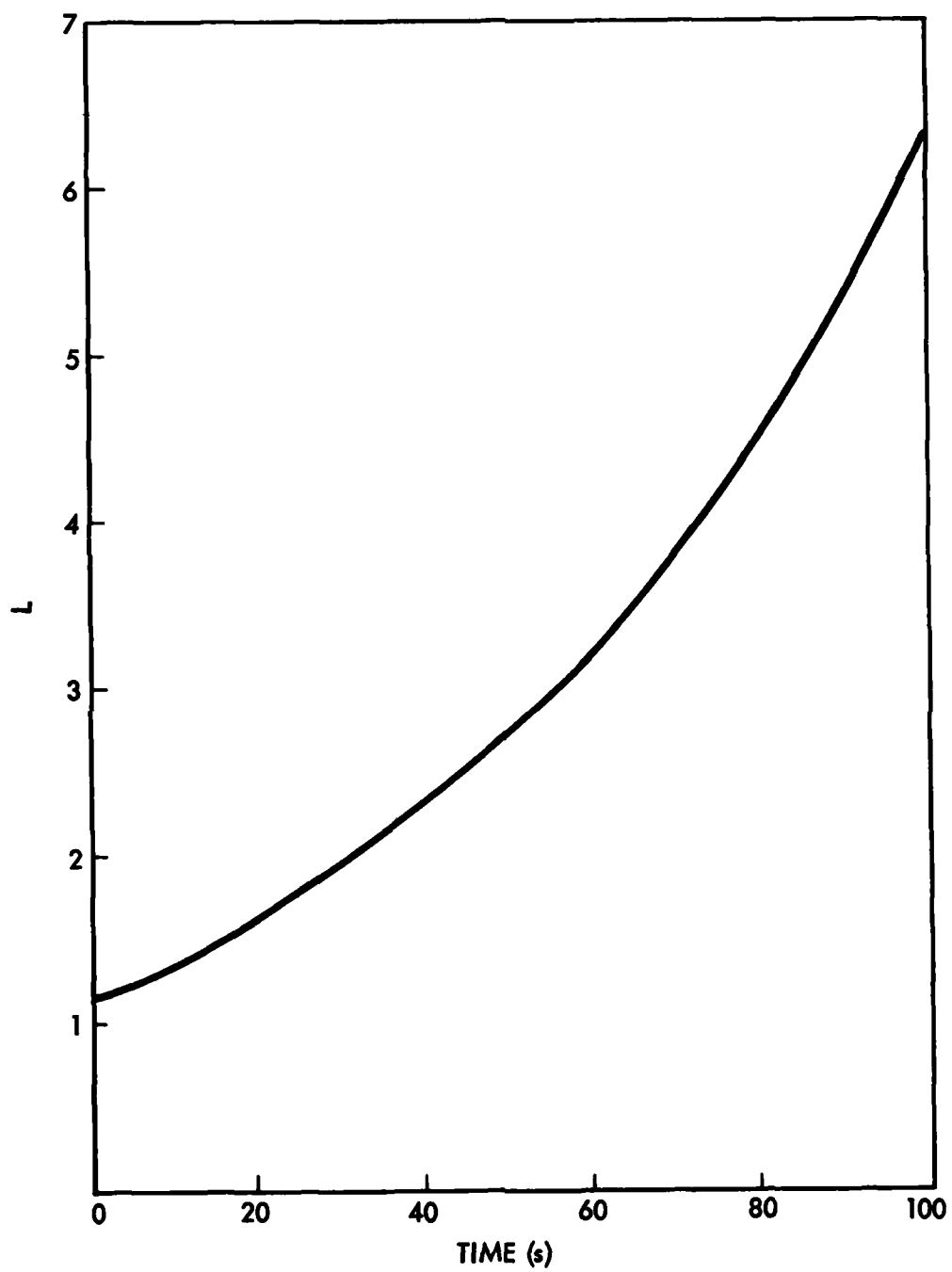
Figure 30.   Motion of Starfish debris tube.
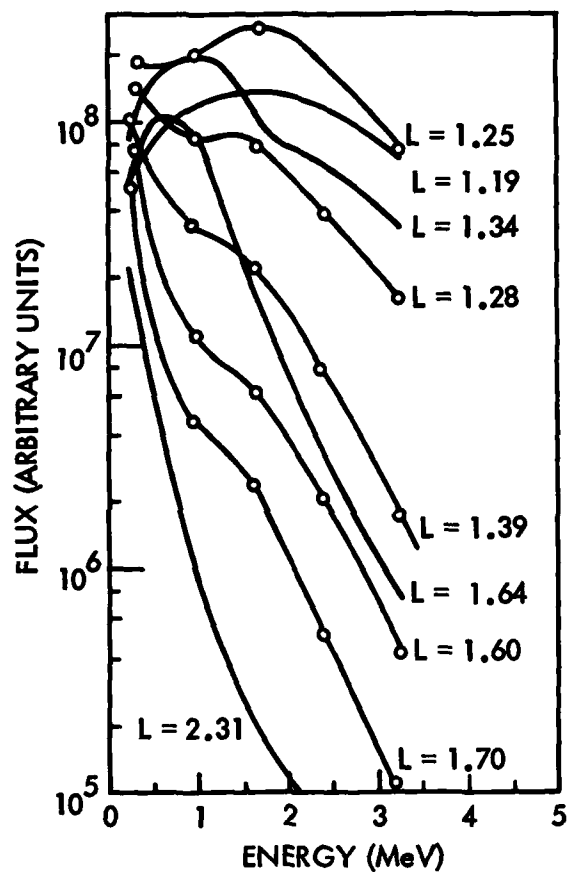
Figure 31. Experimental spectra of radiation belt
electrons following Starfish (Reference 15).
The solid-line curves without the open
circles are the computed spectra of the
redistributed electrons (see Figure 21).

114

trapped electrons and the decay of the Starfish electrons, detailed agreement is not expected. However, the general softening of the computed spectra at increasing L values is verified by these data.

The comparison of the equatorial, omnidirectional flux with the Telstar data, however, is not so favorable. Here, the electron distributions computed with the new injection model and with the old jetting model are both in disagreement with the Telstar data at L values above the peaks of the distributions. In making the comparison, the effect of the different electron spectra given by the two models was removed by computing the response of the Telstar detector to the fluxes by integrating the counting efficiency of the detector given in Ref. 17 (channel 3, with lower and upper pulse-height edges at 390 and 615 keV, respectively) over the energy spectra of the fluxes. The resulting counting rates are shown in Figure 32. The open circles are the counting rates of the Telstar detector, at the equator, two days after Starfish. The solid curve gives the counting rate expected for the flux computed with the new injection model. Here, decay is not included. The detector response was computed by using the spectra shown in Figure 21 with the spectral intensities reduced by the factor .07778/2π. The broken-line curve in Figure 32 is the counting rate expected if 27% of the debris jets. This is the magnitude of the jetting expected at early times when the ram pressure of the debris exceeds the magnetic-field pressure. The broken-line curve was computed using the old jetting model, assuming the equilibrium fission beta-decay spectrum, and applying a two-day decay factor. The data should be compared with the sum of the computed counting rates, which are approximately the rates expected if the debris both jets at early times and is carried upward by the tube motion at later times. As shown in the figure, the computed counting rates are in fairly good agreement with the data at L$\leq$1.6. However, at the higher L values, the Telstar data lie higher than the computed values by an amount that increases with increasing L value.

It is well known (see e.g. Ref. 18 and 14) that the fluxes measured by Telstar were much higher than those inferred from the Injun satellite at
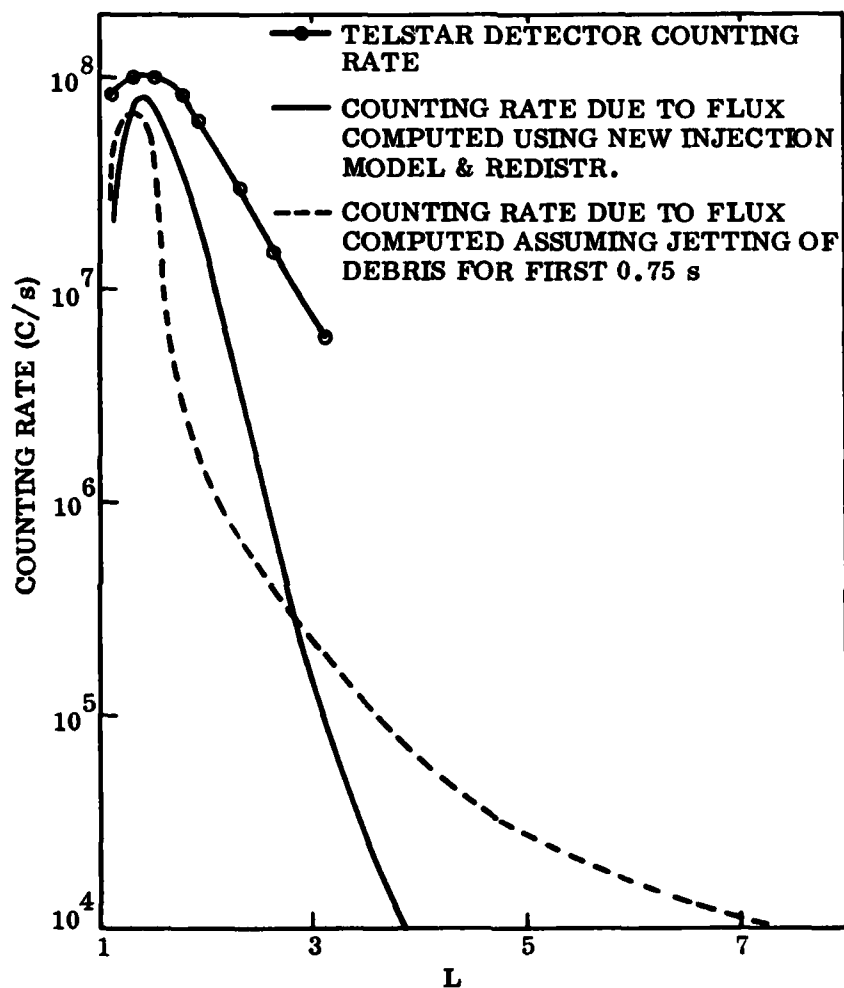
Figure 32.   Counting rate of Telstar detector (open circles) near equator
              as function of L, together with counting rate of detector
              due to fluxes computed with new injection model (solid line)
              and jetting model (broken line).

L>1.4. It was thought that this discrepancy might be accounted for
by the redistribution process in the debris tube which transports
lower-energy electrons to higher L values. But, as shown in Figure 32,
this redistribution of the electrons is not sufficient to account
entirely for the Telstar measurements. The Telstar data have not been
corrected for background measurements; the natural radiation prior to
Starfish, in the energy sensitivity region of the detectors, was not
known since Telstar was launched a day after the Starfish burst.
Vette's AE-4 (1964) steady-state environment for E>500 keV for solar
minimum (Ref. 19) indicates that less than one-tenth of the detector
response can be attributed to the steady state background radiation.
Of course, the natural radiation in the region of the slot, where the
discrepancy occurs, is highly dependent on storm-time activity; the flux
can easily increase by an order of magnitude during magnetic storms.
However, no major magnetic storms occurred for several months prior to
Starfish. The discrepancy might be explained by one or more of the
following processes:

i)   the injected electrons might have drifted to the appropriately
     higher L values while they were bunched in longitude, as dis-
     cussed in Section II.4b, or even at later times due to the fluting
     instability,

ii) the oscillations of the magnetosphere due to the explosion might
     have caused the trapped electrons in the outer radiation zone to
     diffuse into the slot region, and

iii) the counting rate of the Telstar detector might have been enhanced
     due to the acceleration of ambient electrons by processes associated
     with the e. .losion.

The latter possibility was first suggested by Colgate (Ref. 20); he esti-
mated that the counting rate of the Telstar detector could be due to the
acceleration of ambient electrons by the upward-moving collision-free
shock produced by the explosion. Papodopoulos, during the Specter Review

117

held at NRL, also discussed a shock mechanism capable of accelerating ambient electrons to very high energies. If high fluxes of such electrons are accelerated to energies higher than about 3/4 MeV, they would be of importance to the SPECTER program and should be assessed carefully.

The combination of debris jetting at early times (<.75 sec) and debris-tube convection, including redistribution, appears to give results for Starfish that are consistent with the majority of the experimental data. The modeling of these processes contains the correct first-order physics. The jetting is expected theoretically and it has been observed optically (Ref. 21); it also explains the high fluxes (about 10^5 effective 1 MeV electrons per cm^2 per sec) at low altitudes on L≈7 inferred from an analysis of the response of the heavily-shielded Geiger counter on the ARIAL satellite (Ref. 22) using the calibrations of similar detectors by O'Brien et al. (Ref. 23). At the lower L values, the results are in general agreement not only with the Telstar data, as discussed above, but also with Injun data. Of course, further comparisons of the computed fluxes with the data are needed in regions off the equator.

For high-yield bursts, owing to the equipotential-field-line approximation used in the debris-motion model, the effective inductance of the field lines and the expected anomalous resistivity along the field cause the potential to vary along the magnetic field. The effect is such that, at early times, while the majority of the electrons are injected, the electric field across the tube at the lower altitudes is not as high as the model predicts. Hence, the debris density and the attendant electron injection at low altitudes are somewhat lower at high latitudes than predicted by the model.

The hot-air plasma has rendered the debris-tube motion for high-yield bursts, such as Starfish, rather insensitive to wide variations of both the ionospheric resistance and the tube width. Hence, the electron distribution given by this model is now almost entirely dependent on the plasma data provided by NRL.

SECTION IV

THE APPROACH TO SATURATION

1.   THE MECHANISMS OF SATURATION IN THE RADIATION BELTS

Trapped electrons are subject to the influence of electromagnetic
waves, and can actually cause the generation of waves in many modes.
Whenever the unstable generation of waves results in a loss of particle
energy, the particles are redistributed or lost. The problem of
particle loss then boils down to a question of which modes of wave-
particle interactions dominate. In the natural radiation belts it
seems fairly certain that a major part of the energetic electron loss
is due to interactions with waves in the electromagnetic cyclotron,
or whistler, mode. Several mechanisms have been proposed for the way
electrons are removed by interactions with waves. In the Kennel and
Petschek theory (Ref. 24) self interactions limit the electron fluxes:
when the fluxes increase momentarily, the wave generation and subsequent
pitch angle diffusion are enhanced. The Lyons, Thorne and Kennel theory
(Ref. 25) invokes the same wave modes, but the waves are not self-
excited. The waves are supposed to fill the entire trapping region,
and can originate anywhere within the magnetosphere. More recently,
it has been suggested (Ref. 26 through 30) that man-made VLF waves can
cause a large part of the electron losses in the natural radiation belts.
The mechanism is superficially similar to the Lyons, Thorne, and Kennel
mechanism; but the waves may be coherent, which results in diffusion
rates significantly higher than the quasi-linear rates (Ref.[31]).

Though there is some controversy about the true importance of self-
excitation of waves in the natural radiation belts, there is no question
that self-excited waves must eventually limit the total number of electrons
that can be trapped. It also appears that the trapping limit must occur
long before the particle pressure overwhelms the trapping field pressure
(beta > 1). In fact we know that it takes a very well designed experi-
ment to exceed the beta = 1 limit in laboratory plasmas. The aftermath

119

of a high altitude nuclear explosion is highly chaotic, and very
unlikely to provide the uniform conditions needed for very high beta
ratios. So, it is worthwhile to ask whether the Kennel and Petschek
mechanism limits the electron fluxes before the beta criterion is
reached. A secondary concern, to which we have no answers yet, is
whether other wave modes might be as important as the cyclotron mode
at high flux levels. (Electrostatic modes are conceivable candidates
for a flux limiting mechanism.)

One criterion relevant to the importance of various wave particle inter-
actions is their characteristic electron removal times. High beta
instabilities generally result in hydromagnetic waves, which cannot
remove electrons faster than an Alfvén wave can travel along a field
line. Alfvén wave travel times are generally of order several minutes
in the outer radiation belts. These times seemed short enough that
a beta criterion was used in the early versions of Specter to
limit the electron flux at saturation. The characteristic time for cyclotron
wave interactions, on the other hand, is the strong diffusion lifetime.
At saturation there is a geometrically determined limit to the time taken
for a trapped particle to diffuse from a pitch angle near 90° to a pitch
angle in the loss cone. In strong diffusion the lifetime is independent of
the wave amplitude. The electrons cannot be removed faster than the strong
diffusion lifetime, which in the radiation belts is about 10 to 100 seconds
(Ref. 4). This lifetime is generally somewhat smaller than the Alfvén
travel time, so it is reasonable to suppose that the Kennel and Petschek
mechanism does indeed limit the saturation fluxes.

A major criticism of the Kennel and Petschek theory is that it requires
containment of the waves. Whistler-mode waves, however, often propagate
at large angles to the magnetic field. It is not clear, therefore, whether
a thin shell of artificially trapped electrons would be subject to the Ken-
nel and Petschek limit. The application of a Kennel and Petschek limit
to the debris tube, before drift dilution of the electrons, is also some-
what questionable. It might be supposed that the debris tube provides an
effective duct for whistlers, but the wave reflection coefficient and many
other critical parameters remain unknown.

The aim here is to develop a loss model wherein the saturation electron loss rate depends only on the flux level. At low flux levels the loss rate must revert to the natural decay rate. The model may be faulty at very early times — due to the possibility of hydromagnetic instabilities and to our imperfect understanding of wave propagation in the debris tube — but a single injection event is very unlikely to reach saturation. Where the new model becomes particularly useful is in the multi-burst case, where many injection events can occur within time scales of minutes. The total field energy in the trapping field is equivalent to about 150 MT (Ref. 32). A relatively small number of high-yield explosions might exceed the beta=1 limit. Whether saturation ever does occur will be the subject of the following subsections.

2. THE NON-LINEAR MODEL OF SATURATION

Schulz (Ref. 33) has proposed that the particle flux must decay as

$$\frac{dJ}{dt} \stackrel{\sim}{=} \frac{\lambda J}{1+\lambda\tau_s} + S_o \tag{182}$$

where λ is a diffusion loss rate (or reciprocal diffusion lifetime) and τ_s is the strong diffusion lifetime. Eq. (182) is applicable to the Omni-directional flux at the equator, J. The first term on the right contains the effects of self-excitation of waves, and is limited at high diffusion rates to $-J/\tau_s$. The remaining term, S_o, contains the effects of particle sources; in equilibrium

$$S_o = \frac{\lambda_o J_o}{1+\lambda_o\tau_s} \tag{183}$$

Typical values for the equilibrium flux, J_o, and equilibrium (parasitic) diffusion rate are

$$10^4 cm^{-2} sec^{-1} < J_o < 10^{+6} cm^{-2} sec^{-1} \tag{184}$$

$$10^{-7} sec^{-1} < \lambda_o < 10^{-5} sec^{-1} \tag{185}$$

Kennel and Petsche(Ref. 24) proposed that the diffusion rate increases with flux, and that λ is proportional to the wave amplitude squared. The differential equation for λ must contain terms related to the wave growth rate, the wave absorption rate, and an external source of waves to account for parasitic diffusion. Schulz proposes an equation for λ that reduces to

$$\frac{d\lambda}{dt} \simeq - P\frac{dJ}{dt} - Q(\lambda - \lambda_o) \tag{186}$$

Though the model is an extreme simplification, Eq. (5) probably represents the physics fairly well to first order in J and λ. The parameters P and Q are related to the Kennel and Petschek limiting flux, J^*, the growth rate at the limit, γ^*, the wave group velocity V_g, and the wave reflection coefficient, R, thus

$$P \approx \frac{2\gamma^*}{J^*} << 1 \tag{187a}$$

$$\gamma^* \approx .1 \ \sec^{-1} \tag{187b}$$

$$J^* \approx 10^{11}L^{-4} \ cm^{-2}\sec^{-1} \tag{187c}$$

$$Q \approx -V_g \frac{\ln R}{LR_E} \approx 1 \tag{188a}$$

$$\ln R \approx -3 \tag{188b}$$

A computation of the group velocity for waves resonating at the equator with 2 MeV electrons gives

$$Q \approx .2/L \ \sec^{-1} \tag{189}$$

$$Q/P \approx 10^{11}L^{-5} \tag{190}$$

The actual value of Q/P is not very critical; it suffices to most purposes to say that Q/P is of order J^*.

Before proceeding to detailed solutions of the above differential equations, one should examine the behavior of the solutions near equilibrium.

122

Let

$$x \equiv (J - J_0)/J_0 \tag{191}$$

$$y \equiv (\lambda - \lambda_0)/\lambda_0 \tag{192}$$

The differential equations reduce to

$$\frac{dy}{dx} \equiv y' = -\frac{PJ_0}{\lambda_0} - \frac{Q}{\lambda_0} \frac{y}{y+yx+x} = -C_1 + C_2 \frac{y}{y+yx+x} \tag{193}$$

(Note that the actual cases to be solved have $C_2 \gg C_1 \gg 1$.)

The loci of constant slope $y' = A$ are the curves

$$y_A = x/[\frac{C_2 - C_1 - A}{C_1 + A} - x] \tag{194}$$

In Figures 33 - 39 some solutions are plotted for various values of C_1 and C_2, along with the loci of constant slope (the loci of constant slope are labeled with the angular slope in degrees).

If a trajectory $y(x)$ passes through the origin its slope must be equal to the limit of y/x, or

$$\frac{dy_A}{dx} = A \sim \frac{C_1 + A}{C_2 - C_1 - A} \tag{195}$$

$$A = \frac{C_2 - C_1}{2} \pm [(\frac{C_2 - C_1 - 1}{2})^2 - C_1]^{1/2} \tag{196}$$

Eq. (196) is complex for

$$C_2 < (\sqrt{C_1} + 1)^2 \tag{197}$$

which leads to periodic solutions that spiral forever about the origin x-y-0. Figures 33, 34, and 37 show examples of periodic solutions. These solutions are not likely in the realistic situations of interest here. When C_2 increases sufficiently A becomes real, with two values

123
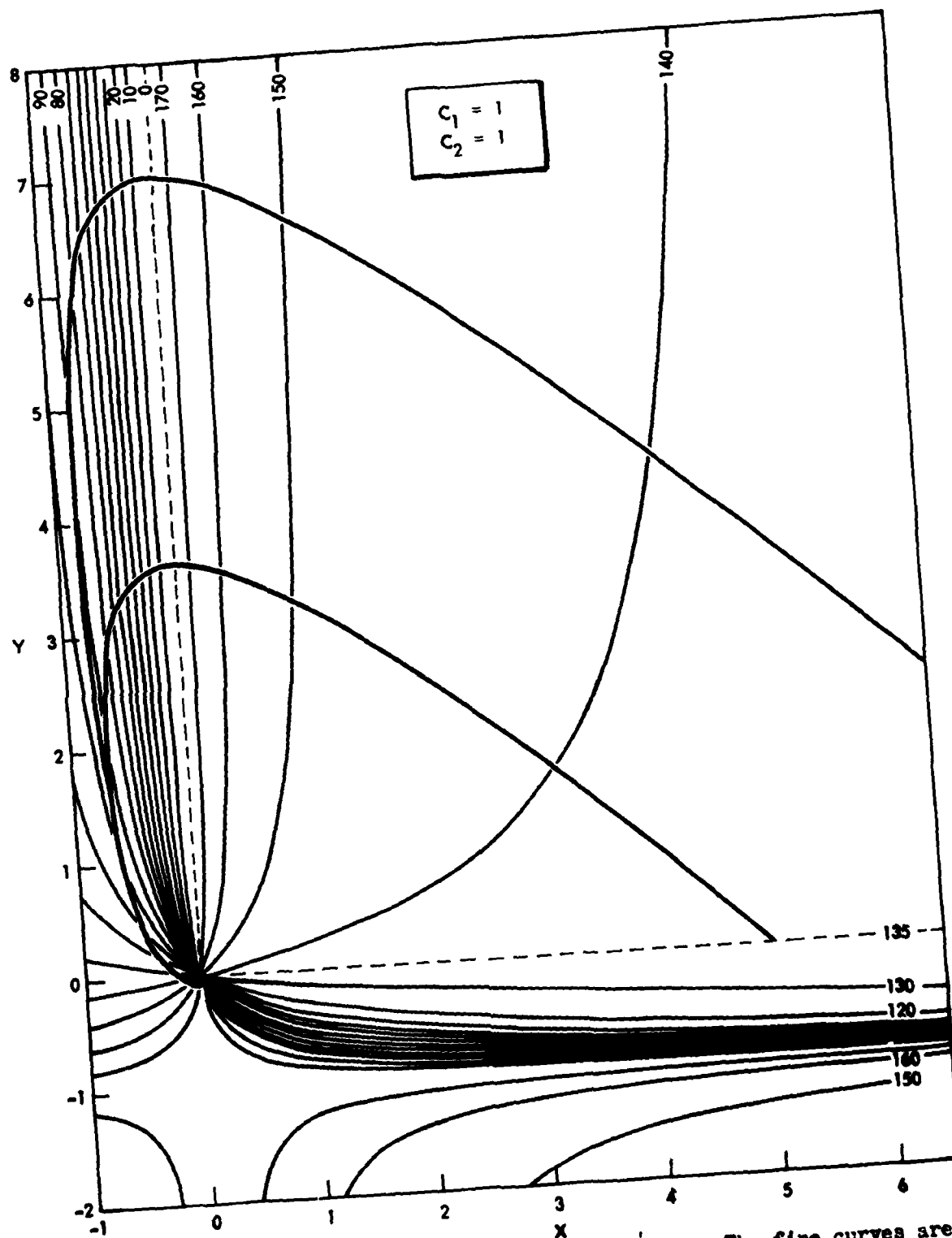
Figure 33. Flux vs. diffusion rate trajectories. The fine curves are the loci of constant slope, labelled with the slope in degrees.

124
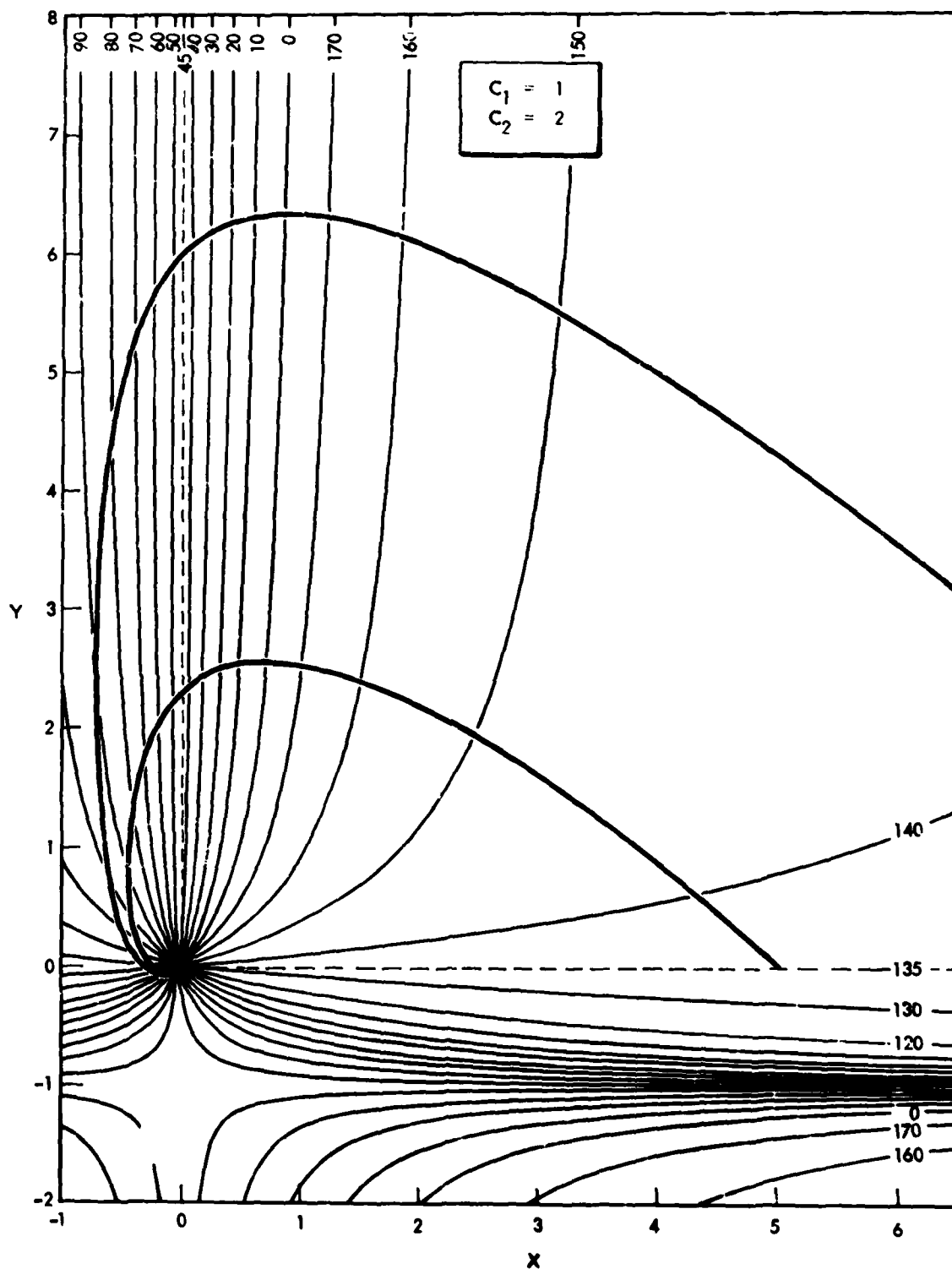
Figure 34. Flux vs. diffusion rate trajectories.
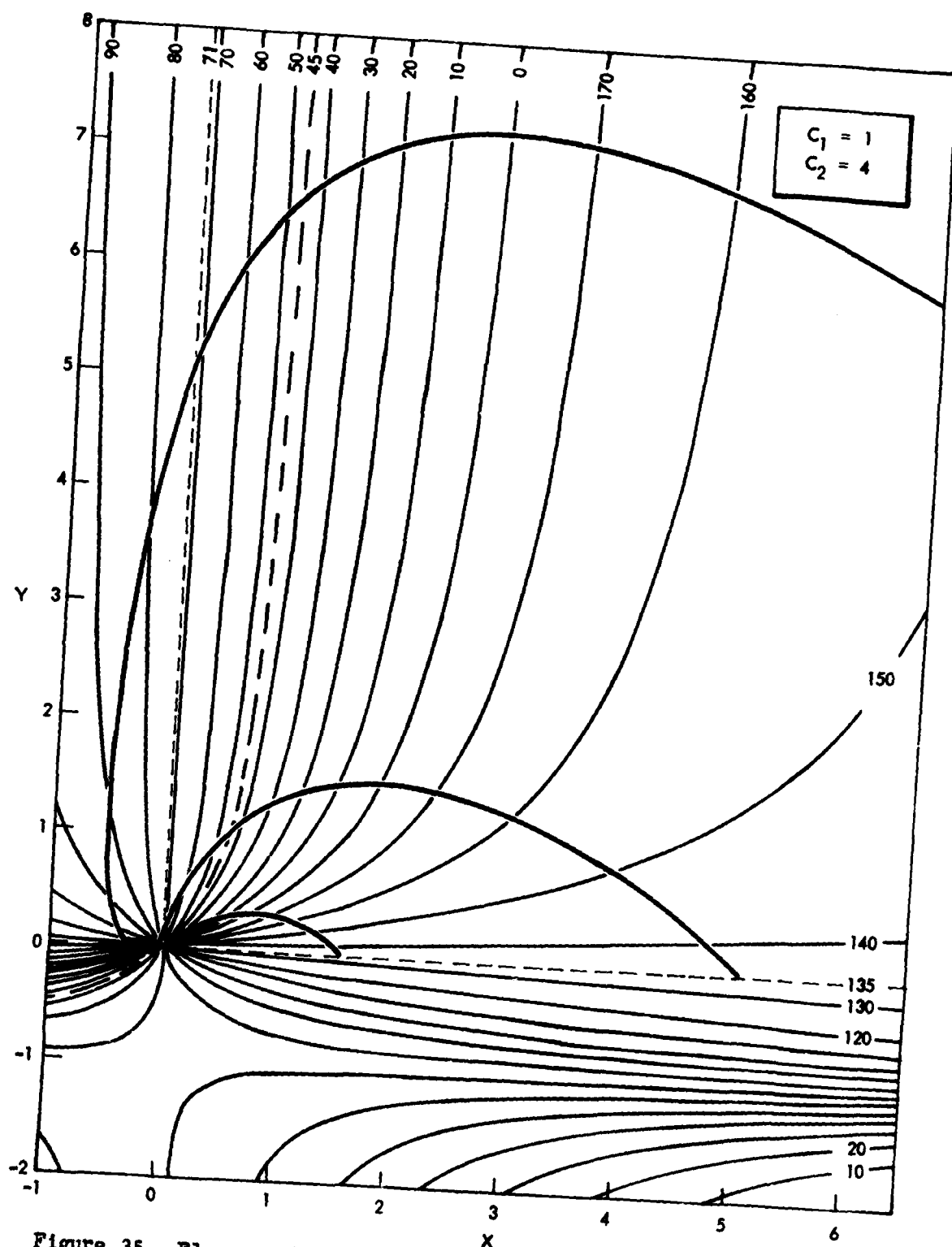
Figure 35. Flux vs. diffusion rate trajectories.

126
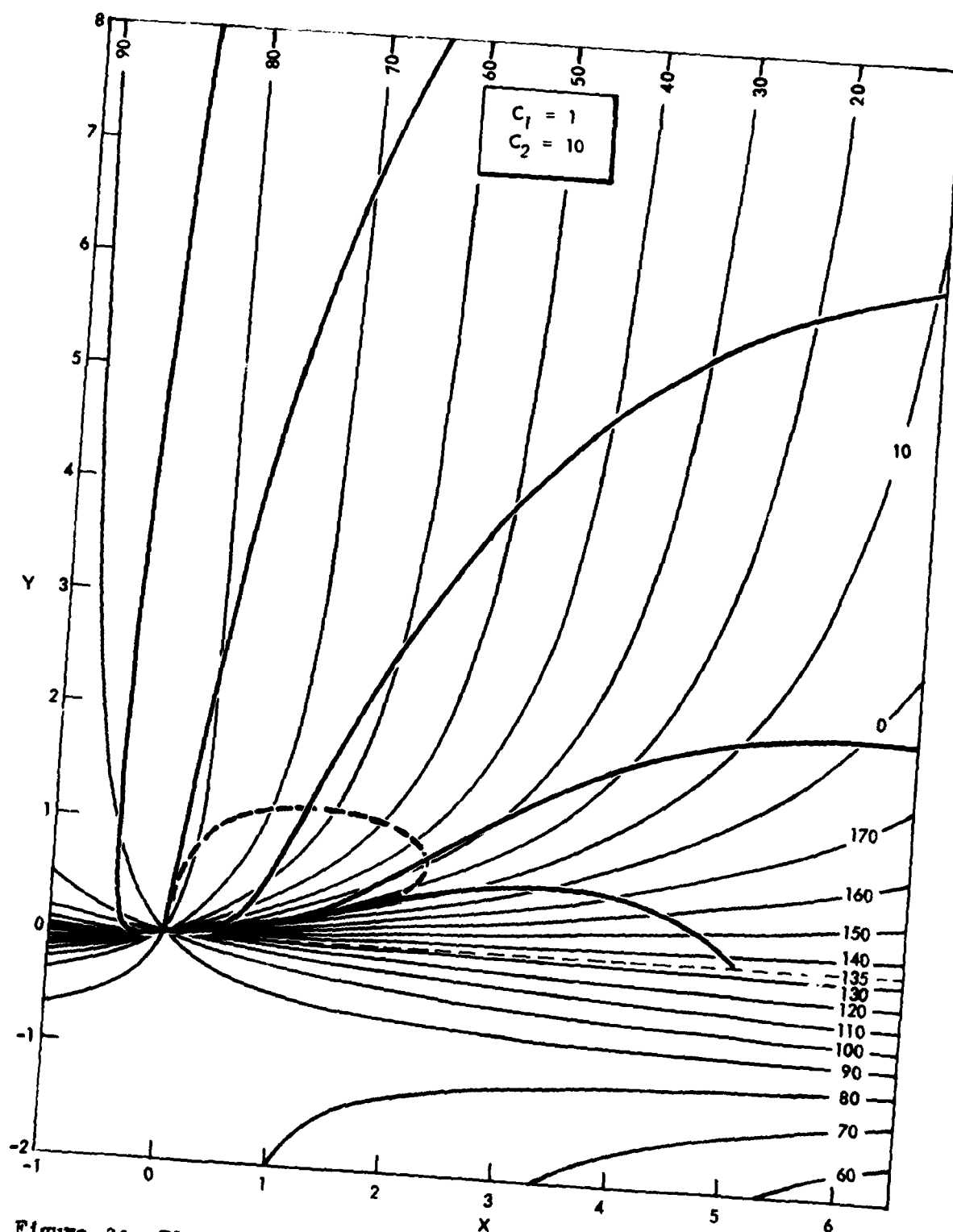
Figure 36. Flux vs. diffusion rate trajectories. The dashed curve is the locus of inflection points.
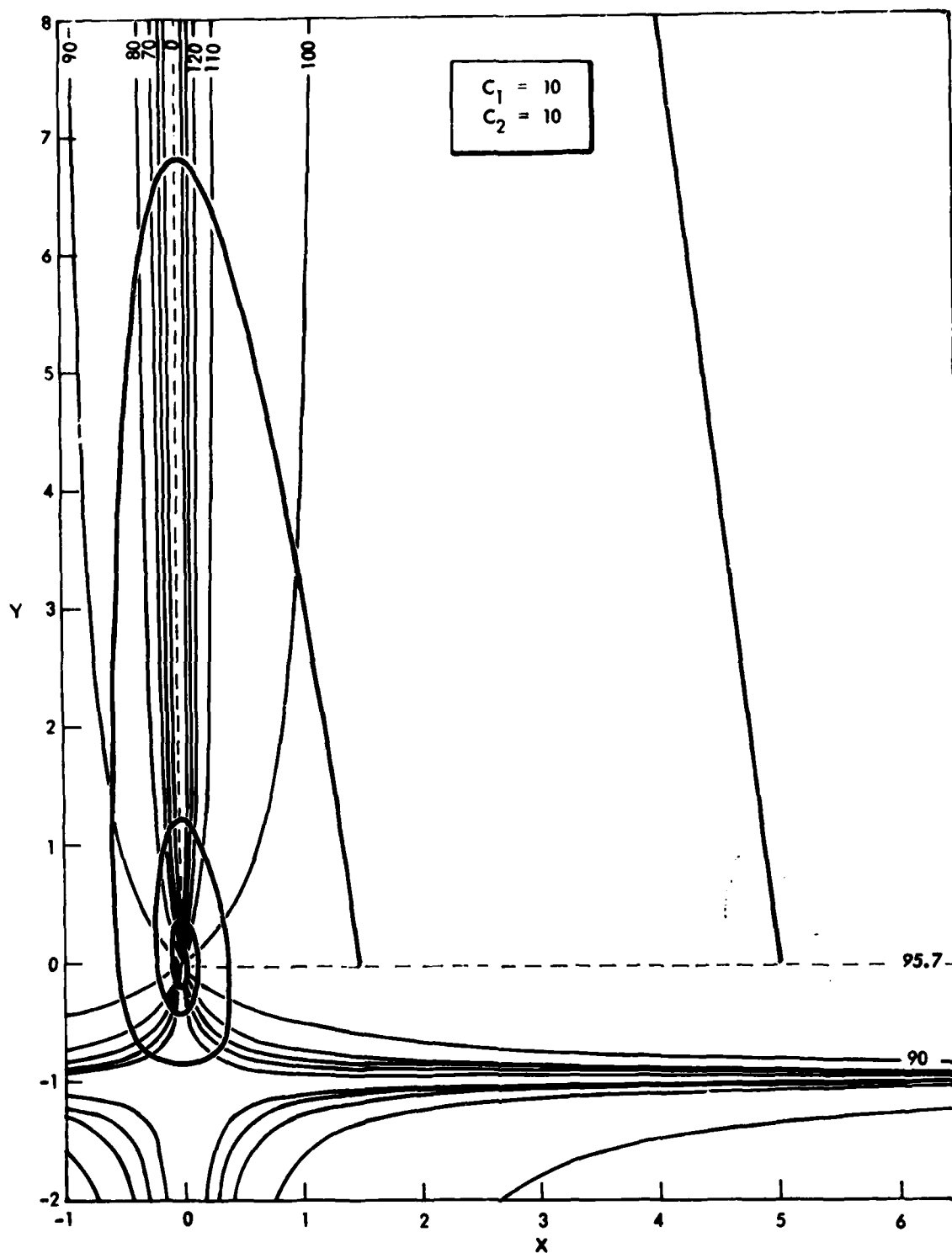
Figure 37. Flux vs. diffusion rate trajectories.

128
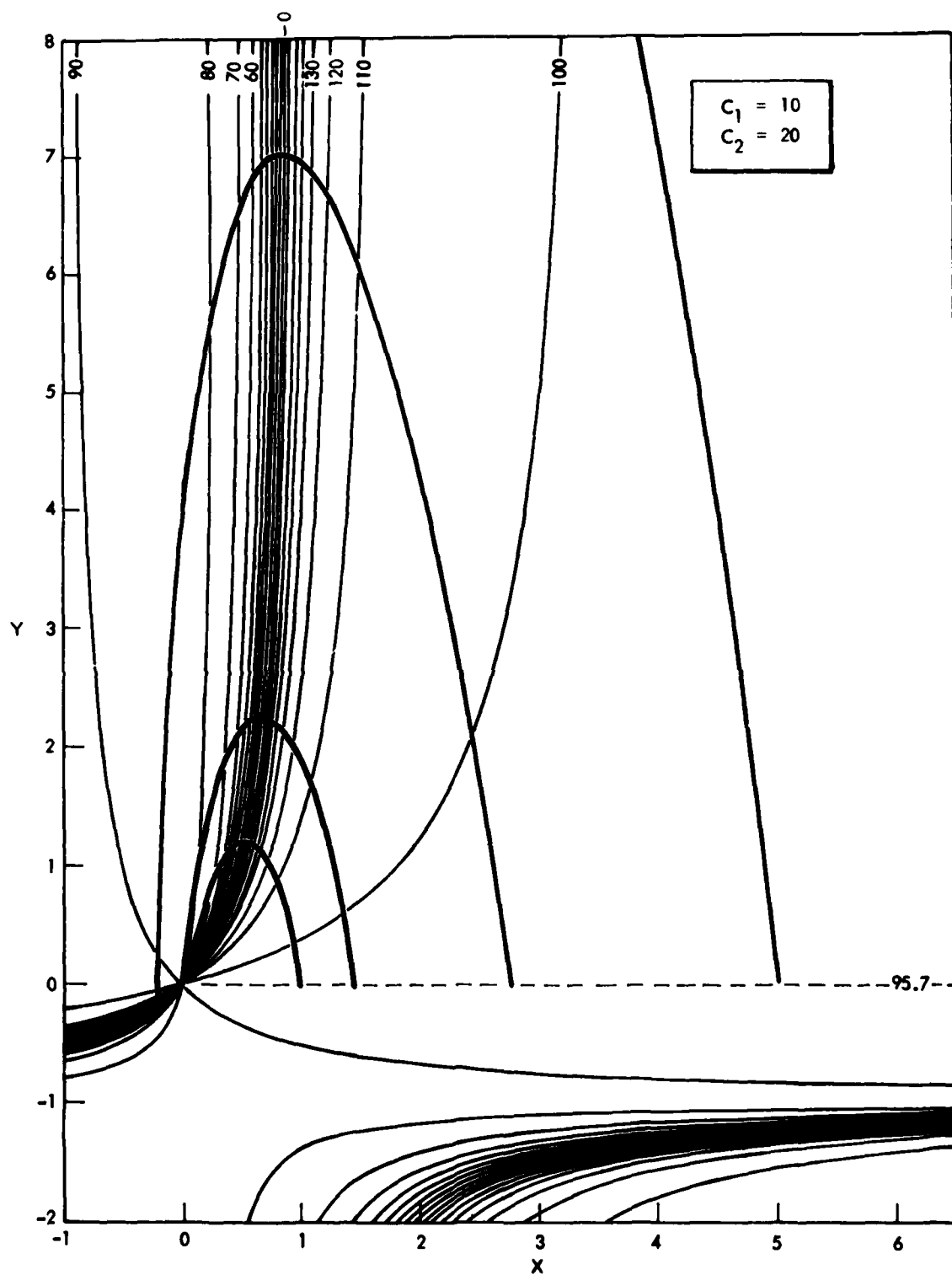
Figure 38. Flux vs. diffusion rate trajectories.
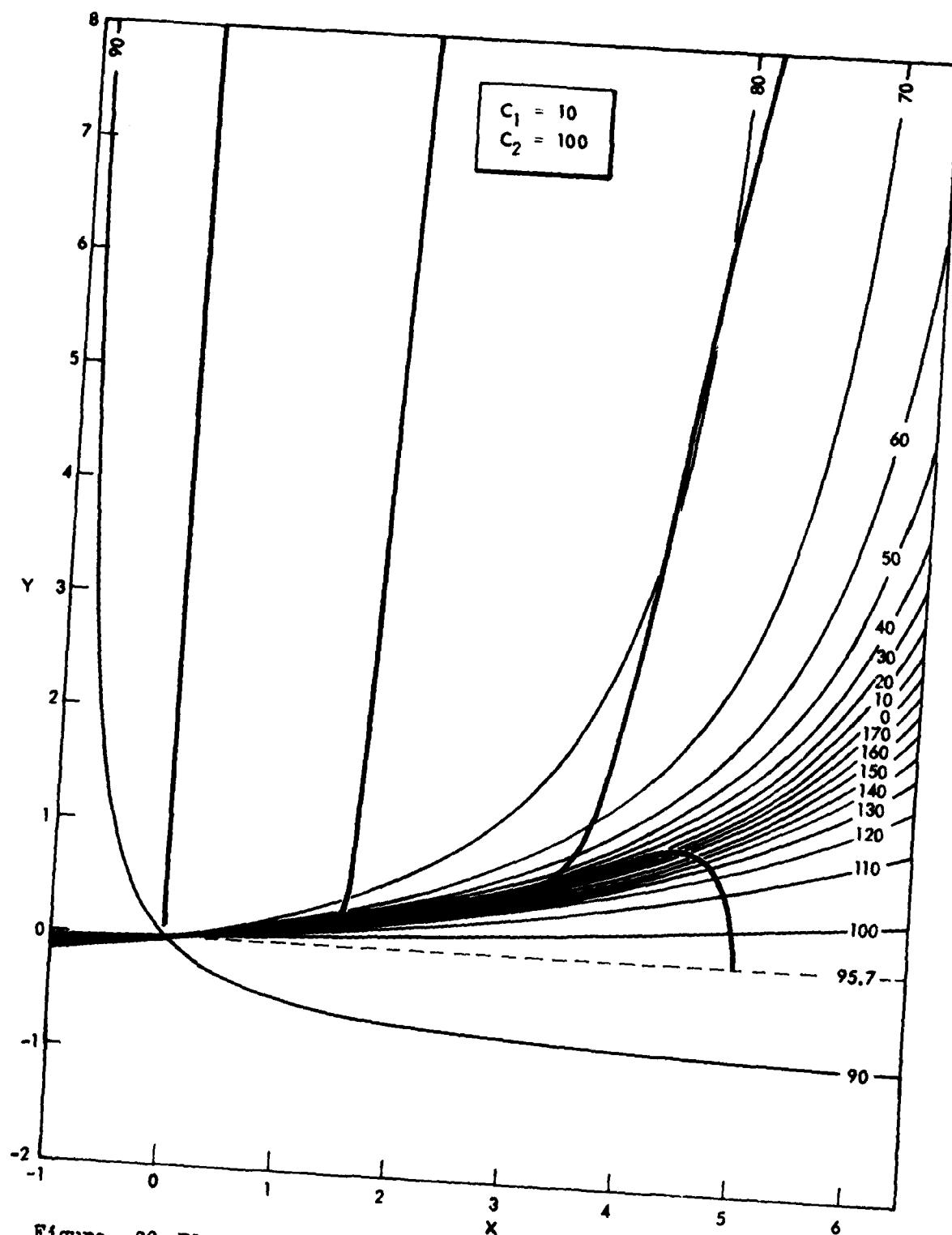
Figure 39. Flux vs. diffusion rate trajectories.

130

$$A_1 \approx C_2 - C_1 - 1 \tag{198a}$$

$$A_2 \approx \frac{C_1}{C_2 - C_1 - 1} \tag{198b}$$

The larger slope A_1 is only a limit case (the near vertical curve in Figure 30 is an example); the majority of solutions enter the origin with a slope near A_2. There are also interesting classes of trajectories to the left of the limit curve that overshoot the origin and approach from the left side $(J < Jo, \lambda < \lambda_o)$.

Note, too, that there is an inflection point wherever

$$-\frac{dy_A}{dx} = A = [C_2 - C_1 - A] / [C_2 - C_1 - A - x(C_1 + A)]^2 \tag{199}$$

The locus of inflection points is plotted in Figure 36 as a dashed line. The inflection points on Figure 39, however, lie so near the $A=0$ curve that most trajectories turn toward the zero slope curve and follow it closely for the major part of their descent. These are the trajectories of primary interest in the present context.

Eqs. (182) and (186), with their widely dissimilar characteristic time scales, constitute a pair of "stiff" differential equations. An excursion from equilibrium quickly causes the growth of waves within several wave growth periods; the wave-particle system then subsides back toward equilibrium at a rate determined by diffusion. The second part of the J,λ trajectory is the only one that concerns us here. But, from the preceding discussion we deduce that, if P is very small, the decay follows very closely the zero-slope curve:

$$\frac{d\ln\lambda}{d\ln J} = 0 = \frac{PJ^2\lambda - (1+\lambda\tau_s)[Q(\lambda-\lambda_o)+PS_o]J}{-\lambda^2 + S_o(1+\lambda\tau_s)\lambda} \tag{200}$$

or

$$J\lambda \approx (1+\lambda\tau_s)[\frac{Q}{P}(\lambda-\lambda_o)+S_o] \tag{201}$$

One may substitute J* for Q/P, though the appropriate constant may not be exactly identical with the Kennel and Petschek limit. Finally, one has, for λ as a function of J

$$\lambda(J) \simeq -\frac{1}{2\tau_s}(1-\frac{J}{J^*})+[\frac{1}{4\tau_s}(1+\frac{J}{J^*})^2+\frac{\lambda_o}{\tau_s}(1-\frac{Jo}{J^*})]^{1/2} \tag{202}$$

For small J:

$$\lambda(J) \sim \lambda_o\frac{J^*-Jo}{J^*-J}, \quad J << J^* \tag{203}$$

Near J*:

$$\lambda(J) \sim [\frac{\lambda}{\tau_s}(1-\frac{Jo}{J^*})]^{1/2}, \quad J \approx J^* \tag{204}$$

For large J

$$\lambda(J) \sim \frac{1}{\tau_s}(\frac{J}{J^*}-1), \quad J >> J^* \tag{205}$$

Consider now the extreme cases of strong and weak diffusion. In weak diffusion, where $J << J^*$, and $\lambda << 1/\tau_s$, Eq. (203) predicts exponential decay at a rate only slightly different from the natural diffusion rate λ_o. The strong diffusion case is described by Eq. (205), which gives

$$J(t) \sim J^*+(Jo-J^*)\exp(-t/\tau_s) \tag{206}$$

The flux thus decays at a nearly exponential rate until it reaches the saturation level, whereupon there is an abrupt transition to weak diffusion at a rate that quickly approaches λ_o.

Eq. (202) is plotted in Figure 40 for several values of the parameters. The transition to strong diffusion as J is increased is very striking. For values of J less than J* the natural, or parasitic, diffusion rate can always be used with high accuracy. For fluxes slightly greater than J* the diffusion quickly reaches the strong diffusion rate. However, at J* the diffusion rate assumes an intermediate value. This has important consequences that will be discussed below. It also seems to imply that Q/P, which is usually slightly less than J*, is an important parameter itself.

Using Eq. (202) it is a simple matter to integrate Eq.(182) to obtain the time history of the flux (it is not a simple matter to directly integrate the pair of differential equations, otherwise much of the above discussion would

132
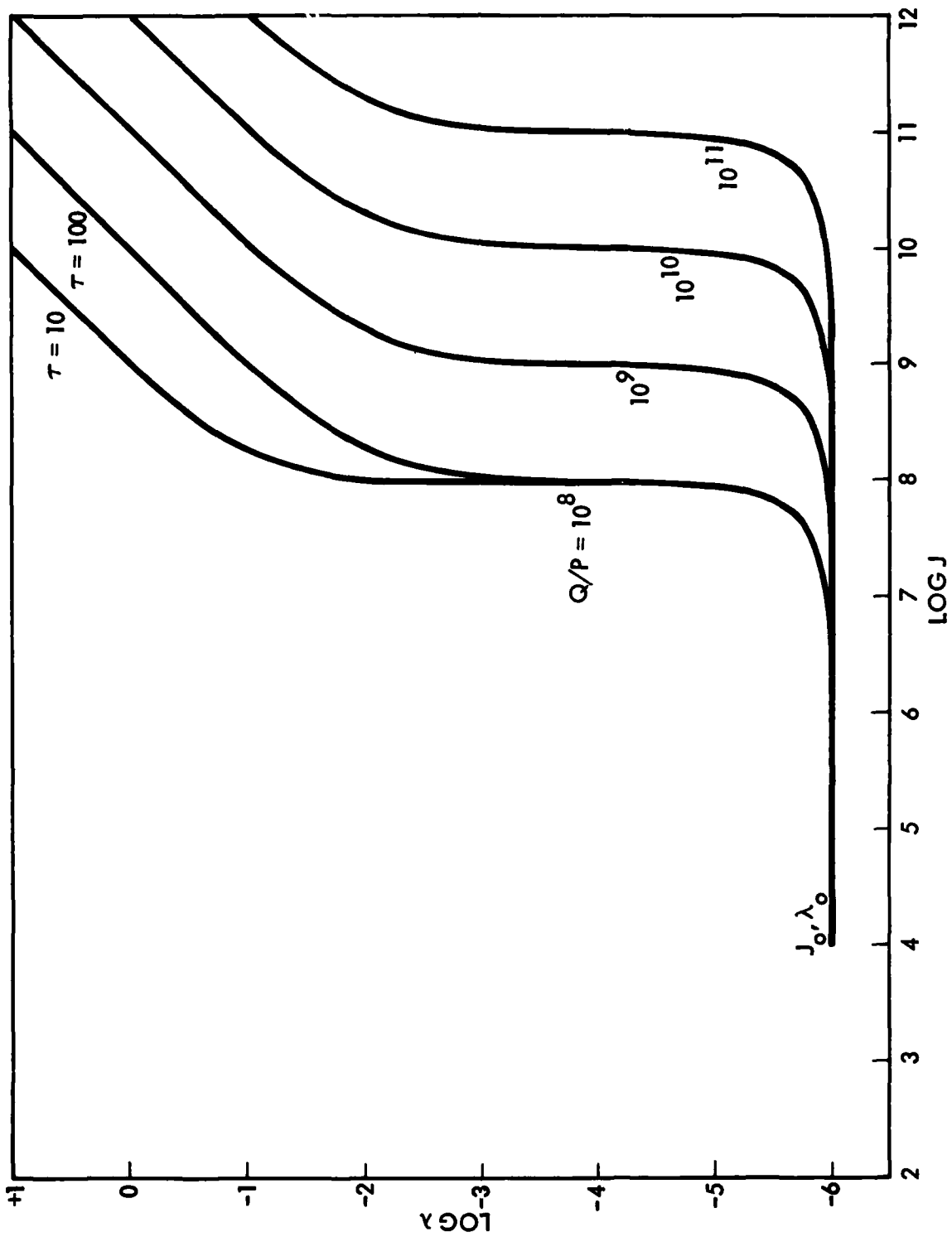
Figure 40. The loci of zero slope for several combinations of parameters. The equilibrium point is at $J_o = 10^4$ cm^{-2}sec^{-1}, $\lambda_o = 10^{-6}$ sec^{-1}.

133

have been unnecessary). Figures 41 and 42 show several solutions for $J(t)$; the two figures are identical but for their different time scales. The flux does decay at nearly the strong diffusion rate until it reaches $J*$; it thereupon decays at the natural rate. So the use of Eqs. (182) and (202), applied to the electron fluxes in Specter, leads naturally to a saturation value which is difficult to exceed for long periods.

3. ATTAINABLE SATURATION LEVELS

The saturation flux, $J*$, is not an absolute limit that can never be exceeded. If new electrons are injected at a high enough rate, a flux much larger than $J*$ can be sustained as long as the injection source. This is in marked contrast with the former Specter saturation model where an absolute limit was assumed. The values used for $J*$ are based on the best available data, which, in some cases, are good only to within an order of magnitude.

To inject electrons up to a level $J \lesssim J*$ it is only necessary to overcome the natural diffusion rate, which, for MeV electrons, is of the order $\lambda_o \approx 10^{-6} \sec^{-1}$. The time scale of artificial injection events is always less than λ_o but usually somewhat greater than the strong diffusion decay rate, $1/\tau_s$. For τ_s Schulz (Ref. 4) finds values

$$\tau_s \approx .04 \ L^4 / \frac{V}{C} \approx .04 \ L^4 \tag{207}$$

The flux from a series of isolated events would be expected to build up slowly until a flux near $J*$ is attained.

To maintain (or generate) a saturated flux, $J \gtrsim J*$, it is necessary to set up an intense electron source, S'; Eq. (182) then becomes

$$\frac{dJ}{dt} \approx - \frac{\lambda J}{1+\lambda\tau_s} + S_o + S \tag{208}$$

If the build up rate does not exceed the wave growth rate (of order .1 to 1 $\sec^{-1}$), the diffusion rate will continuously adjust to the values given by Eq. (202). Even if the wave growth rate is exceeded for a short time, the diffusion rate will quickly relax to those values when the injection rate is reduced, or when the sustainable flux, J', is reached. Eqs. (182) and (202) give for J':

134
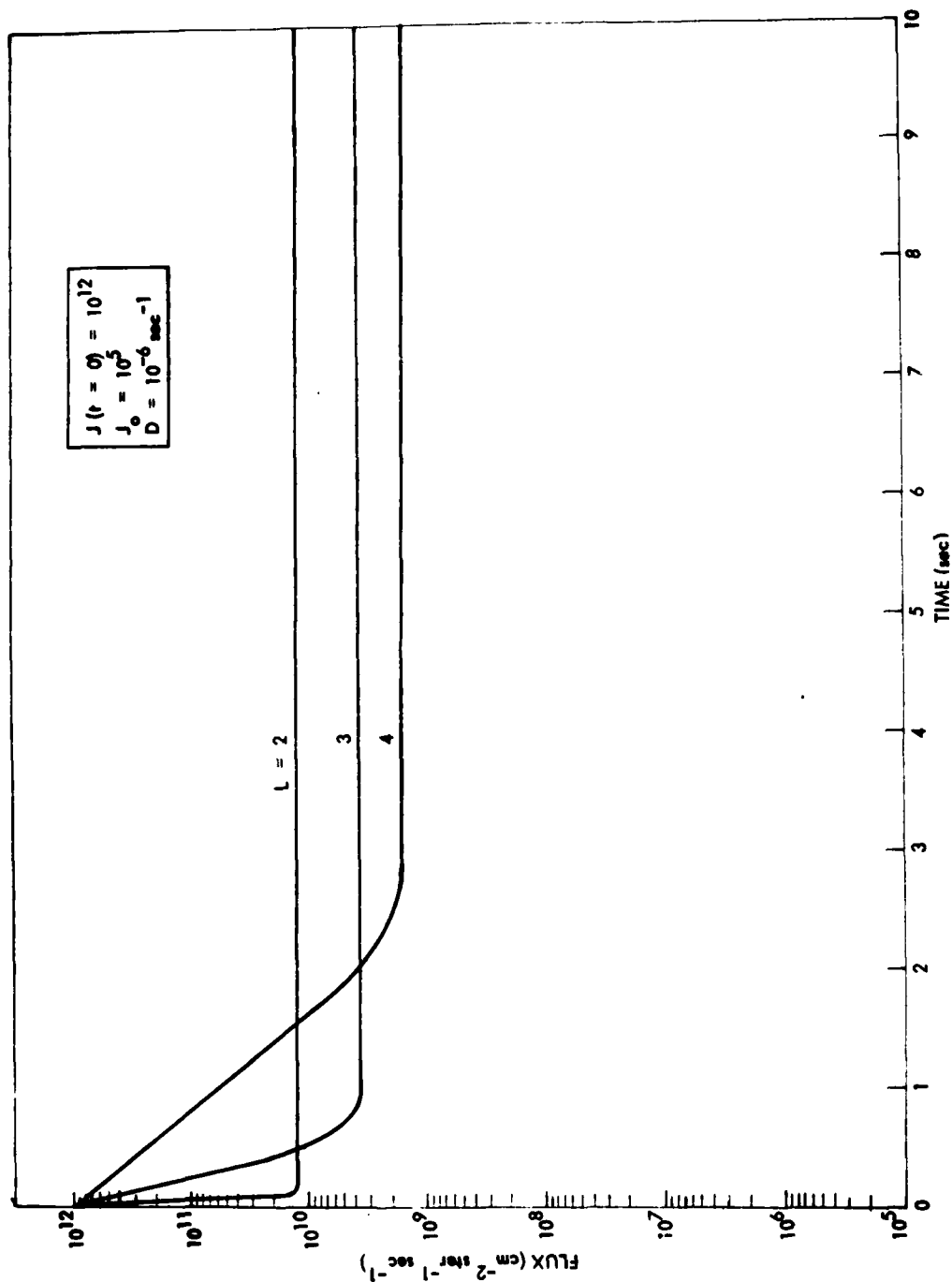
Figure 41. The early time decay, up to 10 sec. of a hypothetical radiation belt from an initial flux of 10^{12} cm^{-2} ster^{-1} sec^{-1}.

135
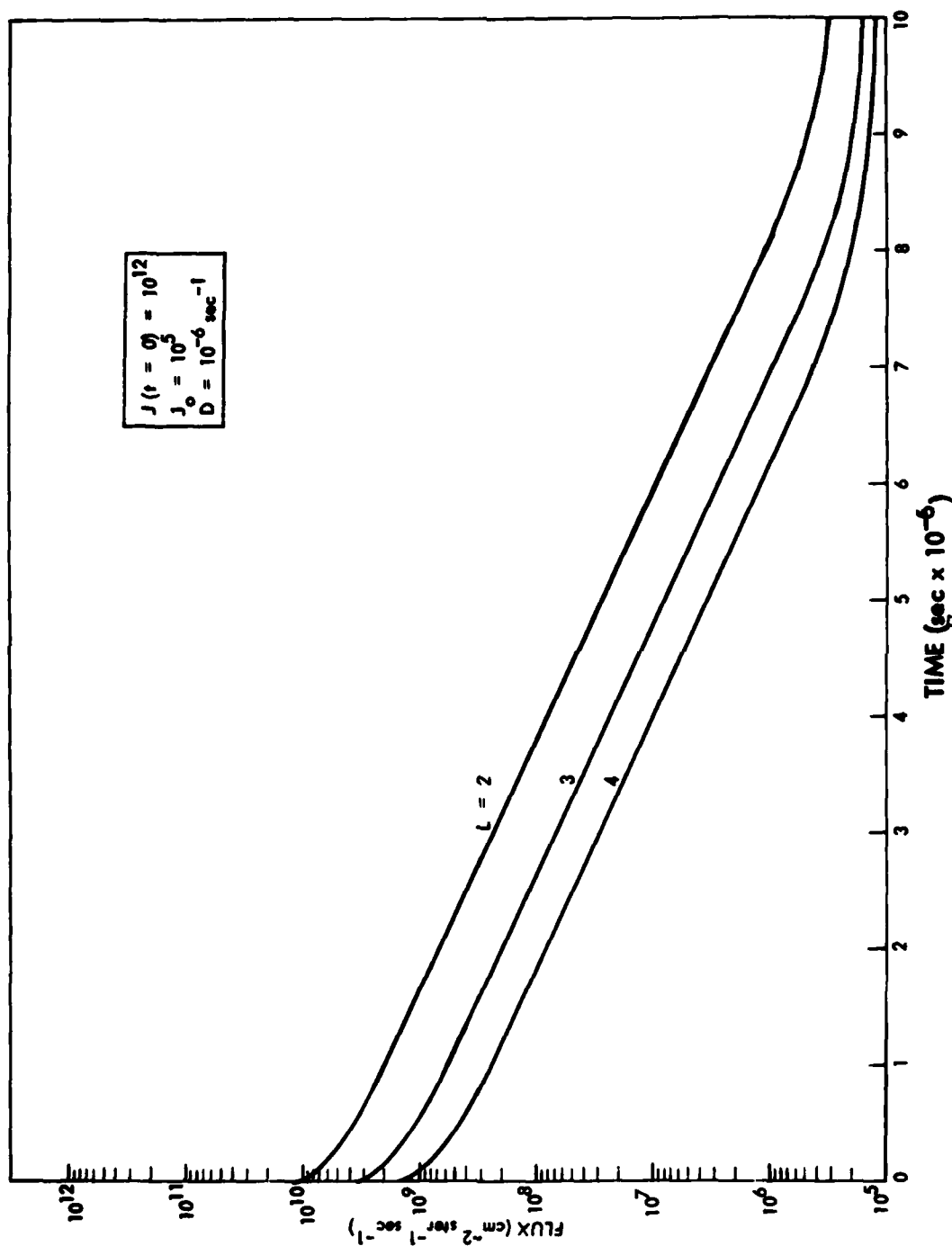
Figure 42. The late time decay, up to 10^7 sec., of an hypothetical radiation belt from an initial flux of 10^{12} cm^{-2} ster^{-1} sec^{-1}.

136

$$\frac{\lambda(J')J'}{1+\lambda(J')}\tau_s \approx S_o + S' \approx J^*(\lambda(J')-\lambda_o)+S_o \tag{209}$$

$$J' \approx S'[J^*+S'\tau_s]/[\lambda_o J^*+S'] \tag{210}$$

The source, S', is related to the electron injection rate. For isotropic injection

$$S' \approx \frac{dN}{dt}\,2/\int_o^{\pi/2}\tau_b \sin\alpha_o \cos\alpha_o\,d\alpha_o \approx 51.4\,\frac{dN}{dt}\,\frac{1}{L} \tag{211}$$

where N represents the total number of electrons trapped in a tube of unit cross sectional area at the equator, and α_o is the equatorial pitch angle. The injection rate is usually known in units of MT fission β yield per second. If W is the injection rate in MT per ΔL per second (assumed uniform in longitude), the relation to S' is

$$S' \approx 51.4\,W \times 6\times10^{26}\,\frac{1}{2\pi R_E^2 L} \approx 1.2\times10^{10}\,\frac{W}{L} \tag{212}$$

Properly W should contain the trapping efficiency, which is usually less than 10%. The sustainable flux is then

$$J' \quad W\,\frac{(J^*+4.7\times10^8 L^2 W)}{(W+8.3\times10^{-11}L^2\lambda_o J^*} \tag{213}$$

The time taken to reach J' is approximately $\tau' \approx J/\frac{dJ}{dt}$, evaluated at J'.

Some values are given in Table 2 for a case $L \approx 4$, $\lambda_o \approx 10^{-6}\text{sec}^{-1}$, $J^* \approx 5\times10^8\text{cm}^{-2}\text{sec}^{-1}$. It is evident from the table (also from Figure 40) that J' reaches a broad plateau near J^* long before τ' approaches τ_s. This is in marked contrast with the customary presumption that strong diffusion must prevail when J' is near J^*. The presumption of strong differences at J^* has led to the misleading conclusion that the saturation limit is unlikely ever to be reached (Ref 34). That deduction was based on a diffusion rate $\lambda \sim 1/\tau_s$, which corresponds in the example of Table 2 to injection rates $W \gtrsim 1\text{ MT }(\Delta L)^{-1}\text{sec}^{-1}$. But injection rates 4 to 5 orders of magnitude lower can give fluxes within 90% of the saturation value. Near-saturation <u>can</u> be attained with realistic injection rates as low as 10^{-5} MT $\text{sec}^{-1} \approx .04$ MT hr^{-1}. This corresponds to an actual fission yield $>.4$ MT hr^{-1}.

137

Table 2

Sustained Flux Levels Related to Injection Rate at $L = 4$

W (MT $\Delta L^{-1} \sec^{-1}$)	J' ($cm^{-2} \sec^{-1}$)	τ (sec)	$W \times \tau$ (MT ΔL^{-1})
10^{-9}	7.5×10^5	10^6	.01
10^{-8}	7.4×10^6	9.9×10^5	.099
10^{-7}	6.5×10^7	8.7×10^5	.87
10^{-6}	3.0×10^8	4.0×10^5	4.0
10^{-5}	4.7×10^8	6.0×10^4	6.0
10^{-4}	5.0×10^8	3.2×10	3.2
10^{-3}	5.1×10^8	500	5.0
10^{-2}	5.8×10^8	72	7.2
10^{-1}	1.25×10^9	17	17
1	4.0×10^9	11	110
10	7.6×10^{10}	10	10^3
10^2	7.5×10^{11}	10	10^4
10^3	7.5×10^{12}	10	10^5

4. INCORPORATION OF SATURATION EFFECTS IN SPECTER

There are two needs for a new saturatioan model in Specter. One is in the saturation model, where saturation is assumed to prevail for a specified duration. In that case one need only replace the former beta criterion by the new criterion, Eq. (213). The adjustable parameters now are W and the duration of the saturation event. These paraemters have readily apparent physical significance. It is even conceivable that W be allowed to vary with time, in which event J´ will adjust nearly instantaneously to the changes.

The other need for a saturation model is in the decay scheme, where the decay rates must be adjusted continuously when the flux approaches J*. One way this can be achieved is to carry an explicit integration of Eqs. (182) and (202) in the loss model. There are, however, simple approaches that give the same limiting behavior at weak and strong diffusion. The transition regime is not well enough understood that the Schulz model is to be preferred over all others. It is, though, a valuable guide to our understanding. The time behavior is actually represented quite well by the formula

$$J(t) \approx J(0)[1-C*]\exp(-t/\tau_s)+J(0)C*\exp(-t/\tau_L) \tag{214a}$$

$$C* \equiv [\text{constant}] \frac{J*}{J(0)+J*} \tag{214b}$$

$$\tau_L \equiv 1/\lambda_o \tag{215}$$

That this form of decay is a good representation in the limits is readily apparent from Figures 41 and 42. In fact, with [constant] $\approx$ 1, Eq. (214) is a very close approximation for all J > J*. Table 3 lists several comparisons for the case $J(0) \approx 10^{10}$, $J*=10^8$, $\tau_s=10$, $\tau_L=10^6$. At smaller fluxes the loss time, $\tau=J/\frac{dJ}{dt}$, approaches τ_L more quickly than in the explicit solutions; but either representation is adequate within the bounds of our ignorance of the actual physical processes.

The decay rates of Eq. (214) are incorporated in the revised Specter electron decay model. The coating changes are minor, and affect only one subroutine — the one used to compute less rates.

Table 3

The Decay of a Saturated Radiation Belt

τ(sec)

t(sec)	J $(cm^{-2}sec^{-1})$	from Eq.(182)	from Eq. (214)
0	10^{10}	10.09	10.10
20	1.43×10^9	10.66	10.75
40	2.71×10^8	14.91	15.86
60	1.14×10^8	46.27	83.11
80	9.24×10^7	278	7.59×10^4
100	8.96×10^7	1.99×10^3	1.05×10^5
120	8.92×10^7	1.44×10^4	1.09×10^5
150	8.92×10^7	2.27×10^5	1.09×10^5
200	8.91×10^7	9.78×10^5	1.09×10^5

INTERACTION REGIONS OF MULTIBURSTS

An investigation has been conducted to determine under what circumstances the simple superposition of injected fluxes due to multiple bursts may be applicable. Specifically, it calls for the boundaries in space and time that define,

i) the interaction region, wherein the detonations are not sufficiently close together to be considered as a single detonation but are sufficiently close together to affect each other's injection processes,

ii) the summing region, wherein the detonations are sufficiently close together in space and time to be considered as a single detonation; and

iii) the noninteracting region, wherein the electron injections are independent and unaffected by the additional detonations.

First, we will try to define regions (i) and (ii). Region (iii) will then be specified as the remaining space and time conditions outside of (i) and (iii).

At the outset, it should be emphasized that a single high-yield burst greatly disturbes the atmosphere-ionosphere-magnetosphere system: the atmospheric heave increar   ¬eutral density in the upper atmosphere by several orders of magnitude   v hundreds of seconds; the heated ionospheric plasma fills the loca   ·tic tube of force, creating an anomously high plasma density in the tube that persists for hours; shock waves are produced that travel several times around the earth; the entire magnetosphere oscillates, producing a wide-band of micropulsations throughout the world; and even the high-energy protons (55 MeV) in the radiation belt are redistributed (see e.g. Ref. 2). In the strictest sense, therefore, the interaction region should include almost all the space-time scenarios envisaged for a nuclear

exchange. In this study we will attempt to include only first-order
effects.

1.   INTERACTION REGION

a.   Expansion of Collision-Dominated Region.

For an explosion below the exosphere, in the collision-dominated region, the
expansion of the nuclear debris will be stopped within a sphere that contains
a mass of air approximately equal to the mass of the debris. Owing to the
buoyancy of the fireball, the debris will also be accelerated upward; if the
fireball radius is at least comparable with the scale height of the atmosphere,
the fireball will undergo a ballistic rise which may carry the debris beyond
the exosphere. However, for detonations away from the South Atlantic anomaly,
very few fission fragments are expected to reach altitudes above about 1500 km,
where the electron trapping efficiency becomes finite. Therefore, the flux
of trapped electrons resulting from the direct injection process should be
negligible. Nevertheless, the Teak and Orange tests did establish radiation
belts. It is believed that these belts resulted from pitch-angle diffusion
of the electrons, due to a plasma instability, after the electrons emitted
by the fission fragments penetrated the residual atmosphere. Since, at the
present time, the Specter codes compute trapped-electron fluxes due to the
direct injection process alone, explosions below an altitude of 200 km are not
included in this study.

In a multiburst situation, however, the altitude of the exosphere is dependent
on the timing of the nuclear bursts as well as the magnitude of the attendant
energy deposition in the atmosphere. Data on the increase in the density of
the atmosphere at high altitudes, in time and space, due to Standard Spartan
bursts at altitudes of 175, 200, 225, and 250 km have been generated by NRL
MRHYDE code. The increase in the altitude of the region where collisions
become important, as a function of the time after a 200-km Spartan burst,
is shown in Figure 43. Note that the altitude of the collision-dominated
region, under the burst, increases substantially, and it remains high for
several hundred seconds. The collision-dominated region is assumed to be at alti-
tudes below the 200-km density contour. The enhanced-density region is

142
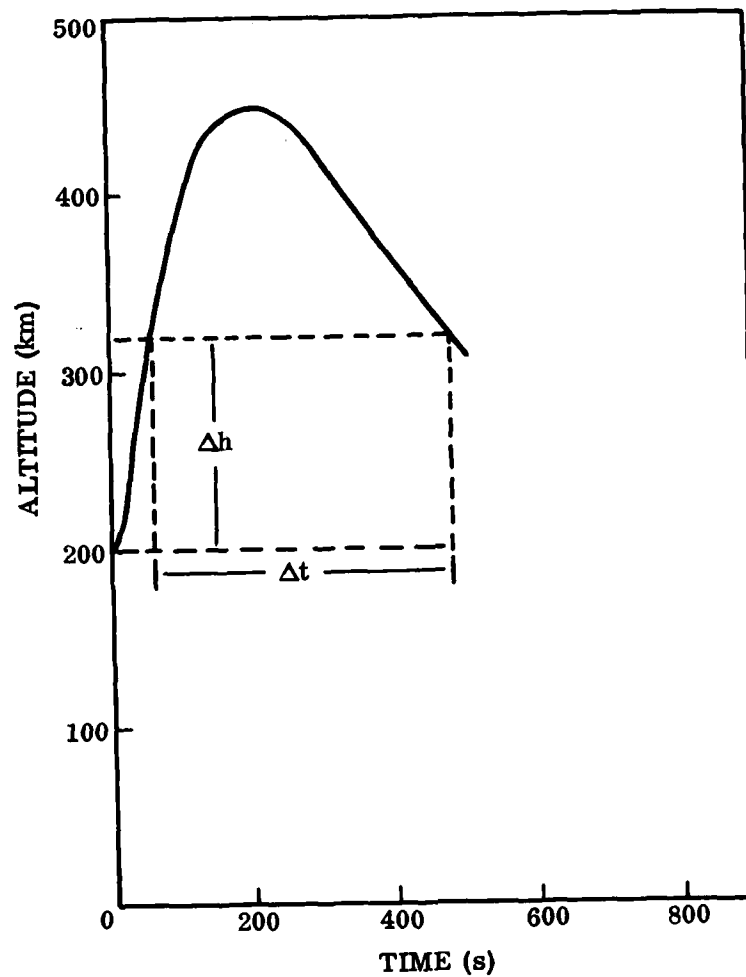
Figure 43. Altitude of 200-km atmospheric-density contour versus
time after Standard-Spartan burst.

143

bell-shaped about a vertical axis through the burst. Since the motion of the debris resulting from an explosion near the exosphere is not known sufficiently well to warrant a detailed specification of the collision-dominated region, the region will be described by simplified "square" functions. Hence, the increased height of the region will be taken to be Δh, half the maximum altitude reached by the 200-km density contour shown in Figure 43; the diameter of the region will be taken to be 2R, the diameter of the 200-km density surface at the altitude Δh; and the time interval of the enhanced density will be taken to be Δt, the time during which the altitude of the contour shown in Figure 43 exceeds Δh.

The data for the Standard Spartan bursts at different altitudes reveal that the intervals Δt are quite similar, beginning at about 60 sec and ending at about 480 sec. However, the heights Δh decrease, and the diameters 2R increase, as the burst altitude increases. These variations are shown in Figure 44.

For bursts of different yields, but at a given altitude, the following reasonable assumptions will be made:

i) The enhanced-density volumes, $R^2\Delta h$, are proportional to the yield. Hence,

$$\frac{R^2\Delta h}{R_s^2 \Delta h_s} = \frac{Y}{Y_s} \tag{216}$$

where Y_s is the Standard Spartan yield and R_s and Δh_s are the dimensions of the enhanced-density region given in Figure 44.

ii) The shape of the perturbation, $\Delta h/R$, remains constant; i.e., the atmospheric expansion pattern for a fixed illumination geometry remains the same. Hence,

$$\frac{\Delta h}{R} = \frac{\Delta h_s}{R_s} \tag{217}$$

144
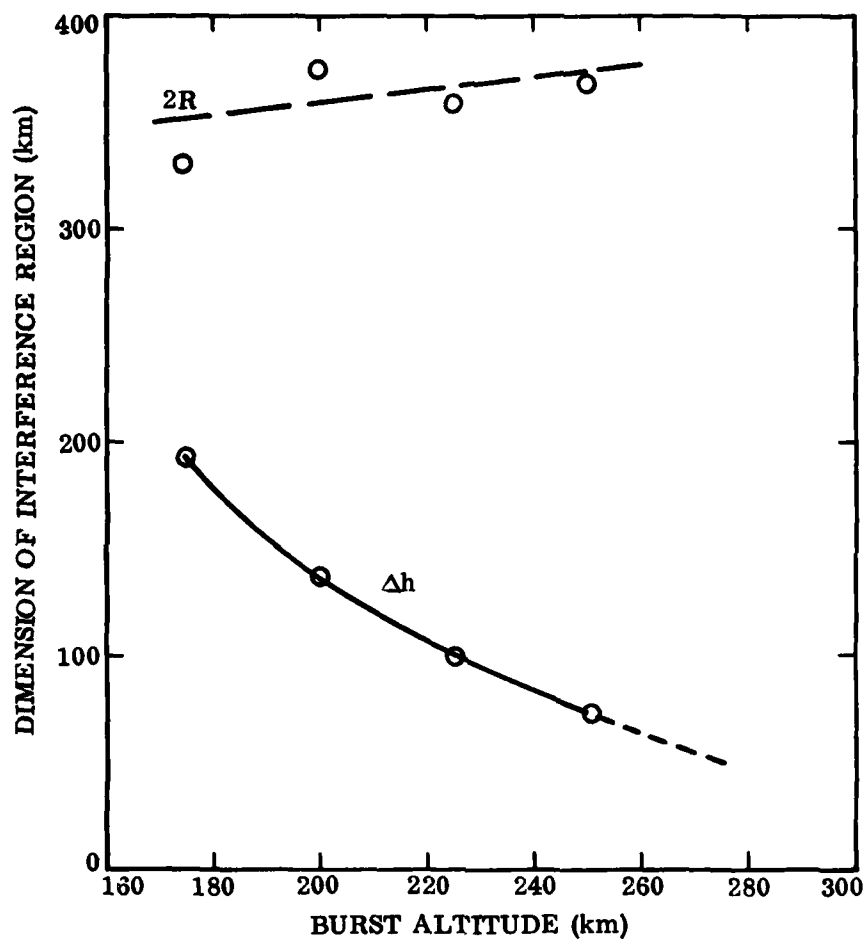
Figure 44. Effective height-increase, Δh, and diameter, 2R, of collision-dominated region vs. height of Standard-Spartan burst.

The above equations give,

$$\Delta h = \Delta h_s \left(\frac{Y}{Y_s}\right)^{1/3} \qquad (218)$$

and

$$R = R_s \left(\frac{Y}{Y_s}\right)^{1/3} \qquad (219)$$

For a burst at the altitude H* of yield equal to 5 MT, for example, Δh = 110 km and R = 195 km. If a second burst is detonated in this region at times after the first burst in the range $60 \leq \Delta t \leq 480$ sec, the injection efficiency of the second burst will be impaired.

If the disturbance produced by a second burst overlaps that produced by the first, an enhancement of the altitude of the overlapping region should occur. This situation is depicted in Figure 45. The heights and yields of the two bursts are H_1^*, Y_1 and H_2^*, Y_2; the parameters of the enhanced-density region produced by each burst alone are denoted by the subscripts, 1 and 2. Δh_3 is the height of the enhanced-density region over the overlapping areas.

The altitude Δh_3 can be estimated as follows. From i)

$$R_n^2 \Delta h_n = k(H_n^*) Y_n, \quad n = 1,2 \qquad (220)$$

where, as indicated, the proportionality constant k is a function of the burst altitude H_n^*. The average value of k for the two detonations is, therefore,

$$k_{ave} = \frac{1}{2} \left(\frac{R_1^2 \Delta h_1}{Y_1} + \frac{R_2^2 \Delta h_2}{Y_2}\right) \qquad (221)$$

146
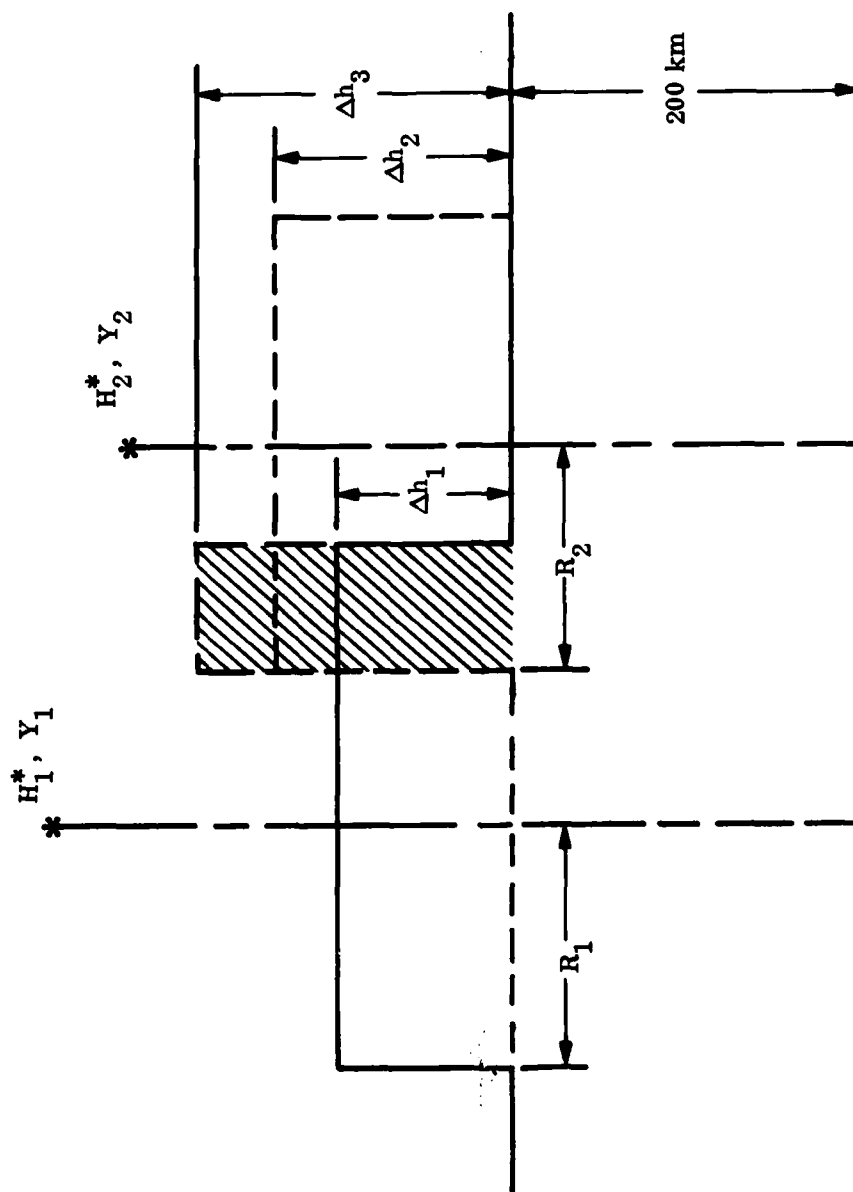
Figure 45. Illustration of increase in height of overlapping regions of enhanced-atmospheric density produced by two bursts.

Thus, for the combined bursts,

$$R_3^2 \Delta h_3 = k_{ave}(Y_1 + Y_2) \qquad (222)$$

Similarly, from ii),

$$\frac{\Delta h_3}{R_3} = \frac{1}{2} \left(\frac{\Delta h_1}{R_1} + \frac{\Delta h_2}{R_2} \right) \qquad (223)$$

Using these equations, a solution for Δh_3 can be expressed as,

$$\Delta h_s = \frac{1}{2} (f_{12} + f_{21})^{1/3} (Y_1 + Y_2)^{1/3} \qquad (224)$$

where,

$$f_{12} = \frac{\Delta h_1}{Y_1} \left(\Delta h_1 + \frac{R_1}{R_2} \Delta h_2 \right)^2 \qquad (225)$$

and f_{21} is obtained from (225) by interchanging the subscripts 1 and 2.

As an example, for $Y_1 = 5$ MT and $H_1^* = 218$ km, $\Delta h_1 = 110$ km and $R_1 = 195$ km; for $Y_2 = 10$ MT and $H_2^* = 240$ km, $\Delta h_2 = 115$ km and $R_2 = 251$ km. Hence, if these detonations are separated in time by less than 480 sec, then in the overlapping spatial region, $\Delta h_3 = 145$ km.

b. Region of Longitudinally-Bunched Electrons

An impairment of the injection efficiency also occurs if a weapon is exploded in the region of a drifting beta tube; i.e., in that region where the electrons injected by a previous burst are still highly bunched in longitude. Such a region contains an eastward electric field, which tends to redistribute the electrons to higher L values, and magnetic-field-aligned currents, which tend to neutralize excess charges. A burst in that

148

region modifies both the eastward-electric field and the current patterns, thereby altering the redistribution of the electrons. Furthermore, the existing electric field and currents modify the cross-L motion of the debris tube. The electron loss rate due to wave-particle interactions is also enhanced because of the increased electron flux.

Initially, the azimuthal sector of the beta tube is equal to the width of the debris tube, $\Delta\phi$, used in the injection model. At later times, owing to the energy spread of the electrons, the width of the sector increases as the electrons drift toward the east. We will regard (i) the center of the bunched electrons to be at the magnetic longitude, ϕ_o, where half of the injected electrons are at $\phi \geq \phi_o$, (ii) the western edge of the bunch to be at ϕ_1, where three-fourths of the injected electrons are at $\phi \geq \phi_1$, and (iii) the eastern edge of the bunch to be at ϕ_2, where one-fourth of the injected electrons are at $\phi \geq \phi_2$. Hence, one-half of the electrons will be within the magnetic longitudes ϕ_1 and ϕ_2. If $N(L,t_L)\Delta L$ is the total number of electrons injected at L in the interval ΔL and at the time t_L, then the number of electrons that drift past ϕ_i at the time t is

$$N(\phi \geq \phi_i, L, t)\Delta L = N(L,t_L)\Delta L \int_{w_1}^{\infty} G(w)dw \qquad (226)$$

where $G(w)$ is the energy spectrum of the redistributed electrons at the eastern edge of the debris tube. It is given by the sum

$$G(w) = \sum_j \frac{k_j \exp(-w/w_j)}{w_j} \qquad (227)$$

The lower limit in (226) is the energy of an electron that drifts eastward to ϕ_1 at the time t; i.e., it satisfies the equation

$$\phi_1 - \phi^* = \dot{\phi}_D(w_1,L)(t-t_L) \qquad (228)$$

149

where ϕ^* is the longitude of the burst, and $\dot{\phi}_D(w_1,L)$ is the mean azimuthal drift velocity at L of an electron of energy w_1. The integration in (227) is just $\sum_j k_j \exp(-w_1/w_j)$. Hence, (226) can be solved for w_1 and w_2 corresponding to ratios $N(\phi > \phi_1, L, t)/N(L, t_L)$ of 3/4 and 1/4 respectively. The interaction region can then be specified as,

$$\phi_2 - \phi_1, \quad \Delta L, \quad t - t_L \tag{229}$$

where

$$\phi_1 = \phi^* + \frac{\Delta\phi}{2} + \dot{\phi}_D(w_1,L)(t-t_L) \tag{230}$$

$$\phi_2 = \phi^* + \frac{\Delta\phi}{2} + \dot{\phi}_D(w_2,L)(t-t_L) \tag{231}$$

and

$$t-t_L \leq \frac{\pi/2}{\dot{\phi}_D(w_2,L)} \tag{232}$$

c. Region of Drifting Debris Tube

Another interaction situation occurs when a second weapon is exploded in a drifting debris tube produced by an earlier burst, or when any debris tube is overtaken by another. Such a situation also leads to a disturbance in the electric field and magnetic-field-aligned-current systems, hence, to a modification of the injected-electron distribution. Again, owing to the enhanced electron flux, the loss rate also increases.

The interaction region due to a burst in a drifting debris tube may be specified as

$$\phi^*, \quad (\Delta\phi_1 + \Delta\phi_2)/2; \; L, \quad (\Delta L_1 + \Delta L_2)/2; \; t-t^*, \quad \Delta t \tag{233}$$

where ϕ^*, L^*, t^* are the coordinates and time of the first burst,

$\Delta\phi$ and ΔL are the dimensions of the debris tubes; the subscripts 1 and 2 denote the parameters due to the first and second bursts respectively

$$L = L^* + \int_{t^*}^{t} \dot{L}\,(t' - t^*)dt' \qquad (234)$$

$$\Delta L_n = \frac{L_n^2}{L_{o_n}}\,\Delta\phi_n, \quad n = 1,2 \qquad (235)$$

and $\qquad \Delta t = \dfrac{\Delta L_1 + \Delta L_2}{L(t - t^*)} \qquad (236)$

$\dot{L}$ is the outward drift, dL/dt, of the first debris tube.

The interaction region due to one debris tube overtaking another can be described by the equations:

$$\phi^*, \ (\Delta\phi_1 + \Delta\phi_2)/2; \ L_1 \le L \le L_2, \ \Delta t \le T_2 - T_1 \qquad (237)$$

where

$$T_n = \int_{L_m}^{L_m} \frac{dL}{\dot{L}_n} \ ; \quad n = 1,2 \qquad (238)$$

and

$$T_1 \le T_2 \ ; \ L_1 \le L_2 \qquad (239)$$

Here, L_m is the maximum L value for persistent trapping. Computer runs are required to determine the values of T for various initial values of L.

151

2. THE SUMMING REGION

It appears that the summing region is very limited. The yields of two
or more bursts may be summed only if one or more bursts occur within the
region where the debris due to a previous bur t is expanding radially
against the magnetic field. Hence, the bursts must be separated less
than about a second in time and less than about a single-burst-magnetic-
bubble diameter in space. Furthermore, the spatial separation and timing
of the bursts must be such as to avoid fratricide. Here, the principal
concerns may be the X-ray fluence, which may collapse the structures within
about a millisecond, and the neutron flux, which may substantially reduce
the yield of a second burst due to overinitiation. Since the travel time
of the neutrons is also of the order of a millisecond for a magnetic-
bubble-diameter separation, the bursts must occur in the restricted region
in space and in less than a millisecond in time to satisfy the summary
condition. It seems very unlikely that such conditions can be met.

3. THE NON-INTERACTION REGION

The noninteraction region, to first order, is that region $(\Delta x, \Delta t)$ out-
side the regions described above in Sections V.1 and V.2.

Section VI

RADIAL DIFFUSION OF ARTIFICIALLY TRAPPED ELECTRONS

1. THE NEED FOR A NEW TREATMENT OF RADIAL DIFFUSION

The electron loss model in Specter was originally based on the theory and
observations of pitch angle diffusion. Pitch angle diffusion is expressed
in a loss rate, which represents the rate at which trapped electrons are
precipitated into the atmosphere. The other forms of wave-particle inter-
actions, that lead to redistribution rather than immediate loss, were ig-
nored. The principal process that redistributes electrons between L-shells
is radial, or cross-L, diffusion. In the natural radiation belts, radial
diffusion is often important, but it seldom dominates the loss processes.
Until now the effects of radial diffusion have not seemed important enough
to include in Specter, mainly because of the uncertainties in the injec-
tion and initial debris distribution. However, with the development of an
improved injection model a new consideration of radial diffusion is called
for.

Radial diffusion has usually been treated in an approximation where pitch-
angle diffusion is accounted for by a simple loss rate (Ref. 35). This
leads to a diffusion equation for the flux as a function of L (35,36). But
the first adiabatic invariant must be assumed constant in such a formulation
if the variation of energy with L is to be computed. This contradicts the
known fact that the first adiabatic invariant is rapidly altered by pitch
angle diffusion. It therefore appears that a thorough treatment of diffu-
sion must include both pitch-angle diffusion and radial diffusion on an equal
basis.

In the case of artificial radiation belts there are some special reasons why
radial and pitch angle diffusion must be treated simultaneously. The initial
injected distribution is a highly non-equilibrium distribution, subject to
initial loss rates that may be much higher than the late time rates (Ref. 2,3).
The simplifying assumption of a constant loss rate (Ref. 35) is not valid.
A more subtle defect in the early treatments has to do with the dependence
of the diffusion rates on pitch angle. Pitch-angle diffusion — driven by
doppler-shifted resonances with cyclotron waves — tends to favor particles
with small pitch angles (Ref. 25). Electrons with pitch angles greater than

153

60° to 80° do not respond rapidly to pitch-angle diffusion. Radial dif-
fusion, on the other hand, favors electrons with pitch angles near 90°
(Ref. 37). So there is a possibility that radial diffusion could move a "pan-
cake" distribution near the equator inward or outward with rates higher than
predicted by the simplified calculations with constant loss rates, indepen-
dent of pitch angle.

The generalized diffusion equations for three degrees of freedom is (Ref. 6)

$$\frac{\partial F}{\partial t} = \sum_{jk} \frac{\partial}{\partial x_j} \left[\mathcal{J} D_{jk} \frac{\partial}{\partial x_k} \left(\frac{F}{\mathcal{J}} \right) \right] \tag{240}$$

where $F(M,J,\Phi)$ is a phase space distribution function in the three adiabatic
invariants, M. J, and Φ; and $\mathcal{J}$ is a Jacobian relating the adiabatic invar-
iants to three coordinates x_j. Walt (Ref. 39) suggested that one of the
degrees of freedom in (240) could be eliminated by choosing x_3 to be more
approximately conserved in both radial and pitch-angle diffusion. A use-
ful variable is

$$\eta \equiv \left(\frac{p^2}{m^2 c^2} \right) L^n = \frac{E(E+2mc^2)}{m^2 c^4} L^n \tag{241}$$

This variable is conserved to a high degree during pitch-angle diffusion,
and nearly conserved during radial diffusion. In radial diffusion the
exponent is exactly 3 for 90° pitch angles and approaches 2 for small pitch
angles (Ref. 40). For most radiation belt particles, an appropriate n is of
order 2.6 to 3.

The use of an assumed constant η is subject to the criticism that the energy
variations are not precisely accounted for if the diffusion equation is
set up with n constant. This is not necessarily a serious objection for
trapped electrons which diffuse predominantly toward lower pitch angles
with little energy change. Only in narrowly defined regions are pitch-
angle and radial diffusion equally important; usually one or the other
clearly predominates. Only if a particle can pass back and forth many times
between the regions, can the approximation of n constant have serious
consequences. Uusually, however, once an electron leaves the radial-
diffusion region, it is thereafter primarily subject to pitch-angle

154

diffusion. Figure 46 shows a concentrated electron distribution with the regions schematically indicated where each mode of diffusion dominates. A diffusion trajectory is sketched to illustrate that the diffusion processes are usually quite independent.

To construct the diffusion equation in L and $\mu \equiv \cos\alpha$, it is first necessary to obtain the Jacobian, $\mathcal{J}$. The first and second and third adiabatic invariants as functions of μ, L, and n, are, respectively

$$M = \frac{1}{2mB_E}\ n\ L^{3-n}\ (1-\mu^2) \tag{242}$$

$$J = \sqrt{n}\ R_E L^{1-n/2} \oint \sqrt{1-(1-\mu^2)\frac{BL^3}{B_E}}\ ds \tag{243}$$

$$\Phi = 2\pi B_E R_E^2/L \tag{244}$$

where B_E is the earth's surface field at the equator, and s is the (dimensionless) distance along a field line. The Jacobian is now (Ref. 37)

$$\mathcal{J} \equiv \frac{\partial(M,J,\Phi)}{\partial(n,\mu,L)} = 4\pi\frac{R_E^3}{m}\ L^{2-3n/2}\ \sqrt{n}\mu T \tag{245}$$

where T represents the quarter bounce integral.

$$T = \frac{1}{4}\oint \frac{ds}{\cos\alpha} \simeq 1.3802 - .6397(1-\mu^2)^{3/8} \tag{246}$$

The diffusion operators are found by applying the chain rule to the partial differentials:

$$\left(\frac{\partial}{\partial L}\right)_M = \left(\frac{\partial}{\partial L}\right)_\mu + \frac{(3-n)(1-\mu^2)}{2\mu L}\left(\frac{\partial}{\partial\mu}\right)_L \tag{247}$$

The customary notation $(\frac{\partial}{\partial x})_y$ means a partial derivative with y held constant. At this point it is clear that n=3 is an especially felicitous choice, since the cross derivatives, $\frac{\partial^2}{\partial L\partial\mu}$ and $\frac{\partial^2}{\partial\mu\partial L}$, are thereby eliminated. Even for n less than 3 the cross derivatives are small. Ignoring the cross derivatives leads to the diffusion equation

$$\frac{\partial f}{\partial t} = \frac{1}{\mu T}\frac{\partial}{\partial\mu}\left[\bar{D}\mu\mu\ \mu T\ \frac{\partial f}{\partial\mu}\right]_n$$
$$+ L^{-2+3n/2}\frac{\partial}{\partial L}\left[\bar{D}_{LL}\ L^{2-3n/2}\ \frac{\partial f}{\partial L}\right]_n \tag{248}$$

The distribution function here is the phase space distribution at the equator. In terms of the directional flux j

155
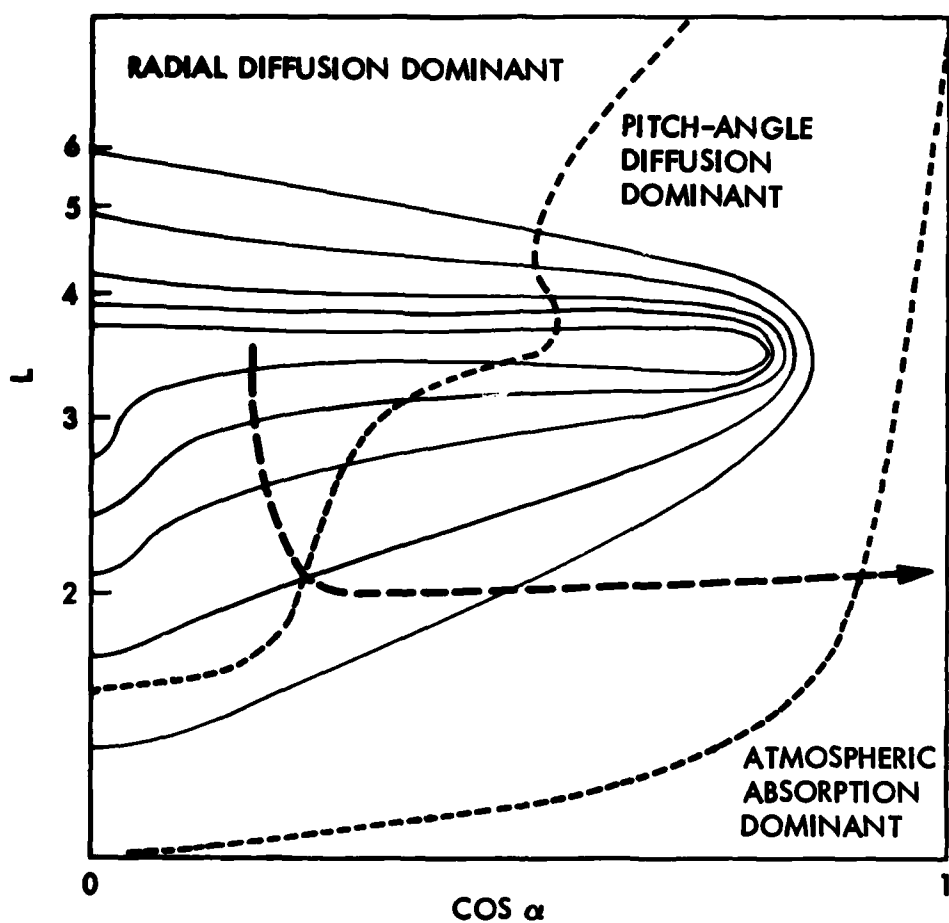
Figure 46. A typical artificial electron distribution
(contours) in L and cosine of pitch-angle.
The dotted lines separate regions where
radial diffusion, pitch angle diffusion,
and atmospheric loss, respectively, dominate.
A hypothetical diffusion trajectory is shown
as a dashed curve.

156

$$f = j(E,\mu,L)/p^2 \tag{249}$$

(The diffusion coefficients are written with a bar, $\overline{D}$, to signify that these are bounce averaged.)

It is curious that for $n = 8/3$ the L diffusion operator reduces to the earlier form (Refs. 1,2). This corresponds to equatorial pitch angles near 40°. The diffusion operator for n=3 is (Ref. 39)

$$L^{5/2} \ \frac{\partial}{\partial L}\left[\ \overline{D}_{LL} \ L^{-5/2} \ \frac{\partial f}{\partial L}\ \right]_\eta \tag{250}$$

Various values have been published for the diffusion coefficients. For $\overline{D}_{\mu\mu}$ we have used a value adjusted to match the values of Lyons, Thorne, and Kennel (Ref. 25):

$$\overline{D}_{\mu\mu} \simeq 1.3 \times 10^{-8} \eta^{-3/4} \ L^{3/2} \ B_w^2 \ (1-\mu^2) \tag{251}$$

where B_w is an assumed broad-band wave amplitude. For $\overline{D}_{LL}$ Schulz and Lanzerotti give several forms: for magnetic impulses

$$\overline{D}_{LL} \ \propto \left[.32 + .68 \ (1-\mu^2)^{1.7}\right] L^{10} \tag{252}$$

and for electric impulses

$$\overline{D}_{LL} \propto L^{10} \tag{253}$$

2. SOLVING THE COMBINED RADIAL AND PITCH-ANGLE DIFFUSION EQUATION

The combined diffusion equation (248) is well suited to a numerical solution. First note that an advantageous change of variables is

$$x \equiv \mu^2 \tag{254}$$

$$y \equiv L^{3-3n/2} \tag{255}$$

$$\frac{\partial f}{\partial t} = \frac{1}{T} \frac{\partial}{\partial x}\left[D_{xx} \ T \ \frac{\partial f}{\partial x}\right] + \frac{\partial}{\partial y}\left[D_{yy} \ \frac{\partial f}{\partial y}\right] \tag{256}$$

$$D_{xx} = \overline{D}_{\mu\mu} \ \mu^2 \tag{257}$$

157

$$D_{yy} = \bar{D}_{LL} \ (3 - \frac{3n}{2})^2 L^{4-3n} \tag{258}$$

In the loss cone one must also subtract a loss term

$$\left(\frac{\partial f}{\partial t}\right)_L = \frac{2wf}{\tau_b} \tag{259}$$

where τ_b is the bounce period, $4R_E T/V$. The empirical factor w can be adjusted to match the detailed solutions. With no atmospheric back-scatter, its value is near 1 (Ref 41). The atmospheric backscatter at high energies is slight (Ref. 42); it is probably preferable at present to ignore backscatter and use the above loss rate with w=1. The form of the loss term is such that one need only replace f by

$$f_{LC} = g \ \exp \ (-2t/\tau_b) \tag{260}$$

and solve Eq. (256) (with no loss term) for g in place of f.

Eq. (256) calls for a predictor-corrector method to do the forward time integration. Let f'_x and f'_y be the x and y diffusion terms on the right, thus

$$\frac{\partial f}{\partial t} = f'_x + f'_y \tag{261}$$

An Adams-Bashforth type method is suited to this form. The essence of that method is to expand the derivatives, $(\frac{df}{dt})$ in a Tayler series,

$$f'_x \ (t) \simeq f'_x \ (t_n) + 2C_{x1} \ (t - t_n) + 3C_{x2} \ (t - t_n)^2 + \dots \tag{262a}$$

$$f'_y \ (t) \simeq f'_y \ (t_n) + 2C_{y1} \ (t - t_n) + 3C_{y2} \ (t - t_n)^2 + \dots \tag{262b}$$

The values of f'_x and f'_y on the right are evaluated at the point t_n.

The predictor step consists in stepping forward from the point t_n to t_{n+1}; using the values of f at t_n and the values of f at preceding points (see Figure 47). The predictor step is

158
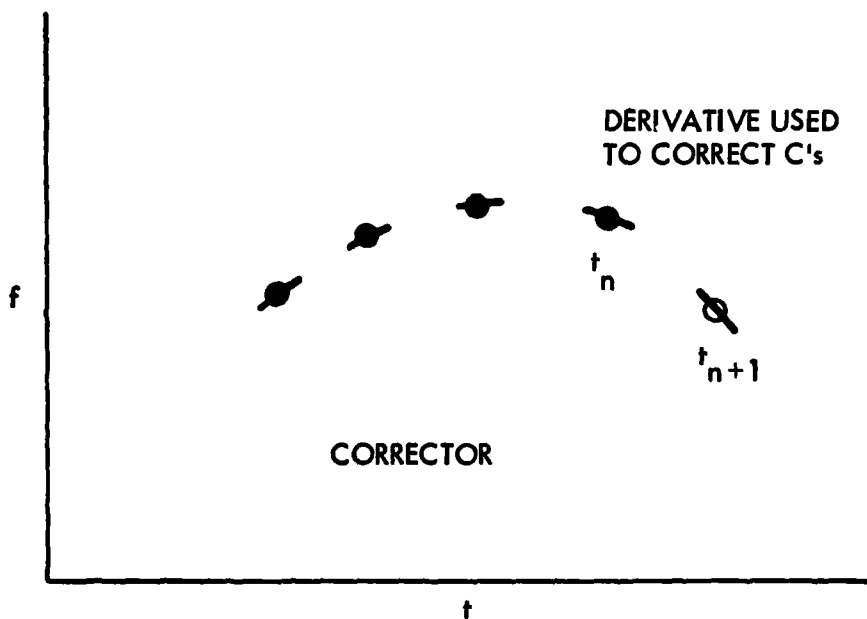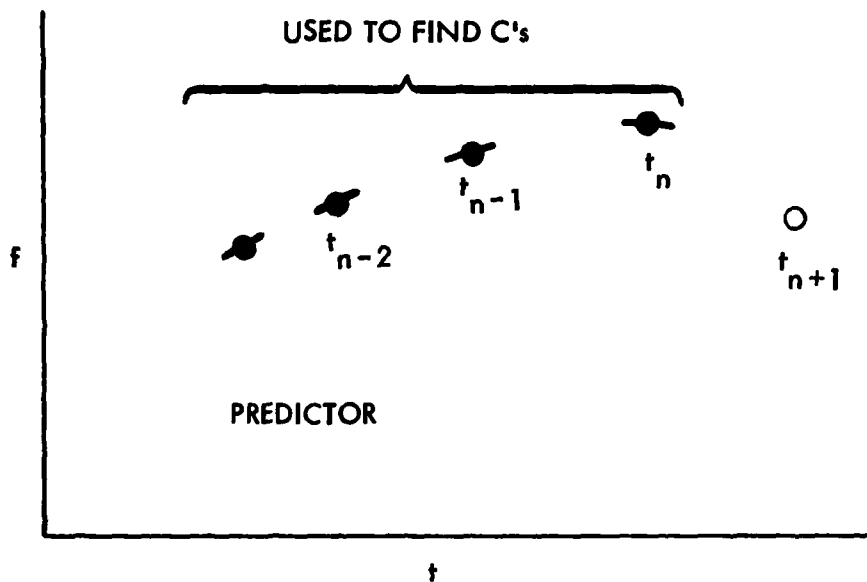
Figure 47. A predictor-corrector integration for a single forward step, from t_n to t_{n+1}.

159

$$f(t_{n+1}) \simeq f(t_n) + \left[f_x'(t_n) + f_y'(t_n) \right] \Delta_{n,n+1}$$

$$+ \left[C_{x1} + C_{y1} \right] \Delta_{n,n+1}^2 + \left[C_{x2} + C_{y2} \right] \Delta_{n,n+1}^3 + \ldots \qquad (263a)$$

$$\Delta_{n,n+1} \equiv t_{n+1} - t_n \qquad (263b)$$

In the corrector step, the new values of f at t_{n+1} are used to find f_x' and f_y' there; the new f'’s are then used to find new C's expanded about t_{n+1}. The corrector step then gives for f:

$$f(t_{n+1}) \simeq f(t_n) + \left[f_x'(t_n) + f_y'(t_n) \right] \Delta_{n,n+1}$$

$$\qquad\qquad (264)$$

$$- \left[C_{x1} + C_{y1} \right] \Delta_{n,n+1}^2 + \left[C_{x2} + C_{y2} \right] \Delta_{n,n+1}^3 - \ldots$$

Taylor expansion gives, about t_n:

$$C_m = \sum_{k=1}^{n-1} \left[f'(t_k) - f'(t_n) \right] D_{mk} \qquad (265)$$

$$D_{mk} = \frac{1}{m+1} (-1)^{n-k} \Sigma\{\Pi \left[\text{all } \Delta_j \neq k,_n \right];$$

$$(n-m-1) \text{ at a time}]\}/\Pi \left[\text{all } \Delta_{jk} \right]; \ m \neq n; k \neq n \qquad (266)$$

where Σ and Π are the conventional notation for extended sums and products, respectively.

The formation of f_x' and f_y' presents difficulties because of restrictions on the size of the four-dimensional integration grid (in x, y, t, and η). It pays to have a differentiation method that minimizes computer storage space, even at the apparent expense of computing time. Spline methods are usually quite successful in estimating derivatives in a grid of discrete points (Ref. 43). To construct a cubic spline of f over a discrete variable z, let

$$\Delta_i \equiv (Z_i - Z_{i-1})/3 \qquad (267)$$

$$\lambda_i \equiv \frac{\Delta_{i+1}}{\Delta_i(\Delta_i + \Delta_{i+1})} \qquad (268)$$

$$\mu_i \equiv \frac{\Delta_i}{\Delta_{i+1}(\Delta_i + \Delta_{i+1})} \qquad (269)$$

$$u_i \equiv \lambda_i(f_i - f_{i-1}) + \mu_i(f_{i+1} - f_i) \qquad (270)$$

To evaluate the derivatives, $(\frac{df}{dZ})_i$ one now must invert a tridiagonal matrix equation

$$\lambda_i \Delta_i \left(\frac{df}{dZ}\right)_{i-1} + 2\left(\frac{df}{dZ}\right)_i + \mu_i \Delta_{i+1} \left(\frac{df}{dZ}\right)_{i-1} = u_i \qquad (271)$$

The spline, however, contains two unknown parameters, which are usually to be specified at the two end points. Derivative boundary conditions are especially useful, because two $(\frac{df}{dt})$'s are directly specified. When no boundary condition is available, it is necessary to estimate the derivative by fitting a polynomial over the adjacent end points.

Using the logarithm in place of f has several advantages, the most important of which is the assurance that f will remain positive. The diffusion operators are now of the form

$$f'/f = g \frac{1}{f} \frac{\partial}{\partial Z} \left[h \frac{\partial f}{\partial Z} \right]$$

$$= gh \left[\frac{\partial \ln f}{\partial Z} \right]^2 + g \frac{\partial}{\partial Z} \left[h \frac{\partial \ln f}{\partial Z} \right] \qquad (272)$$

(it might sometimes be desirable to compute the derivatives of f; this is rather inefficient because f must be evaluated from log (f) at every time step.) Two conservative applications of the spline yield the second order differential operators. Figures 48 and 49 show the results of several trial calculations. A rather coarse grid of 13 points was used, nonetheless the second derivatives were computed quite successfully. A secondary advantage of Eq. (272) is that the squared term on the right usually dominates for interior points. This aids the accuracy in minimizing the errors that inevitably occur in the second derivative.

The natural boundary conditions for the radial diffusion operator are $\frac{df}{dy} \sim 0$ at $y \sim 0$ and $f \sim 0$ at $f \sim 1$. The first condition ensures that the current (the bracketed term in Eq. (256) goes to zero at $L \sim \infty$. The boundary conditions for the pitch angle diffusion operator are more subtle. If D_{xx} were finite at the ends, x=0 and x=1, the appropriate boundary condition would be $\frac{\partial f}{\partial x}=0$. But D_{xx} may vanish at the ends, leaving an indeterminate boundary condition. In that case one obtains, instead, a relation between the derivatives:

161
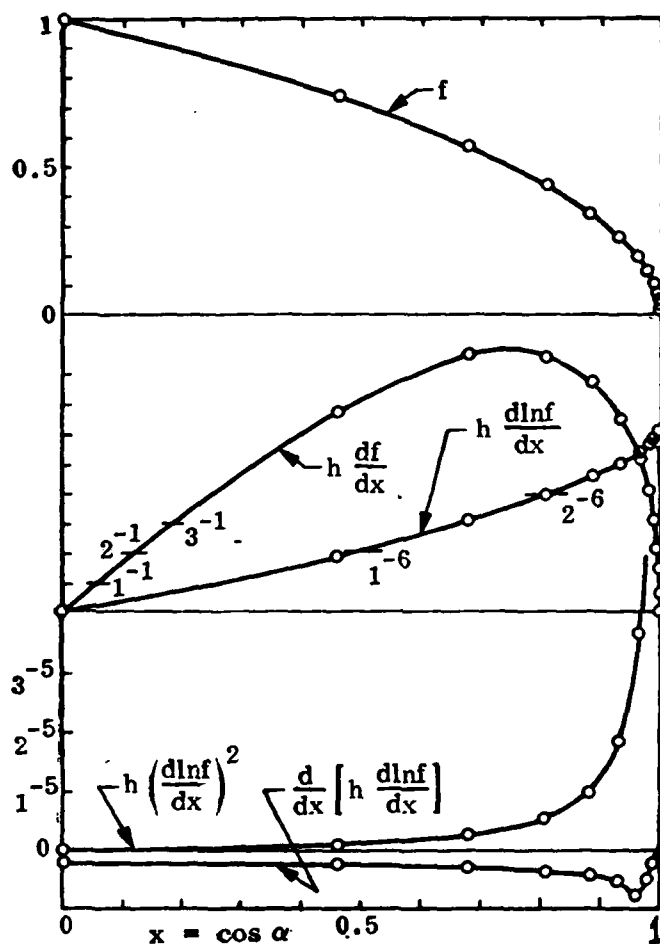
Figure 48. A test case showing the derivatives evaluated
by a spline approximation. The circled points are
the discrete points at which the distribution function,
f, was evaluated. This case corresponds to a high L
shell with a very small loss cone (on the right). The
exponents denote powers of 10.

162
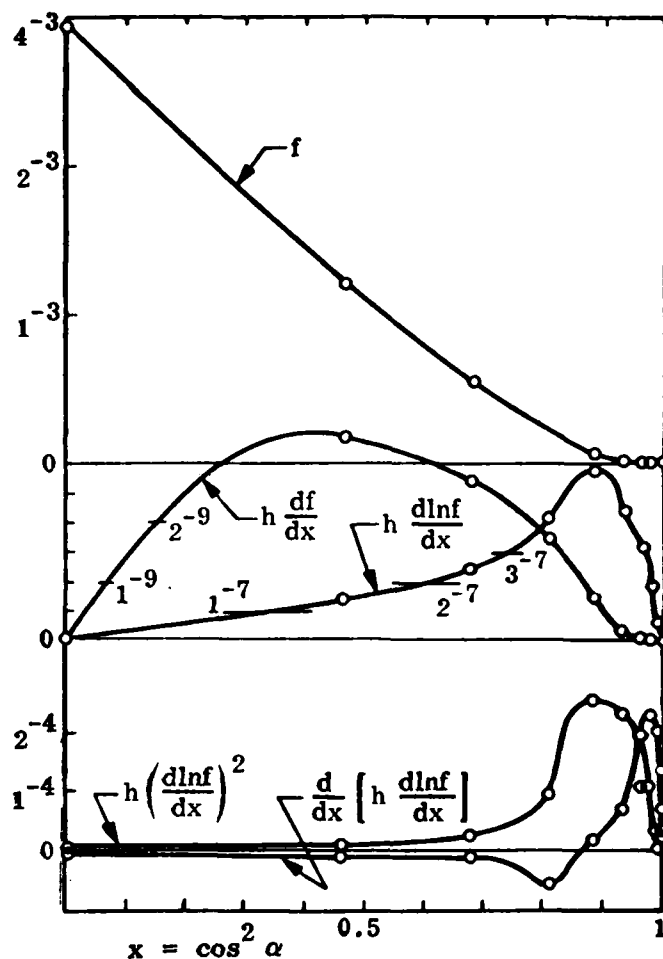
Figure 49. A test case showing the derivatives evaluated by a
spline approximation. The circled points are the discrete
points at which the distribution function, f, was evaluated.
This example shows clearly the excessive curvature of $n\frac{\partial f}{\partial x}$
near x=0 which makes the logarithmic differentiation
preferable. This case is for an intermediate L shell.   The
exponents denote powers of 10.

163

$$\frac{\partial}{\partial x}\left[hx\,\frac{\partial f}{\partial x}\right] - h(0)\,\frac{\partial f}{\partial x} \tag{273}$$

A supplementary condition may also be posed that $\frac{\partial f}{\partial x}$ is always negative at the two ends; this ensures that numerical errors do not introduce a spurious particle source at the boundary.

A computer code has been developed to implement the differential equation solution. It constructs solutions over constant η slices through the distribution. The number of η's is somewhat arbitrary, they can be selected one at a time and the results can be stored temporarily so that the resulting table of f values can be interpolated to selected energies. The main determinants of the needed storage space are the size of the x,y grid and the number of time points needed for a satisfactory solution. For convenience the x and y arrays are nearly the same size, about 15 to 30 points each. A satisfactory integration can be carried out with less than 5 to 8 time points. The maximum number of f values that need to be stored for any is about 2000 (two time points). The maximum number of f values is about 15,000 (including both f_x' and f_y'), with approximately the same number of C's.

In the cases that have been tested there were always regions in x, y, and t where radial diffusion dominated. This is because, despite the usual vast differences in the magnitude of the diffusion coefficients, the pitch angle distribution quickly approaches a lowest normal mode. Steep gradients in L, though, can persist for rather long times. If appreciable differences do exist in the characteristic diffusion rates the scheme developed here is quite advantageous. Usually with two modes of diffusion one would set up two separate time scales; the integration method described above is readily adapted to that approach. We selected an alternate approach that may be somewhat less efficient, but suffers from fewer computational complexities. Our approach was to set the numbers of time points for f_x' and f_y' according to the respective diffusion rates. The use of a high order Adams-Bashforth method is intended to maximize the time steps. The step size can therefore be set to accommodate the slower process, with just 2 or 3 time points; the order of the faster process is then adjusted for acceptable accuracies. Ideally we would like to use a vairable order at each point in the x,y grid. The economies of such a scheme are obvious, although coding complexities made it undesirable for the first trials.

164

3. RESULTS OF RADIAL DIFFUSION COMPUTATIONS AND ADJUSTMENTS TO THE
   SPECTER LOSS MODEL

In the earlier computations of radial diffusion rates following an artificial
injection event (Ref. 35), the effects of radial diffusion were negligible
compared with loss due to pitch-angle diffusion. Figure 50 is a reproduc-
tion of Figure 3-3 from the earlier report. The new computations, with
increased pitch angle diffusion rates at early times, were not expected
to result in significantly more radial diffusion at high L-shells. They
should, however, tell whether the elevated radial diffusion rates of equa-
torially mirroring electrons, as discussed in VI.1, could alter the diffu-
sion toward low L shells.

Table 4 shows the results of the first few steps of a trial computation
up to 1.4 seconds.

The initial distribution was chosen to have a steep radial gradient near
L=3 and a near-normal mode pitch-angle distribution. The initial values
of f_x' and f_y' show clearly the regions which favor the separate diffusion
processes. The example does demonstrate the expected preference for radial
diffusion at large pitch angles, but not enough to outweigh the loss over
the entire distribution due to pitch-angle diffusion. In fact, because of
the different radial dependence of radial and pitch-angle diffusion coef-
ficients, the radial gradient in the omnidirectional flux can actually
steepen with time at the outer edge of the "slot" region — L $\approx$ 2.3 to
L $\approx$ 3. A very large radial diffusion coefficient was chosen for the test
case, in a realistic case pitch-angle diffusion would dominate everywhere
below L $\approx$ 6.

It may be concluded that radial diffusion is not likely to be important in
artificial radiation belts, except perhaps near synchronous altitudes. At
synchronous altitudes and beyond our knowledge of radial diffusion rates
is not sufficient to make definitive predictions. Below L $\sim$ 3, in the
slot and inner belt, radial diffusion can be definitely ignored.

165
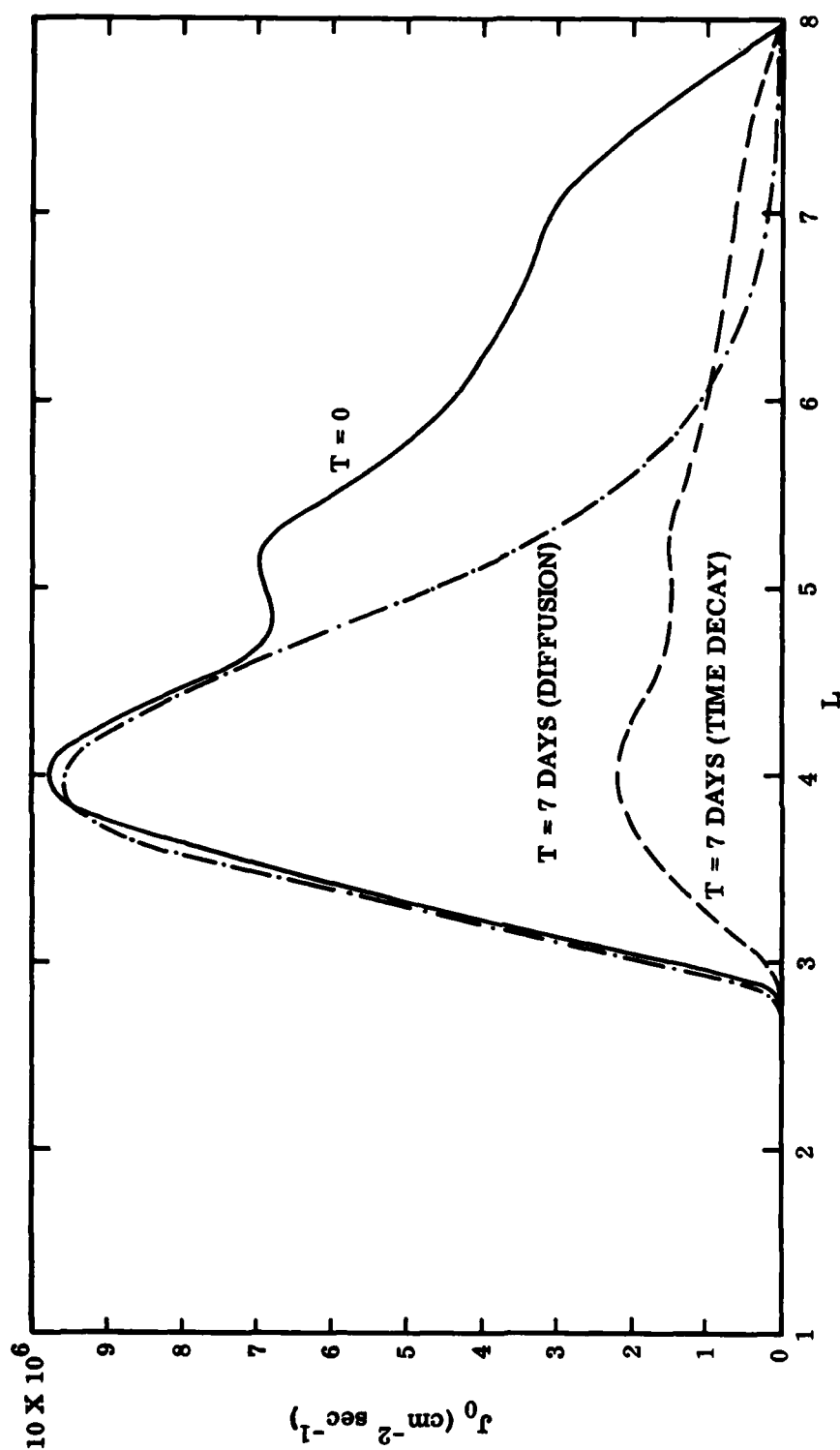
Figure 50. Jo, the radial omnidirectional flux at the equator, at various times for the detonation near L = 4.0. Shown are the initial flux values for t = 0 (solid curve); the flux after 7 days of diffusion, but no time decay, determined by the numerical solution to the diffusion equation (dot-dashed curve); and the flux after 7 days of time decay, but no diffusion (dashed curve).

166

Table 4 Initial results of a test case at $\eta = 20$. The unshaded values of f'_x and f'_y indicate where each dominates; at the right side atmospheric absorption is the predominant effect on particles in the loss cone. The values of $f(t=1.4)$ are shaded where a decrease occurs. The diffusion coefficients at $L = 3$ were:

$$D_{\alpha\alpha} = 1.3 \times 10^{-6} \ sec^{-1}$$
$$D_{LL} = 3 \times 10^{-4} \ sec^{-1}$$

f(t=0)

L\α(deg)	90.00	47.23	34.56	25.93	19.96	15.16	11.06	8.28	6.01	4.10	2.59	1.24	0.00
∞	1.0000	.7340	.5673	.4372	.3413	.2616	.1918	.1440	.1047	.07150	.04528	.02160	.01071
10.36	.9999	.7338	.5669	.4367	.3406	.2605	.1907	.1423	.1025	.06822	.03980	.02385	.01616
6.38	.9988	.7325	.5654	.4347	.3382	.2574	.1864	.1366	.09442	.05535	.03337	.02271	.01797
4.74	.7949	.5470	.4000	.2905	.2137	.1521	.1005	.06568	.03644	.02082	.01361	.01050	.00927
3.71	.08578	.04541	.02638	.01494	.00840	.00418	.00141	.00050	.00023	.00014	.00011	.00010	.00010
3.03	.01553	.00758	.00407	.00207	.00100	.00036	.00014	.00007	.00004	.00003	.00003	.00003	.00003
2.53	.00295	.00121	.00054	.00021	.00006	.00002	.00001	.00000					
2.09	.00061	.00021	.00006	.00001	.00000								
1.78	.00007	.00003	.00001	.00000									
1.54	.00000												
1.33	.00000												
1.16	.00000												

atmospheric cutoff

Table 4 (cont.) $(N\underline{+}M \equiv N \times 10^{+M})$

$$f'_x(t=0)/f(t=0)$$

L\α(deg)	90.00	47.23	34.56	25.93	19.96	15.16	11.06	8.28	6.01	4.10	2.59	1.24	0.00
∞	-2.8-5	-1.9-5	-6.7-6	1.3-5	4.9-5	1.1-4	2.4-4	5.1-4	8.5-4	2.6-3	3.8-3	2.9-2	1.1-1
10.36	-3.1-3	-1.7-3	-1.7-3	4.1-3	-1.4-3	3.1-2	-2.3-2	1.7-1	-1.4-1	616-1	6.1-1	2.3	5.9
6.38	-7.2-4	-5.2-4	-1.1-4	1.7-4	1.6-3	2.1-3	7.4-3	1.5-2	-3.9-3	2.1-1	1.7-1	3.8-1	7.6-1
4.74	-3.4-4	-1.6-4	-1.7-4	6.7-4	-9.5-5	4.2-3	-1.2-3	1.4-2	3.5-2	8.6-2	6.6-2	9.7-2	1.6-1
3.71	-2.0-4	-1.3-4	1.3-4	2.2-4	1.2-3	1.4-3	4.6-3	2.3-2	3.0-2	3.9-2	2.8-2	2.7-2	3.6-2
3.03	-3.3-4	-3.2-5	7.6-5	4.7-4	8.3-4	2.1-3	1.1-2	2.2-2	1.9-2	1.7-2	1.1-2	7.4-3	8.1-3
2.53	-8.5-5	-3.8-5	1.4-4	2.5-4	9.2-4	3.9-3	4.6-3	7.2-3	5.4-3	3.8-3	2.3-3	1.2-3	1.0-3
2.09	-5.8-5	-9.0-6	1.4-4	3.1-4	2.2-3	2.4-3	2.4-3	2.6-3	1.7-3	9.5-4	4.8-4	1.8-4	1.3-4
1.78	-4.3-5	3.5-5	9.9-5	1.0-3	7.6-3	1.3-3	9.8-4	8.6-4	5.0-5	2.2-4	9.2-5	2.6-5	1.5-5
1.54	-2.0-5	1.9-6	1.9-4	3.3-4	4.8-4	3.2-4	2.1-4	1.7-4	8.3-6	2.9-5	9.8-6	2.1-6	9.6-7
1.33	-1.9-5	9.8-6	1.1-4	1.3-4	1.4-4	8.9-5	5.0-5	3.4-5	1.3-5	3.5-6	9.8-7	1.5-7	5.9-8
1.16	-9.1-6	3.1-6	4.2-5	5.9-5	6.9-5	4.6-5	2.7-5	1.8-5	7.0-6	1.8-6	5.2-7	7.9-8	3.0-8

Table 4 (cont.)

$$f'_y(t=0)/f(t=0)$$

L\α(deg)	90.00	47.23	34.56	25.93	19.96	15.16	11.06	8.28	6.01	4.10	2.59	1.24	0.00
∞	8.1-2	1.0-1	1.2-1	1.4-1	1.5-1	1.7-1	1.7-1	1.5-1	1.5-1	-1.9-1	-4.5-1	5.5-1	1.9
10.36	-2.0-2	-2.5-2	-3.0-2	-3.4-2	-3.9-2	-4.2-2	-4.7-2	-4.7-2	-5.7-2	4.4-4	6.9-2	-1.0-1	-9.6-2
6.38	-1.8-2	-2.3-2	-2.6-2	-3.0-2	-3.2-2	-3.4-2	-3.4-2	-2.9-2	-1.7-2	6.2-2	1.0-1	-1.0-1	-3.8-1
4.74	9.0-3	1.3-2	1.6-2	2.0-2	2.4-2	2.9-2	3.5-2	4.3-2	6.1-2	4.8-2	2.9-2	7.1-2	-1.4-1
3.71	4.6-3	6.0-3	7.3-3	8.9-3	1.1-2	1.3-2	1.9-2	2.7-2	3.0-2	3.3-2	3.7-2	1.9-2	-4.2-3
3.03	4.6-3	5.2-3	5.7-3	6.3-3	7.0-3	8.4-3	1.0-2	1.1-2	1.0-2	8.5-3	6.3-3	1.1-2	1.7-2
2.53	1.1-3	1.1-3	1.2-3	1.3-3	1.5-3	1.9-3	1.6-3	1.2-3	7.3-4	8.0-4	1.2-3	-3.7-4	-2.4-3
2.09	2.1-4	2.6-4	3.2-4	4.6-4	6.5-4	6.8-4	6.4-4	5.8-4	5.4-4	4.2-4	2.8-4	6.9-4	1.3-3
1.78	7.7-5	9.0-5	1.2-4	1.6-4	1.6-4	1.4-4	1.2-4	1.1-4	1.0-4	1.3-4	1.7-4	4.7-5	-1.2-4
1.54	5.1-5	5.2-5	5.7-5	4.1-5	2.2-5	1.0-5	5.4-7	-5.1-6	-7.9-6	-1.7-5	-2.9-5	6.6-6	5.6-5
1.33	2.3-5	2.4-5	2.1-5	1.7-5	1.3-5	1.1-5	1.0-5	1.1-5	1.1-5	1.4-5	1.7-5	6.5-6	-8.6-6
1.16	8.3-6	6.9-6	5.7-6	6.2-6	6.5-6	7.2-6	7.0-6	6.7-6	6.4-6	4.9-6	2.7-6	9.0-6	1.8-5

Table 4 (cont.)

f(t=1.4sec)

L α(deg)	90.00	47.23	34.56	25.93	19.16	15.16	11.06	8.28	6.01	4.10	2.59	1.24	0.00
∞	1.0129	.7386	.5750	.4520	.3482	.2744	.1977	.1527	.1129	.0798	.06374	.04044	.04587
10.36	.9879	.7928	.5504	.4420	.3260	.2690	.1862	.1485	.1142	.0957	.07186	.06148	.05819
6.38	.9917	.7260	.5608	.4304	.3362	.2551	.1873	.1368	.09916	.06170	.03714	.04958	.04555
4.74	.7990	.5524	.4046	.2961	.2178	.1574	.1041	.07023	.02976	.01192	.00299	.00124	.00101
3.71	.3982	.2417	.1587	.1028	.06741	.04146	.02235	.01024	.00118	.00005	.00002	.00002	.00001
3.03	.08655	.03570	.05208	.01530	.00851	.00423	.00143	.00003	.00000				
2.53	.01556	.00900	.00425	.00207	.00101	.00036	.00000						
2.09	.00295	.00135	.00055	.00021	.00006	.00000							
1.78	.00061	.00021	.00007	.00001	.00000								
1.54	.00007	.00003	.00001	.00000									
1.33	.00000												
1.16	.00000												

170

The calculations of radial diffusion rates have all been done with assumed rates derived for the natural radiation belts. We have ignored the effect of electromagnetic disturbances due to the nuclear explosion. One might, a priori, conclude that the disturbances do not last long enough to cause substantial radial diffusion, which usually takes place on a time scale comparable to the particles drift periods. The discrepancies noted above between the injection model and the Telstar data above L $\approx$ 2 could perhaps be a result of radial diffusion. Whether radial diffusion was actually effective is a question that is unlikely to be answered. Whether the discrepancies are consistent with radial diffusion is a question that can be examined with the new diffusion code.

SECTION VII

RECONCILIATION OF THE ELECTRON LOSS MODEL TO DATA BODIES

1.   NEW DATA BODIES

In an earlier report (Reference 3) an extensive comparison was made of the Specter
electron loss model with available data, particularly from the artificial
radiation belts. The data on artificial belts have been quite thoroughly analyzed,
and no high altitude nuclear tests are expected in the future, so we must rely on
natural belt data to fill the gaps in our knowledge of decay rates. The principal
deficiencies in the loss model are at low altitudes, where the longitude-
dependent filling of the drift loss cone is important, and at very high altitudes,
where the decay is complicated by radial diffusion and other transient phenomena.

Several important data bodies have been reported since the earlier report
(Reference 3). At low and intermediate altitudes the relevant new data are those
of Imhof (Reference 30) and Vampola (Reference 29). These data are highly
promising since they often define the loss cone distribution to a much higher
degree of precision than previous data. Unfortunately, they still await a detailed
theoretical analysis that might define the rates of diffusion into the loss cone.
This problem can only be approached with an extensive computation of the combined
effects of pitch-angle diffusion at high altitudes, scattering in the atmosphere,
and longitudinal drift. Earlier treatments, though marginally adequate for the
present loss model, are totally insufficient for a precise determination of
diffusion rates, mainly because of neglect of atmospheric backscatter. Another
problem has become apparent over the last two years, to wit: what is the signifi-
cance of interactions with man-made VLF emissions? The issue is still somewhat
controversial, but there is a growing body of evidence that the man-made emissions
are very important (References 27 - 30). At high altitudes the nature of the VLF
wave sound makes little difference to the Specter loss model. At low altitudes,
because of the complicating effect of longitudinal drift, the mechanism of wave
generation is crucial. Sporadic or coherent VLF waves affect trapped electrons in

172

an entirely different fashion (Reference 31) from the steady loss assumed in the theories of Kennel and Petscheck (Reference 24) and Lyons, Thorne, and Kennel (Reference 25). The issue has not been resolved yet, though the next year might bring substantial progress.

At high altitudes, the recent data of West (Reference 44) using observations from OGO-5, are especially valuable. For the first time we have available data with sufficient resolution to test the combined effects of radial and pitch angle diffusion beyond $L=4$. The data cover the energy range of interest in Specter, so their analysis should yield much improved loss rates in the outer radiation belt. The data are just beginning to be analyzed to determine diffusion rates; unfortunately no concrete results were available at the time of this report.

2. COMPARISON OF DATA BODIES WITH SPECTER

The loss rates in Specter have been compared with all the available artificial radiation belt data and large parts of the natural radiation belt data, the results were described in the earlier report on the improvement of Specter II (Reference 3). The only major unresolved discrepancies are those that appear in the early times, as discussed above in Section III. Because of the incomplete state of the analysis of recent data we were not able to make any additional comparisons with loss rates at late times.

3. IMPROVEMENTS NEEDED IN THE SPECTER LOSS MODEL; NORMAL-MODE DECAY VS. NUMERICAL MODELLING

The deficiencies in the Specter electron-loss model affect the decay rate at early times and the distribution at low altitudes. The present decay model is completely empirical and obviously cannot apply exactly to every possible case. A question that has frequently been brought up is the desirability of replacing part or all of the decay model by an actual solution to a diffusion equation. There are many ways this might be accomplished, among them the use of an eigenfunction expansion, or a direct numerical solution of a diffusion equation, as described above in Section VI.

173

The use of an eigenfunction expansion appears attractive because of the possibility of high computational efficiency. Schulz has developed an interesting scheme in which the pitch-angle variable is replaced by a new variable which contains the bounce integral and all the sine and cosine factors taht usually appear in the diffusion operator (Reference 45). His variable is similar to x, as used in Section VI. The inclusion of the bounce integral, T, leads to inconsequential numerical differences. Schulz's diffusion coefficient is, however, quite different from the forms assumed above for D_{xx}. The diffusion coefficient $D_{\alpha\alpha}$ in Section VI was assumed finite, which led to awkward, but tractable, boundary conditions. Schulz, on the other hand, assumed a diffusion coefficient that implied $D_{\alpha\alpha} \to \infty$ at both ends, $x = 0^{\circ}$ and $\alpha = 90^{\circ}$. The physical implications of an infinite diffusion coefficient are not clear; the published values (Reference 25) of $\overline{D}_{\alpha\alpha}$ seem relatively constant at $\alpha \sim o$ and generally vanish at $\alpha \sim 90^{\circ}$. The Schulz scheme has one special advantage, that the eigenfunctions can be constructed of elemetnary functions that need not be recomputed at every step. A loss model that required the evaluation of other functions, such as Bessel functions, would be out of the question because of the excessive computation time. A criticism that may be very serious, is that the eigenfunctions may be too simple to adequately represent the lowest normal mode. The pitch-angle distribution of the trapped particles in Specter was carefully fitted to a large body of data at late times. It is doubtful whether simpler functions would be adequate.

An alternate approach would be to construct a lowest normal mode similar to the present pitch-angle distribution. From the lowest mode the higher eigenfunctions could be computed numerically and stored as interpolation coefficients. It is quite feasible to add pitch-angle points (or minor points) to the present arrays to facilitate efficient, accurate computation. Interpolation by evaluation of a second or third degree interpolation polynomial is much more efficient than the evaluation of higher functions. (The computation of the eigenfunctions is straightforward and need only be performed once, so the added computation is insignificant.)

The (bounce averaged) pitch-angle diffusion equation is

$$\frac{\partial f}{\partial t} = \frac{1}{T_\mu} \frac{\partial}{\partial \mu} \left[\overline{D}_{\mu\mu} T_\mu \frac{\partial f}{\partial \mu} \right] + Q \qquad (274)$$

174

where Q is a source of particles. In a steady state, $\partial f/\partial t = 0$, a simple solution
results for D and Q of the assumed forms

$$\bar{D}_{\mu\mu} \propto \frac{1-\mu^2}{T_\mu^2} \tag{275}$$

$$Q \propto \frac{1}{T} \tag{276}$$

The above diffusion coefficient is physically realistic and resembles the
coefficients of Lyons, Thorne and Kennel (Reference 25). The trapped
distribution is then

$$f \propto (\mu_c^2 - \mu^2 + \ln\frac{1-\mu^2}{1-\mu_c^2} + C_1) \tag{277}$$

Where μ_c is the (global) atmospheric cutoff. The constant C_1 can be evaluated
by constructing a loss cone solution (involving Bessel functions) (References
46, 47) and fitting the solution at μ_c.

Equation (277) suggests a form for the lowest normal mode in a freely-decaying
distribution

$$f = C_2 \left[(\mu_c^2 - \mu^2)^{n/2} + \frac{\ell - n}{2} \ln \frac{1-\mu^2}{1-\mu_c^2} + C_1 \right] \exp(-t/T) \quad 2 \leq n \leq 4 \tag{278}$$

This is nearly indistinguishable from the distribution now in Specter. It also
has the advantage of a gradual transition across μ_c to the loss-cone distribution.
That transition, where the present distribution function in Specter vanishes,
has been a weak point in the representation of drift loss-cone fluxes. Equation
(278) must be a solution of the diffusion equation

$$\frac{\partial f}{\partial t} = -\frac{1}{T}f = \frac{1}{T\mu} \frac{\partial}{\partial \mu}\left[\bar{D}_{\mu\mu} T_\mu \frac{\partial f}{\partial \mu} \right] \tag{279}$$

Substitution in (279) gives a differential equation for $\bar{D}_{\mu\mu}$:

175

$$T\mu \ (\mu_c^2 - \mu^2)^{\mu/2} + \frac{4-n}{2} \ln \frac{1-\mu^2}{1-\mu_c^2} + C_1 \tag{280}$$

$$= \frac{\partial}{\partial \mu} \ [D_{\mu\mu}\tau T_\mu \left\{ n\mu(\mu_c^2 - \mu^2)^{\frac{n-2}{2}} + (4-n)\frac{\mu}{1-\mu^2} \right\}]$$

$$= \frac{\partial}{\partial \mu} \ [D_{\mu\mu}\tau T \ \frac{\mu}{1-\mu^2} \left\{ n(1-\mu^2)(\mu_c^2-\mu^2)^{\frac{n-2}{2}} + 4-n \right\}]$$

$$= \frac{\partial X}{\partial \mu}$$

Eq. (280) is directly integrable, giving

$$X = \frac{1}{2} \int_0^{\mu^2} dx \ T \ [(\mu_c^2-\mu^2)^{n/2} + \frac{4-n}{2} \log \frac{1-\mu^2}{1-\mu_c^2} + C_1] \tag{281}$$

Near $\mu \sim 0$, X must approach zero; an approximate solution is

$$X \sim \frac{1}{2} \ \mu^2 T \ [\mu_c^n - \frac{4-n}{2} \ \ln (1-\mu_c^2) + C_1] \tag{282}$$

This gives

$$D_{\mu\mu}\tau \sim (1-\mu^2) \ [\mu_c^2 - \frac{4-n}{2} \ln (1-\mu^2) + C_1]/[2n\mu_c^{n-2} + 8-2n] \tag{283}$$

For n=2

$$D_{\mu\mu}\tau \sim \frac{1}{4} \ (1-\mu^2) \ [\mu_c^2 - \ln (1-\mu^2) + C_1] \tag{284}$$

The total loss rate for the above distribution must be consistent with the rate of filling of the loss cone. The total number of particles contained in a tube of unit cross sectional area at the equator is

$$N = 2\pi \int_0^{\mu_c} f \ 4R_E LT \ \mu d\mu \tag{285}$$

It follows from (279) and (285) that the total loss rate is

176

$$\frac{dN}{dt} = 2\pi \int_{0}^{\mu_c} \frac{df}{dt} \, 4R_E LT\mu d\mu \qquad (286)$$

$$= 2\pi D_{\mu\mu} \; 4R_E LT \; \mu_c \; \left(\frac{\partial f}{\partial \mu}\right)_{\mu=\mu_c}$$

Substituting for $D_{\mu\mu}$ and T gives

$$\frac{dN}{dt} \approx - \left\{ 1 \times 10^{10} \; [1-.4635(1-\mu_c^2)^{3/8}] \; \frac{D_{\mu\mu}(\mu)}{D_{\mu\mu}(1)} \; \frac{f}{\tau} \; L\mu_c^2 \right\} \qquad (287)$$

$$x \propto n < 2$$

$$x \; \frac{2-\mu_c^2}{2} \quad n = 2$$

$$x \; \frac{4-n}{n\mu_c^{n-2} + 4-n} \quad 2 < n < 4$$

It is readily seen that distributions of the form

$$f \propto (\mu_c^2 - \mu^2)^{n/2} \quad n < 2 \qquad (288)$$

are not physically realistic approximations to a normal decay mode. They should be replaced by the more complicated formula, (277), to ensure that the loss cone filling is computed correctly. Even in the current decay model, this is an important consideration because the precipitating fluxes at low altitudes are normalized to $\frac{dN}{dt}$ rather than f.

Replacing the present long time distribution by the above distribution (277) would have slight effect on computational efficiency, and would ensure that the distribution does approach a true normal mode. This distribution could be used with the present early time decay model, or, alternately, the complete set of eigenfunctions could be built up from the lowest mode. The remaining eigenfunctions could be easily computed with the aid of standard eigenfunction generating codes.

Another, quite different, approach to the electron decay problem is to employ a purely numerical method that works for any arbitrary set of diffusion coefficients. An appropriate method has been developed and described above in Section VI. The computer code there has an advantage in that radial diffusion is explicitly included; though radial diffusion can be omitted with substantial improvements in computing efficiency. The code at present is not very fast, but it should be competitive with eigenfunction methods. Of

177

course, the explicit integration must be turned off when it reaches the lowest mode decay if the potential computing efficiency is to be realized. All the decay models have one feature in common: that they revert eventually to a fixed pitch-angle distribution which can be either represented by an algebraic function, or by a table of interpolation coefficients.

One of the essential features of any decay scheme is that it be compatable with the model used to derive fluxes in the drift loss cone. It has not been feasible to model the loss cones as well as the trapped part of the distribution. Perhaps we should consider a more elaborate calculation in which the loss cones are treated on an equal footing to the rest of the distribution. We have constructed numerical computations of the drift loss cone filling and used them to develop the current loss model. That calculation did not treat the early-time decay, but there is no reason why all phases of the decay could not be treated. The only difficulty is in modelling the atmospheric backscatter (which is ignored in the current model). We now know how to treat the atmospheric backscatter, and approximate it quite well in a bounce averaged diffusion calculation (Refs. 11, 12). A normal-mode approach may be feasible for the drift loss cone problem; we do not, however, know of any way the atmospheric backscatter could be accurately represented in the construction of eigenfunctions.

SECTION VIII
RECOMMENDATIONS FOR FUTURE WORK

The new injection model—including the initial distribution of the debris
and hot air near the magnetic bubble, the initial jetting of the debris,
the outward convection of the debris tube, and the redistribution of the
electrons due to the motion of the debris tube—is a considerable improve-
ment over the previous models. The pertinent phenomena are treated real-
istically for all L values. It is therefore expected to provide a good
basis for the computation of the trapped-electron distribution due to any
size burst at any point in the magnetosphere, not just for the limiting
cases of the very small and very large bursts at points where the tests
have been conducted, which is strictly true for the old injection models.
Certain parameters of the old models had been adjusted to generate fluxes
that were in agreement with the nuclear test results. There are no such
adjustable parameters in the new model.

Nevertheless, the model still has shortcomings that should be improved
in future efforts. In the first place, the assumption in the debris motion
model that the magnetic field lines are equipotentials is not valid for
high yields. The rate of change of the neutralizing current along the
magnetic field is so large that the electric field along the magnetic field,
due to the effective inductance of the circuit, is not negligible. In
fact, for Starfish the associated potential drop along the magnetic field
at early times was about one-third of the potential across the tube. This
effect could be improved by using a transmission-line model, with approp-
riate distributed capacitance, inductance, and resistance, rather than
the equivalent LCR resonant circuit with lumped parameters, to compute
the distribution of the debris in the magnetosphere. In addition to ac-
counting for the potential difference along the magnetic field, this approach
would also correct the difficulty in the present model that the entire
capacitance of the tube is used in the circuit even while the hot-plasma

front is moving along the tube. This effect is not realistic since the thermal plasma ahead of the front does not know about the advancing plasma; i.e., the front moves faster than an Alfvén wave.

As discussed in Section II.2b, subsection (3), it appears that anomalous resistivity may also appear along magnetic field lines. Even though its magnitude cannot be determined reliably at the present time, representative values based on observations in the auroral zones could be included in the transmission-line model to assess its importance on the debris distribution.

Futher work on the redistribution model is also warranted, especially since the Telstar satellite data obtained after the Starfish test have not yet been satisfactorily explained (see Section III.2). In particular, the redistribution of the electrons that occurs during their eastward drift motion, while they are bunched in longitude, should be computed. This process is discussed in Section II.4b.

A problem of secondary concern is the likelihood of anomalous trapping, as originally suggested by Davidson (Ref. 48). Though the expected magnitude of the effect is not very large (efficiencies less than 25% have been suggested for low yield bursts, less for high yield) there may be circumstances, e.g. nuclear testing at 80 to 200 kilometers altitude, where there is a possibility of serious damage to satellites. The problem merits an exploratory investigation to determine its likely magnitude and impact on SPECTER.

A troublesome shortcoming of the trapped electron model is the difficulty of interpolating meaningful flux values to obtain the energy spectrum at early times. As discussed in Section II.5, the early-time drift diluted fluxes are highly irregular in time, longitude, and energy. The present interpolation scheme was fully adequate as long as the total flux (or 1 MeV equivalent flux) alone was used to evaluate satellite irradiation. The growing need for spectral information points out the desirability of replacing the interpolation of drift diluted electron fluxes. The most promising approach is the use of a semi-analytical model, suggested in

Section II.5, which treats the drift in a fashion consistent with first-principal physics. This has an added advantage in that it would retain much of the present coding.

Finally, the computed fluxes for Argus-3, Starfish, and U.S.S.R. tests should be further tested against reliable experimental data.

The electron loss model shows some obvious needs for improvement, mainly where the observational data have been inadequate to define the loss rates. A continuing search for better data is called for, but even more important is a continuing effort to incorporate the data in the loss model. The loss model appears adequate for most of the trapped electrons, though much remains to done in establishing the physical bases for energy and L-dependent loss rates. A moderate scale program should be directed toward evaluating the improvements that could be expected from an improved loss model; it would be very worthwhile to compare the advantages of normal-mode models vs. diffusion models. Only after such a study would it be wise to consider replacing the present trapped electron model with something more complicated.

The low altitude part of the loss model, especially the drift loss cone part, is not so satisfactory. At least one effect, atmospheric backscatter, has been totaly neglected; though it is possible to achieve a backscatter albedo as high as 10 to 50% at 1 to 3 MeV for a fission decay spectrum. The backscatter contribution must be evaluated in a manner consistent with the results of Davidson and Walt (Ref. 41, 42). The relevant observational data have not yet been analyzed to determine the relative contributions of diffusion, backscatter, and drift; but, nonetheless, this would be an appropriate time to consider improving the low altitude loss model in SPECTER. A straightforward approach would be to make slight improvements in the trapped electron loss model, as discussed in Section VII.3, and do a new set of calculations for fluxes in the drift loss cone. The trapped and loss cone distributions could be joined in a way similar to that now used; but with a more detailed pitch angle distribution.

The SPECTER development program is presently supported by several related programs at Lockheed Palo Alto Research Laboratory. We have developed a computer code to calculate pitch-angle diffusion into the drift loss cones, and hope to apply it to the analysis of low altitude energetic-election data. The development of the combined radial and pitch-angle diffusion code, discussed in Section VI is continuing independent of the immediate SPECTER needs. We are engaged in a cooperative program with Dr. H. West of Lawrence Livermore Laboratories to use the code to analyze his outer belt electron data (Ref. 44) to derive loss rates.

REFERENCES

1.

2

3. Cladis, J. B., G. T. Davidson, W. E. Francis, R. K. Landshoff,
    and M. Walt, *Improvement of SPECTER II Code*, AFWL-TR-75-286, Air
    Force Weapons Laboratory, Kirtland Air Force Base, Albuquerque,
    N. M., 87115, Sept. 1976

4. Schulz, M., "Particle Lifetimes in Strong Diffusion", *Astrophys.*
    Sp. Sci.. 31, 37, 1974

5. Kindel, J. M., and C. F. Kennel, "Topside Current Instabilities",
    J. Geophys. Res., 76, 3055, 1971

6. Mozer, F. S., C. W. Carlson, M. K. Hudson, R. B. Torbert, B. Parady,
    J. Yatteau, and M. C. Kelley, "Observations of Paired Electrostatic
    Shocks in the Polar Magnetosphere", *Phys. Rev. Lett.*, 38. 292, 1977

7. Cladis, J. B. and R. D. Sharp, "Electrostatic Potential Differences
    along Magnetic Field Inferred from Satellite Measurements of Electron
    and Ion Distributions", *Trans. Am. Geophys. Union*, 58. 473, 1977

8. Mizera, P. F., and J. F. Fennell, "Charged Particle Distributions
    in the Presence of Large DC Electric Fields", *Trans. Am. Geophys.*
    Union, 58. 472, 1977

183

9.   Hudson, M. K., R. L. Lysak, and F. S. Mozer, "Magnetic Field
     Aligned Potential Drops Due to Electrostatic Ion Cyclotron Turb-
     ulance", Geophys. Res. Lett., 5, 143, 1978

10. Chiu, Y. T., "An Improved Phenomenological Model of Ionospheric
     Density", J. Atmos. Terr. Phys., 37, 1563, 1975

11. Johnson, C. Y., "Ionic Composition and Density from 90 to 1200
     Kilometers at Solar Minimum", J. Geophys. Res., 71, 330, 1966

12   Carpenter, D. L., "Whistler Studies of the Plasmapause in the
     Magnetosphere", J. Geophys. Res., 71, 711, 1966

13. Titheridge, J. E., "Plasmapause Effects in the Top Side Ionosphere",
     J. Geophys. Res., 81, 3227, 1976

14. Walt, M., "History of Artificial Radiation Belts", The Trapped
     Radiation Handbook, DNA 2524H, Headquarters, Defense Nuclear
     Agency, Washington, D. C. 20305, December 1971

15. H. I. West, Jr., L. G. Mann, and S. D. Bloom. University of California
     Report UCRL-7659, TID-4500, 1964.

16. H. I. West, Jr., "The Trapped Electron Spectra from the Starfish
     Detonation and from the Outer Belt in the Fall of 1962", in Radiation
     Trapped in the Earths Magnetic Field, ed. by B. M. McCormac, D. Reidel
     Publishing Co., Dordrecht, 663, 1966.

17. W. L. Brown and J. D. Gabbe, "The Electron Distribution in the Earth's
     Radiation Belts during July 1962 as Measured by Telstar, J. Geophys.
     Res. 68, 607, 1963.

18. W. L. Brown, W. N. Hess, and J. A. Van Allen, "Collected Papers on the Artificial Radiation Belt from the July 9, 1962, Nuclear Detonation", J. Geophys. Res., <u>68</u>, 605, 1963.

19. K. W. Chan, D. M. Sawyer, and J. I. Vette, "Trapped Radiation Population", in the <u>Trapped Radiation Handbook</u>, DNA 2524H, revised 1977.

20. S. A. Colgate, "Energetic Electrons from Shock Heating in the Exosphere", in <u>Radiation Trapped in the Earth's Magnetic Field</u>, ed. by B. M. McCormac, D. Reidel Publishing Co., Dordrecht, 693, 1966.

21. J. Zinn, H. Hoerlin, and A. G. Petschek, "The Motion of Bomb Debris Following the Starfish Test", in <u>Radiation Trapped in the Earth's Magnetic Field,</u> ed. by B. M. McCormac, D. Reidel Publ. Co., Dordrecht, 671, 1966.

22. Elliot, H., "Some Cosmic Ray and Radiation Belt Observations Based on Data From the Anton 302 G-M Counter in Ariel 1", <u>Radiation Trapped in the Earth's Magnetic Field</u>, B. M. McCormac, ed., D. Reidel Publishing Co., Dordrecht-Holland, 1966

23. O'Brien, B. J., J. A. Van Allen, C. D. Laughlin, and L. A. Frank, "Absolute Electron Intensities in the Heart of the Earth's Outer Radiation Zone", <u>J. Geophys. Res.</u>, <u>67</u>, 397, 1962

24. Kennel, C. F. and H. E. Petshek, "Limit on Stably Trapped Particle Fluxes", <u>J. Geophys. Res.</u>, <u>71</u>, 1, 1966

25. Lyons, L. R., R. M. Thorne, and C. F. Kennel, "Pitch Angle Diffusion of Radiation Belt Electrons within the Plasmasphere", <u>J. Geophys. Res.</u>, <u>77</u>, 3455, 1972

26. Bullough, K., A. R. L. Tatnall, and M. Denby,"Man-Made ELF/VLF Emissions and the Radiation Belts", Nature, 260, 401, 1976

27. Helliwell, R. A., J. P. Katsufrakis, T. Bell, and R. Raghuram, "VLF Line Radiation in the Earth's Magnetosphere and Its Association with Power System Radiation", J. Geophys. Res., 80, 4249, 1975

28. Lyons, L. R. and D. J. Williams, "A Comment on the Effects of Man-Made VLF Waves on the Radiation Belts", Geophys. Res. Lett., 5, 116, 1978

29. Vampola,A. L. and G. A. Kuck, "Induced Precipitation of Inner Zone Electrons, 1. Observations", J. Geophys. Res.,83, 2543, 1978

30. Imhof, W. L., J. B. Reagan, and E. Gaines, "The Energy Selective Precipitation of Inner Zone Electrons", J. Geophys. Res., 83, 4245, 1978

31. Inan, U. S., T. F. Bell, and R. A. Helliwell, "Nonlinear Pitch Angle Scattering of Energetic Electrons by Coherent VLF Waves in the Magnetosphere", J. Geophys. Res., 83, 3235, 1978

32. Davidson, G. T., "Sources and Losses of Trapped Particles". The Trapped Radiation Handbook, DNA 2524H, Headquarters, Defense Nuclear Agency, Washington, D. C. 20305, 1977

33. Schulz, "Particle Saturation in the Outer Zone: A Nonlinear Model", Astrophys. Sp. Sci., 29, 233, 1974

34. Gabbard, C. E., and J. M. Green, "A First Estimate of the Electron Fluence Intercepted by Low-Altitude Satellites Orbiting in an Intense Artificially Saturated Radiation Belt", RDA-TR-605009-002, R. and D. Associates, Marina Del Rey, Ca., 1977

35.   Cladis, J. B., G. T. Davidson, W. E. Francis, W. I. Futterman, L. L. Newkirk, and M. Walt, "Trapped Radiation Studies Involving Plasma Instabilities and Radial Diffusion" DNA 2824F, Headquarters, Defense Nuclear Agency, Washington, D. C. 20305 1977

36.   Fälthammar, C. G., "On the Transport of Trapped Particles in the Outer Magnetosphere", J. Geophys. Res., 71, 1487, 1966

37.   Schulz, M., and L. J. Lanzerotti, Particle Diffusion in the Radiation Belts, Springer, New York, 1974

38.   Haerendel, G., "Diffusion Theory of Trapped Particles and the Observed Proton Distribution", Earth's Particles and Fields, B. M. McCormac, ed., Reinhold, New York, 1968

39.   Walt, M., "Radial Diffusion of Trapped Particles", Particles and Fields in the Magnetosphere, B. M. McCormac, ed., D. Reidel Publishing Co., Dordrecht-Holland, 1970

40.   Davidson, G. T., "The Motion of Charged Particles in the Earth's Magnetic Field", The Trapped Radiation Handbook, DNA 2524H, Headquarters, Defense Nuclear Agency, Washington, D. C. 20305, 1977

41.   Davidson, G. T., "Pitch Angle Diffusion of Trapped Particles in the Presence of a Loss Cone: Calculating the Distribution of Particles Precipitating from the Earth's Radiation Belts", J. Comput. Phys., in press, 1978

42.   Davidson, G. T., and M. Walt, "Loss Cone Distributions of Radiation Belt Electrons", J. Geophys. Res., 82, 48, 1977

43.   Ahlberg, J. H., E. N. Nilson, and J. L. Walsh, The Theory of Splines and their Application, Academic Press, New York, 1967

44. West, H. I., "The Signatures of the Various Regions of the Outer Magnetosphere in the Pitch Angle Distributions of Energetic Particles", UCRL-81152, U. of California, Lawrence Livermore Lab., Livermore, Ca. 94550, 1978

45. Schulz, M., "Pitch Angle Diffusion in Canonical Coordinates", Trans. Am. Geophys. Union, 58, 1218, 1977

46. Kennel, C. F., "Consequences of a Magnetospheric Plasma", Rev. Geophys. Sp. Sci., 7, 379, 1969

47. Theodoridis, G. C., and F. R. Paolini, "Pitch Angle Diffusion of Relativistic OUter-Belt Electrons", Ann. Geophys., 23, 375, 1967

48. Davidson, G. T., "Enhancement of Artificial Electron Belts through Interactions of Electrons with Ion Cyclotron Waves", J. Geophys.Res., 78, 7569, 1973

49. Nicolet, M., "The Collision Frequency of Electrons in the Ionosphere", J. Atmos. Terrest. Phys., 3, 200, 1953

50. Chapman, S., "The Electrical Conductivity of the Ionosphere: A Review", Nuovo Cimento, 4, suppl., 1385, 1956

DISTRIBUTION LIST

DEPARTMENT OF DEFENSE

Defense Documentation Center
Cameron Sta, Alexandria VA 22314
12 cy ATTN: TCA

Director
Defense Nuclear Agency
Washington DC 20305
      ATTN: DDST
      ATTN: RAEV
      ATTN: STVL
      ATTN: RAAE
4 cy ATTN: TITL Tech Library

Commander
Field Command
Defense Nuclear Agency
KAFB NM 87117
      ATTN: FCPR

Director
Joint Strategic Target Planning Staff, JCS
Offutt AFB NE 68113
      ATTN: Document Control

DEPARTMENT OF THE ARMY

Director
US Army Ballistic Research Laboratories
ATTN: DRDAR-TSB-S
Aberdeen Proving Ground MD 21005

Commander
US Army SATCOM Agency
Ft Monmouth NJ 07703
ATTN: Document Control

DEPARTMENT OF THE NAVY

Director
Naval Research Laboratory
Washington DC 20375
ATTN: Code 6780 S. Ossakow

Commanding Officer
Navy Astronautics Group
Box 30, Point Magu CA 93042
ATTN: W. J. Gleason

189

DISTRIBUTION LIST

DEPARTMENT OF DEFENSE

Defense Documentation Center
Cameron Sta, Alexandria VA 22314
12 cy ATTN: TCA

Director
Defense Nuclear Agency
Washington DC 20305
        ATTN: DDST
        ATTN: RAEV
        ATTN: STVL
        ATTN: RAAE
4 cy ATTN: TITL Tech Library

Commander
Field Command
Defense Nuclear Agency
KAFB NM 87117
        ATTN: FCPR

Director
Joint Strategic Target Planning Staff, JCS
Offutt AFB NE 68113
        ATTN: Document Control

DEPARTMENT OF THE ARMY

Director
US Army Ballistic Research Laboratories
ATTN: DRDAR-TSB-S
Aberdeen Proving Ground MD 21005

Commander
US Army SATCOM Agency
Ft Monmouth NJ 07703
ATTN: Document Control

DEPARTMENT OF THE NAVY

Director
Naval Research Laboratory
Washington DC 20375
ATTN: Code 6780 S. Ossakow

Commanding Officer
Navy Astronautics Group
Box 30, Point Magu CA 93042
ATTN: W. J. Gleason

DEPARTMENT OF THE AIR FORCE

Commander
Air Force Weapons Laboratory, AFSC
KAFB NM 87117
    ATTN: HO (Dr Minge)
2 cy ATTN: SUL
6 cy ATTN: DYC

Headquarters
AF Systems Command
AAFB DC 20334
    ATTN: DLWM

AUL (LDE), Maxwell AFB, AL 36112

DEPARTMENT OF DEFENSE CONTRACTORS

Aerospace Corporation
Box 92957
LA CA 90009
    ATTN: George Paulikas

Lockheed Missiles and Space Company
3251 Hanover St
Palo Alto CA 94304
    ATTN: John B Cladis
    ATTN: G T Davidson
    ATTN: L L Newkirk
    ATTN: W E Francis
    ATTN: Martin Walt
    ATTN: Tech Information Center

Mission Research Corporation
Drawer 719
Santa Barbara CA 93102
    ATTN: D Sowle

Official Record Copy
    (AFWL/DYC. Capt Backstrom)